12-2024

# Anomalous Proximitized Transport Properties in Heterostructures Built on Geometrically Frustrated Lattice

Chengkun Xing
cxing2@vols.utk.edu

To the Graduate Council:

I am submitting herewith a dissertation written by Chengkun Xing entitled "Anomalous Proximitized Transport Properties in Heterostructures Built on Geometrically Frustrated Lattice." I have examined the final electronic copy of this dissertation for form and content and recommend that it be accepted in partial fulfillment of the requirements for the degree of Doctor of Philosophy, with a major in Physics.

Haidong Zhou, Major Professor

We have read this dissertation and recommend its acceptance:

Jian Liu, Cristian Batista, Dustin Gilbert

Accepted for the Council:

Dixie L. Thompson

Vice Provost and Dean of the Graduate School

(Original signatures are on file with official student records.)

To the Graduate Council:
I am submitting herewith a dissertation written by Chengkun Xing entitled "Anomalous Proximitized Transport Properties in Heterostructures Built on Geometrically Frustrated Lattice." I have examined the final paper copy of this dissertation for form and content and recommend that it be accepted in partial fulfillment of the requirements for the degree of Doctor of Philosophy, with a major in Physics.

Haidong, Zhou, Major Professor

We have read this dissertation
and recommend its acceptance:

Jian, Liu

Cristian Batista

Dustin, Gilbert

Accepted for the Council:

Dixie L. Thompson

Vice Provost and Dean of the Graduate School

# Anomalous Proximitized Transport Properties in Heterostructures Built on Geometrically Frustrated Lattice

A Dissertation Presented for the

Doctor of Philosophy

Degree

The University of Tennessee, Knoxville

Chengkun Xing

December 2024

*To my lovely girlfriend, Yanan, and my parents, Shengyu and Guilin*

# Acknowledgements

First and foremost, I would like to express my deepest gratitude to my supervisors, Prof. Haidong Zhou and Prof. Jian Liu, for their guidance, leadership, and patience throughout the course of this work. They spent a lot of time training me when I was a fresh person to the lab. I could not have completed this Ph.D. without their support and encouragement.

I am also deeply grateful to my committee members, Dr. Cristian Batista, Dr. Dustin Gilbert for their constructive instructions.

A special thanks goes to Dr. Eun Sang Choi for his patience and technical support at the National High Magnetic Field Laboratory (NHMFL). His expertise has been invaluable in overcoming many technical challenges.

This dissertation would not have been possible without the collaborations that contributed significantly to its success. I would like to extend my heartfelt thanks to Prof. Lu Li, Dr. Yan Xin, Dr. Lukas Horak, Prof. Zhigang Jiang, Dr. Shu Zhang and all the other collaborators for their contributions to these projects.

I must also acknowledge all my colleagues: Qing Huang, Han Zhang, Kyle Noordhoek, Lin Hao, Dapeng Cui, Shashi Pandey, Dongliang Gong, Alexander Brassington, Weiliang Yao, Qiang Chen, Hao Zhang, Junyi Yang for their help, encouragement in my Ph.D. life. Additionally, I am grateful to the faculty and staff of the Physics Department for their support and guidance.

I sincerely thank the University of Tennessee, the Center for Material Processing, and the Department of Physics for their financial support, which has been vital to my academic progress.

Finally, I would like to thank my girlfriend, Yanan He, for her support, patience, and encouragement throughout my Ph.D. journey. Her belief in me has been a constant source of strength.

# Preface

The following presented in this dissertation has been published or in preparation of publishing:

## Chapter 3

Zhang, H., Xing, C., Noordhoek, K. et al. Anomalous magnetoresistance by breaking ice rule in $Bi_2Ir_2O_7/Dy_2Ti_2O_7$ heterostructure. Nat Commun 14, 1404 (2023).

## Chapter 4

Xing, C., Zhang, S., Yao, W. et al. Phys. Rev. Materials 8, 114407 (2024)

## Chapter 5

Xing, C., Zhang, H., Noordhoek, K., Zheng, G., Chen, K., Horák, L., Xin, Y., Choi, E., Li, L., Zhou, H., Liu, J. in preparation

# Abstract

While geometrically frustrated quantum magnets (GFQMs) host rich exotic spin states with potentials for revolutionary quantum technologies, most of them are necessarily good insulators which are difficult to be integrated with modern electrical circuit. The grand challenge is to electrically detect the emergent fluctuations and excitations by introducing charge carriers that interact with the localized spins without destroying their collective spin states. This thesis consists of three projects that design a new series of heterostructures which combine the insulating GFQMs and spin-orbit entangled correlated metal to study the exotic magnetic excitations in GFQMs. Chapter 1 describes the background to the magnetic properties of geometrically frustrated pyrochlore magnets, and gives the motivation of the original research presented later. Chapter 2 describes experimental techniques including heterostructure synthesis and heterostructure characteristics. In chapter 3, $Bi_2Ir_2O_7/Dy_2Ti_2O_7$ heterostructure is designed to capture the characteristic angular and temperature dependence of ice-rule-breaking transition. In chapter 4, we design a $Bi_2Ir_2O_7/Yb_2Ti_2O_7$ heterostructure to show that the proximitized transport in $Bi_2Ir_2O_7$ can be effectively tuned by magnetic field through suppressing the quantum spin fluctuations as well as inducing transitions via magnetic anisotropy in $Yb_2Ti_2O_7$. In chapter 5, by synthesizing 18nm-thick $Dy_2Ti_2O_7$ thin film on YSZ substrate and capped by a thin conductive $Bi_2Ir_2O_7$ layer, it confirmed that the ice-rule-breaking phase transition survives in the thin film but with a significantly reduced effective nearest-neighbor interaction compared to the bulk crystal.

# Table of Contents

# Chapter 1

# Introduction

Geometrically frustrated quantum magnets (GFQMs) are known for a variety of novel ground state and emergent excitations [1, 2, 3]. Frustration is common in systems of interacting degrees of freedom. Usually a system is classified as frustrated when the energy of the whole system cannot be minimized by minimizing pairwise interaction energy. One type of frustration is geometric, and the simplest example is that frustration arises on triangular or tetrahedral lattices with antiferromagnetically spin interaction, as shown in Fig. 1.1(a). As one of the typical GFQMs, pyrochlore $A_2B_2O_7$ have attracted much attention, because the structure is formed by two corner-sharing tetrahedral lattices (Fig. 1.1(b)). Pyrochlore is highly frustrated if A or B are magnetic, so it provides a new platform for novel quantum effects to emerge at low temperatures. In the following subsections, we will focus on the introduction to two representative GFQMs: $Dy_2Ti_2O_7$ and $Yb_2Ti_2O_7$.

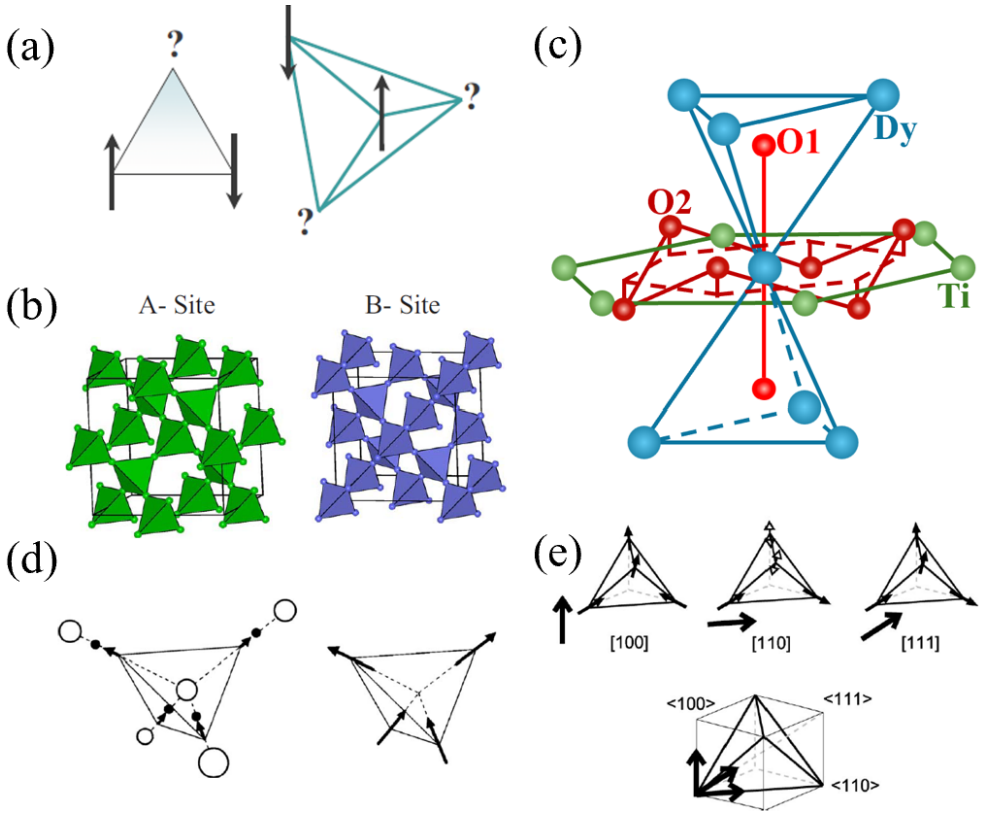


**Figure 1.1:** (a): Frustration arises on triangular or tetrahedral lattices with antiferromagnetically spin interaction [3]. (b): Lattices of corner-sharing tetrahedra [3]. (c): Oxygen environment surrounding rare earth ion in spin ice [4]. (d): Analogy of "2-in-2-out" configurations between ice structure and spin ice [3]. (e): Spin configurations at saturated states when the external field is applied along different principal axes [5].

## 1.1 Introduction to spin ice in geometrically frustrated pyrochlore

### 1.1.1 Single-ion anisotropy

In DTO spin ice, it contains the ions $O^{2-}$, $Ti^{4+}$ and $Dy^{3+}$. Like the $O^{2-}$ ion, $Ti^{4+}$ ion is also non-magnetic; therefore, the magnetic properties at low temperature originate from the $Dy^{3+}$ ion with unfilled 4f shells. However, the dynamics of $Dy^{3+}$ spins is not self-dependent but largely rooted in the crystal field on rare earth element sites. The surrounding nearest negative oxygen ions determine the crystal field, which deeply affects the single-ion quantum state [6, 4].

Fig. 1.1(c) shows the surrounding oxygen environment of rare earth ions. Eight oxygen ions can be divided into two subclasses: the O1 and O2 sites. The O1 ions site on the center of the tetrahedra formed by $Dy^{3+}$ ions, and the line between $Dy^{3+}$ ion and its nearest O1 ion is in the direction of the $\langle 111 \rangle$ crystal axes of the pyrochlore structure. According to relevant theoretical calculations on crystal-field Hamiltonian [4, 7], these closer O1 ions are responsible for the classical Ising-like anisotropy behavior of $Dy^{3+}$ ion spin. The ground state of the crystal-field Hamiltonian is fully polarized state: $|\phi^{\pm}\rangle \approx |M_J = \pm\frac{15}{2}\rangle$, representing strong anisotropy along $\langle 111 \rangle$ crystal axes. The crystal field spectra of $Dy^{3+}$ ion shows that the energy gap between the ground state and first excited state is larger than 250 K [4]. Therefore, when studying the magnetic behavior at low temperatures (typically below 1 K), $Dy^{3+}$ spin behaves with classical strong Ising-like anisotropy, which means that the direction of spin can only point "in" or "out" towards the center of the tetrahedra.

### 1.1.2 Dipolar spin ice Hamiltonian

Besides the crystal-field effect, magnetic behavior at low temperature in the spin ice system depends on the competition between different kind of spin-spin interaction. Due to the sizeable spin moment in the DTO system, long range dipole-dipole

interaction plays an important role. The dipolar spin ice Hamiltonian is as following (the first term is nearest-neighbor interaction, and the second term is dipolar interaction) [3]:

$$H = -J \sum_{<i,j>} \boldsymbol{S}_i^{z_i} \cdot \boldsymbol{S}_j^{z_j} + D r_{nn}^3 \sum_{<i,j>} \left( \frac{\boldsymbol{S}_i^{z_i} \cdot \boldsymbol{S}_j^{z_j}}{|\boldsymbol{r}_{ij}|^3} - \frac{3(\boldsymbol{S}_i^{z_i} \cdot \boldsymbol{r}_{ij})(\boldsymbol{S}_j^{z_j} \cdot \boldsymbol{r}_{ij})}{|\boldsymbol{r}_{ij}|^5} \right)$$

where $\boldsymbol{S}_i^{z_i}$ is the Ising moment with amplitude $|\boldsymbol{S}_i^{z_i}| = 1$ pointing to the local Ising axes $\langle 111 \rangle$, and $r_{nn}$ is the nearest-neighbor distance. If only nearest-neighbor interaction is considered, the effective energy scale will be: $J_{eff} = J_{nn} + D_{nn}$, where $J_{nn} = \frac{J}{3}$, $D_{nn} = \frac{5D}{3}$. Relevant studies [6, 7] have simulated these two values using zero-field susceptibility and specific heat data to get $J_{nn} = -1.24$ K, $D_{nn} = 2.35$ K for DTO, therefore the effective energy scale $J_{eff}$ is positive, giving rise to the ferromagnetic nearest-neighbor spin interaction.

### 1.1.3 Zero-point entropy in spin ice system

While frustration is often accompanied by antiferromagnetic interaction, ferromagnetic interaction accounts for the frustration in DTO. Considering only one tetrahedron with strong local axis anisotropy, ferromagnetic nearest-neighbor interaction will favor "2-in-2-out" configuration to minimize the total energy, which means that two spins point "in" toward the center of the tetrahedra and two spins point "out" of the center of the tetrahedra. There are six equivalent-energy configurations in one tetrahedron, which represents the degeneracy. However, each spin is shared by two tetrahedra; the above six"2-in-2-out" configurations are not indepedent on each tetrahedron. Ground state degeneracy in the pyrochlore is: $\Omega = \{2^2(6/16)\}^{N/2} = (3/2)^{N/2}$. Therefore, the number of ground state configurations in the whole material is macroscopically large, and the ground state entropy is extensive. As an analogy, the ground state entropy should be the same as one of ice structure $I_h$ with proton disorder [8], which shows that two protons site "near"

to and two protons site "far " from the oxygen ion, so that every oxygen ion has two adjacent protons, forming a water molecule (Fig. 1.1(d)). This "2-in-2-out" ground state denegeracy is the so-called "ice rule". Zero-point residual entropy is measured by integrating $C(T)/T$ between two temperatures: $\Delta S = \int_{T_1}^{T_2} \frac{C(T)}{T} dT$. The study [9] shows a residual spin entropy $0.67R\ln 2$, which is similar to Pauling's original value for ice $I_h$: $0.71R\ln 2$.

### 1.1.4 Magnetic anisotropy and phase diagram in $Dy_2Ti_2O_7$

Although extensive zero-point entropy exists in the spin-ice system, degeneracy can be lifted when an external field is applied [5], accompanied with time-reversal-symmetry breaking. In Fig. 1.1(e), there are three principal axes in the spin-ice system, which means that the saturated magnetization is parallel to the external field if the external field is applied on these principal axes. Along [100] axes, the saturated magnetic moment is $g_J J\frac{1}{\sqrt{3}} = 5.77\mu_B$/Dy with only one kind of "2-in-2-out" configuration in all tetrahedra. Along [110] axes, the saturated magnetic moment is $g_J J\sqrt{\frac{2}{3}} \times 2/4 = 4.08\mu_B$/Dy, with one spin pointing in, one spin pointing out, and two free spins. Although two spins are free due to perpendicular direction with the external field, each tetrahedron still remains "2-in-2-out" configuration to minimize the exchange coupling energy. Along [111] axes, the saturated magnetic moment is $g_J J(1 + \frac{1}{3} \times 3)/4 = 5\mu_B$/Dy with different configurations in tetrahedra: 3(1)-in-1(3)-out configuration. The above configuration all agrees with the fact that spin anisotropy is along the local $\langle 111 \rangle$ axes.

However, things become interesting when a magnetic field is applied along $\langle 111 \rangle$ at a lower temperature. Crystal structure along $\langle 111 \rangle$ axes is composed by the combination of the triangular and kagome plane, as shown in Fig. 1.2(a). Fig. 1.2(b) shows the magnetization curve at 0.48K, 0.99K, 1.65K separately when the field is applied along $\langle 111 \rangle$ axes [10]. An intermediate plateau can be obviously seen

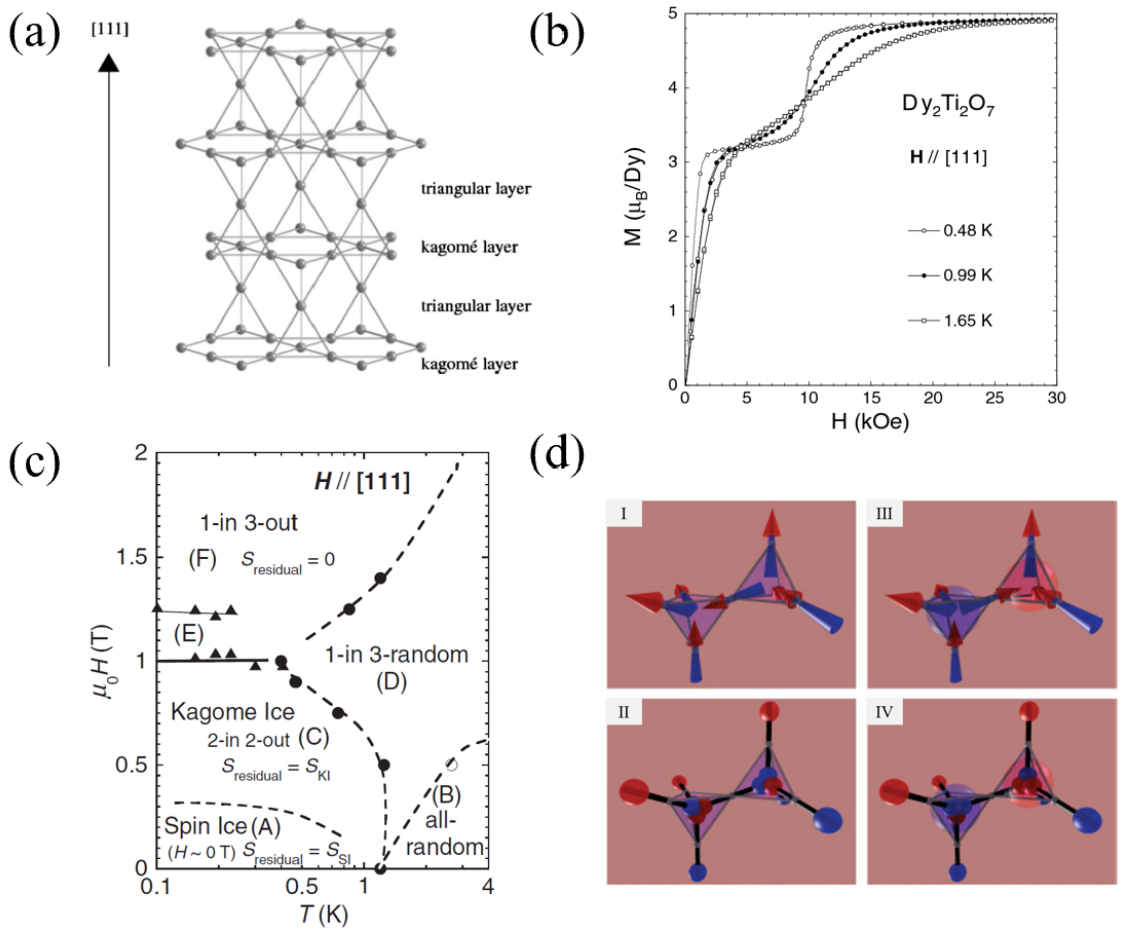


**Figure 1.2:** (a): Alternating kagome and triangular layers along [111] axes in pyrochlore structure [3]. (b): Magnetization curve at 0.48 K, 0.99 K, 1.65 K when the field is along [111] axes [10]. (c): Field-Temperature phase diagram for DTO crystal with ⟨111⟩ oriented field [11]. (d): Analogy between spin ice picture and dumbbell picture [12].

at 0.48K with magnetic moment $g_J J(1+\frac{1}{3}\times 1)/4 = 3.33\mu_B$/Dy, which is in the so-called kagome ice state. In this state, the spins on the triangular plane are parallel to the field direction $\langle 111\rangle$; two of three spins on the kagome plane choose to be polarized by the external magnetic field, but one remaining spin choose to oppose the magnetic field since the Zeeman energy still doesn't exceed the neighboring exchange energy. But in a larger field when Zeeman energy exceeds exchange energy, this field-opposed spin flips. This process is so-called "ice-rule breaking".

Fig. 1.2(c) shows the field-temperature phase diagram for DTO crystal with $\langle 111\rangle$ oriented field [11]. At zero field below around 1 T, the spin ice state is realized. At low temperature with increasing field, the system experiences the transition from spin ice state to kagome ice state, then to 1-in-3-out saturated state. The solid line around 1 T represents the first order phase transition from kagome ice state to 1-in-3-out saturated state. However, crossover region appears around 0.5 K, which is due to that the spins are thermally fluctuating at higher temperature. So the transition from kagome ice state to 1-in-3-out saturated state becomes indistinguishable with increasing temperature, which gives rise to the smooth magnetization increase in Fig. 1.2(b).

### 1.1.5 Magnetic monopoles in spin ice

No elementary particle with a net magnetic charge has been observed in nature. However, this can be realized as emergent particles in the many-body spin-ice system. Dipolar spin ice Hamiltonian can be computed as the magnetic Coulomb law using magnetic charges, which is known as Dumbell Picture [12]:

$$V(r_{\alpha\beta}) = \begin{cases} \frac{\mu_0}{4\pi}\frac{Q_\alpha Q_\beta}{r_{\alpha\beta}} & \alpha \neq \beta \\ \frac{1}{2}\nu_0 Q_\alpha^2 & \alpha = \beta \end{cases}$$

Here $Q_\alpha$ is the total magnetic charge at site $\alpha$, which is the center of each tetrahedron and forms diamond lattice (Fig. 1.2(d)). For example, the tetrahedron with "2-in-2-out" configuration can convert to a site with zero magnetic charge. $r_{\alpha\beta}$ is the distance between two sites. $\nu_0$ is "self-energy" originating from the nearest-neighbor interaction. Since the larger scale value of "self-energy", the total energy is minimized if all $Q_\alpha$is zero, demonstrating that the ground-state in spin-ice system is "2-in-2-out".

The importance of this picture is not only mapping the Hamiltonian and the ground state, but also simulating the phase transition boundary. The theoretical study [12] was done on the diamond lattice with a tuneable lattice gas of monopoles to give the location of the monopole liquid-gas transition. This is near to the experimental solid line, which is exactly ice-rule breaking transition from Kagome ice state to 1-in-3-out saturated state.

## 1.2 Introduction to $Yb_2Ti_2O_7$ in geometrically frustrated quantum magnet pyrochlore

### 1.2.1 Impact of stoichiometry in $Yb_2Ti_2O_7$

In $Yb_2Ti_2O_7$ (YbTO), the magnetic properties at low temperature originate from the $Yb^{3+}$ ion with unfilled 4f shells. The ground state of the crystal-field Hamiltonian is $|\phi^{\pm}\rangle = 0.376\,|\pm\frac{7}{2}\rangle \pm 0.922\,|\pm\frac{1}{2}\rangle - 0.093\,|\mp\frac{5}{2}\rangle$ based on relevant theoretical calculations, which makes it an effective 1/2 spin system [7]. The values of the spectroscopic factors along and perpendicular to the local axis are $g_\parallel = 2.04$ and $g_\perp = 4.09$ [7], respectively, which makes YbTO to have a strong planar crystal electric field anisotropy.

For the last decade, the small effective (S=1/2), XY anisotropy and geometrical frustration makes YbTO a good candidate of quantum spin liquid [13]. However, the ground state of YbTO was debated for a long time [14, 15, 16, 17] due to the experimental inconsistencies of low-temperature transition. The specific heat

transition peak is around 260 mK for YbTO powders [18, 19], but appears at much lower temperature (150-200 mK) for those crystals grown by traditional floating zone method [18, 20, 21]. The color of those crystals with lower transition temperature are yellow, which is due to the off-stoichiometry problem that some $Ti^{4+}$ site is stuffed by $Yb^{3+}$ [22]. Fig. 1.3(a) shows the effect of non-stoichiometry: the transition temperature broadens and decreases as $Yb_{2+x}Ti_{2-x}O_{7-\delta}$ is doped away. Fortunately, the successful synthesis of colorless stoichiometric YbTO crystal was accomplished by traveling solvent floating zone method [22]. The sharp peak is around 268 mK for stoichiometric YbTO crystal, which is similar to that of power data. This high-quality crystal makes it possible to study the real ground state in YbTO system.

### 1.2.2 Magnetic phase diagram and reentrant behavior

The synthesis of ultrapure YbTO crystal enables the examination of magnetic phase diagram from specific heat, ac susceptibility, and neutron scattering: Fig. 1.3(b) shows the field-temperature phase diagram when applying the magnetic field along each of the three main symmetry axes: $\langle 111 \rangle$, $\langle 110 \rangle$ and $\langle 100 \rangle$ [23, 26]. The ground state of YbTO is ferromagnetic below the ordering temperature $T_c = 270$ mK at zero field. For fields along $\langle 111 \rangle$ and $\langle 110 \rangle$, there is a high-field phase boundary from splayed ferromagnetic state to polarized state driven by the competition between the cubic magnetic anisotropy and the Zeeman energy. More interesting thing is the reentrant behavior: applying the magnetic field initially increases the ordering temperature and then suppresses it at higher fields. For field along $\langle 100 \rangle$, the system becomes polarized state with small field [23, 26].

Coarse-grained theoretical model was used to understand the high-field phase transition and the order of the phase boundaries when the field is applied along $\langle 111 \rangle$ or $\langle 110 \rangle$ axes [23]:

$$U = -\mathbf{B} \cdot \mathbf{m} - K_1 \sum_i (\mathbf{m} \cdot \mathbf{e}_i)^4 - K_2 \prod_i (\mathbf{m} \cdot \mathbf{e}_i)^2. \tag{1.1}$$

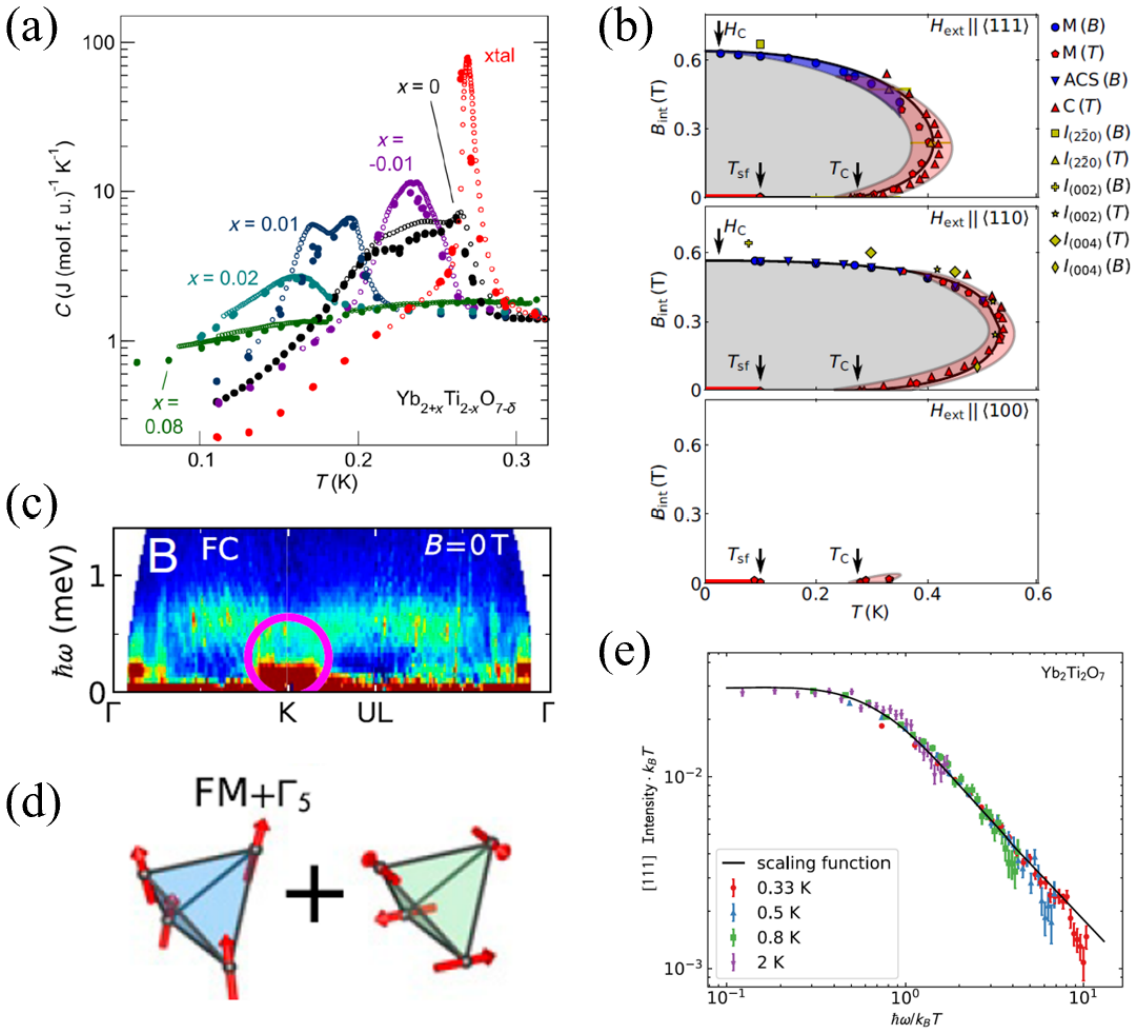


**Figure 1.3:** (a): The specific heat capacity of the sintered rod $Yb_{2+x}Ti_{2-x}O_{7-\delta}$ series [22]. (b): Magnetic phase diagram of $Yb_2Ti_2O_7$ with magnetic field seperately applied along ⟨111⟩, ⟨110⟩ and ⟨100⟩ high symmetry axes [23]. (c): Inelastic magnetic neutron scattering at zero field from $Yb_2Ti_2O_7$ along Γ⟨000⟩ → K⟨2-20⟩ → UL⟨2-11⟩ → Γ⟨000⟩ [24]. (d): Schematic of FM + AFM phase coexistence at zero field [24]. (e): Integrated {111} rod scattering intensity multiplied by temperature as a function of energy divided by temperature [25].

This model describes the competition between the Zeeman energy and the magnetic anisotropy, where $K_1$ represents the anisotropy along $\langle 100 \rangle$ and $K_2$ represents the anisotropy along $\langle 111 \rangle$. This model can catch the magnetic-field induced phase transitions and the corresponding critical field [23], but it cannot explain the reentrant behavior at small field.

### 1.2.3 Multiple phase competition and dynamical scaling

Recently, neutron scattering on YbTO crystal gives evidence for a canted ferromagnetic ground state from elastic neutron scattering and short-range antiferromagnetism from inelastic scattering [24]. This coexistence of AFM + FM phase at zero field gives the broad dispersive spin waves (Fig. 1.3(c)). Fig. 1.3(d) is the schematic of FM + AFM spin configurations at zero field. This multiple phase competition provides the explanation for the reentrant behavior: the strong quantum fluctuations significantly suppress the zero-field ordering temperature.

It is found that, due to proximity to a quantum critical point among the FM and AFM, the dynamical structure factor exhibits a dynamical scaling behavior, which was demonstrated by inelastic neutron scattering in YbTO [25]: Fig. 1.3(e) integrated the $\{111\}$ rod scattering intensity multiplied by temperature, and it follows a $(\hbar\omega/k_BT)^{-n}$ scaling law above $(\hbar\omega/k_BT) = 1$.

## 1.3 Motivation of the pyrochlore heterostructure

Frustration is common in systems of interacting degrees of freedom and novel emergent states of quantum magnets often arise from geometric frustration. Geometrically frustrated quantum magnets (GFQMs) are known for a variety of novel ground state and emergent excitation. However, most GFQMs are good insulators and it's difficult to integrate them in electronic integrated-circuit technology. The challenge here is

to find a new way to convert spin excitations in GFQMs to charge signal. So the primary motivation here is to exploring a new route of "metallizing" the GFQMs.

Here, we design a new heterostructure which combines the insulating GFQMs and spin-orbit entangled correlated metal. We assume that the interaction between local moment in GFQMs and electron carrier in correlated metal can lead to an unusual electronic transport property, which will successfully transfer the spin excitations to charge signal. For the GFQM part, we choose DTO and YbTO as representatives. There are two reasons for this choice. First, DTO and YbTO are well studied over the recent decades. DTO exhibits the first order phase transition from Kagome ice state to 3(1)-in-1(3)-out state at low temperature, accompanied with formation of pairs of monopoles. We would like to electronically detect this phase transition by transport measurement. YbTO was revealed to have ferromagnetic (FM) and antiferromagnetic (AFM) multiphase, and exhibit reentrant phase diagram in a $\langle 111 \rangle$ or $\langle 110 \rangle$ magnetic field. We would like to see the electronic response of quantum spin fluctuations suppression and detect the phase transitions. Second, floating zone method can be used to grow large DTO and YbTO crystal, making it possible to be a substrate. For the correlated metal part of the heterostructure, $Bi_2Ir_2O_7$ (BIO) is selected here. A large family of pyrochlore iridates $R_2Ir_2O_7$ have been studied to have an evolution from insulating behavior to metallic behavior depending on the radius of R, as shown in Fig. 1.4(a). Pyrochlore iridate BIO is a less studied one. Relevant study shows that substitution of the Bi significantly enhances the hybridization between the Bi 6s/6p and Ir 5d electrons, which overpowers the SOC and U, driving a metallic behavior [29]. DC magnetic susceptibility shows no evidence of long-range order with a divergent magnetic susceptibility, and the saturated magnetization at low temperature is less than 2% of the expected one in S=1/2 system, which shows the magnetic instability at low temperature [29]. This behavior is believed to be associated with the proximity to the magnetic quantum critical point of the phase diagram of rare earth pyrochlore iridates [30, 31, 32]. The transport properties of the itinerant electrons in BIO are thus expected to be highly sensitive to spin fluctuations. Recently the magnetoresistance

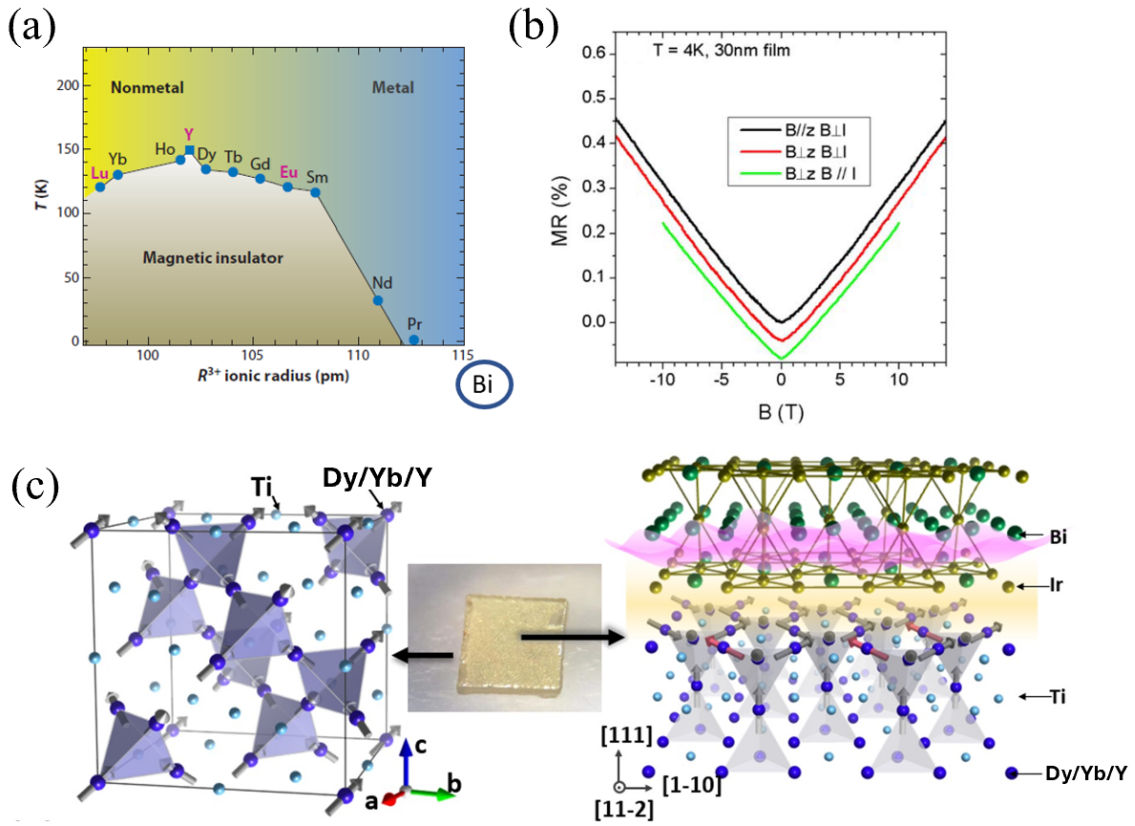


**Figure 1.4:** (a): Phase diagram for the pyrochlore iridates R-227 system [27]. (b): Angle dependence of magnetoresistance at low temperature for BIO film on YSZ substrate [28]. (c): Schematic of heterostructure with BIO film on RTO (R=Dy/Yb/Y) crystal.

of BIO film is studied [28]. At low temperatures, the linear magnetoresistance is positive and isotropic without any sign of saturation up to 35T, as shown in Fig. 1.4(b). We choose BIO as metal part of the heterostructure for two reasons. First, the lattice mismatch between DTO/YbTO and BIO is less than 3%, which is the ideal condition for forming epitaxial growth. Second, The transport properties of the itinerant electrons in BIO are expected to be highly sensitive to spin fluctuations. The study of this heterostructure will provide a revolutionary route to study how exotic magnetic excitations in GFQMs interact with mobile chargers for electrical detection of the emergent entanglement, which will be further used in the future to design quantum information processing devices. Fig. 1.4(c) shows the ion arangements of the heterostructure. Out-of-plane direction is along $\langle 111 \rangle$ axes, which is composed by the combination of the triangular and kagome plane. The axes of two sides are $\langle$1-10$\rangle$ and $\langle$11-2$\rangle$, which makes it easier for the magnetic field to be applied on other principal axes if we rotate the sample along $\langle$1-10$\rangle$ or $\langle$11-2$\rangle$ axes.

# Chapter 2

# Experimental methods

## 2.1 Heterostructure synthesis

### 2.1.1 $Dy_2Ti_2O_7$ crystal growth

Polycrystalline DTO was prepared by thoroughly mixing stoichiometric $Dy_2O_3$ and $TiO_2$ with the molar ratio of 1:2 [33]. Prior to weighing, $Dy_2O_3$ was preheated at 1000 °C for 10 h in order to remove the moisture. After grinding the mixture, sintering the mixture at 1000 °C and 1400 °C for 20 h each in air with intermediate grinding. The powders were then compressed to a feed rod with another additional annealing at 1400 °C for 20 h, which were used to grow the single crystal DTO by using a double elliptical mirror optical floating-zone furnace SC1-MDH from Canon Machinery. To avoid oxygen deficiency, we grew the single crystal in 5 atm flowing $O_2$ atmosphere. In the first cycle we used a high growth rate of 50 mm/h for both feed and seed rods and in the second cycle we used a relatively slow growth rate of 4 mm/h. Many oxide materials can be grown by the Traveling Solvent Floating Zone (TSFZ) method (Fig. 2.1(a)). In this method, the focus of the halogen lamps enables a small molten zone between the seed rod and feed rod. By moving the whole rod slowly downward relative to the fixed halogen lamps, new crystal material will be solidified on the top

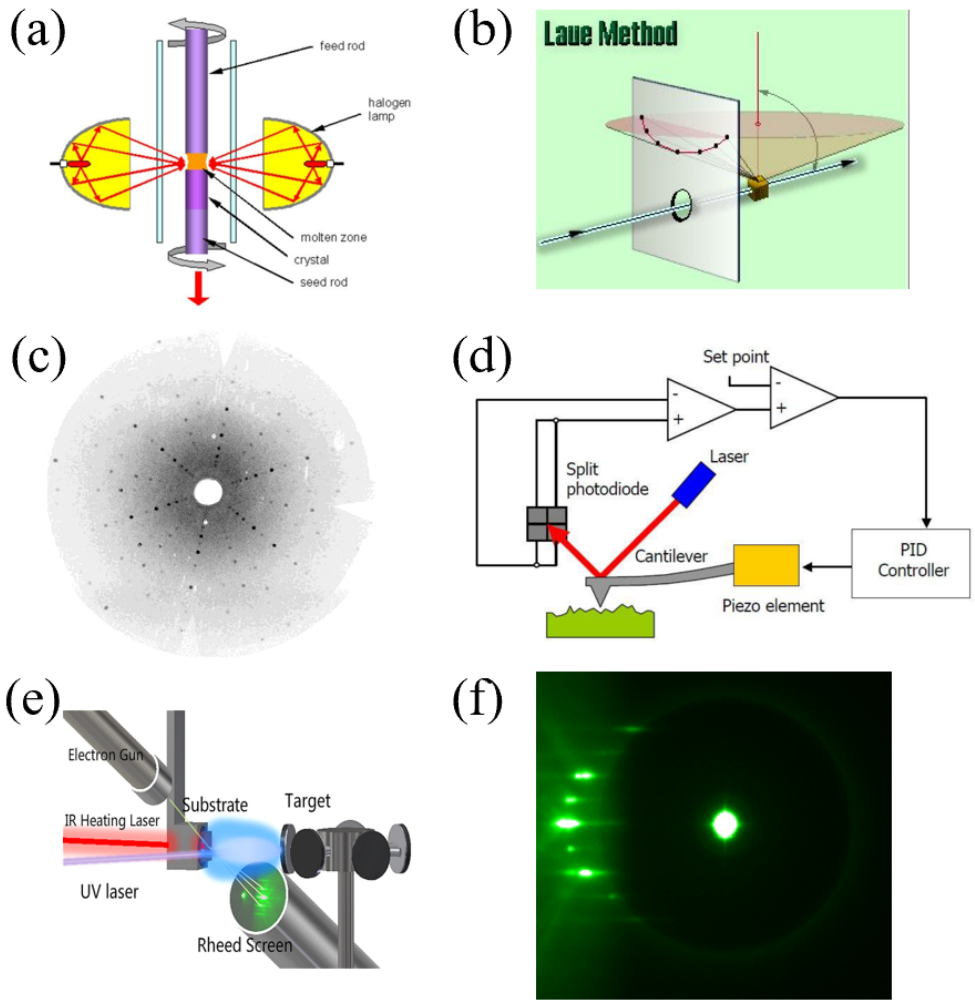


**Figure 2.1:** (a): Schematic of Floating Zone method. (b): Schematic of back-reflection Laue method. (c): Laue pattern when the beam is perpendicular to the pyrochlore (111) plane. (d): Schematic of AFM mechanism. (e): Schematic of Pulsed Laser Deposition method. (f): Reflection High Energy Electron Diffraction (RHEED) pattern of polished YbTO surface before BIO thin film deposition.

of the seed rod. The quality of the grown crystal depends on many factors [34, 35]: crystalization rate, gas atmosphere, gas pressure, and rotation rate.

### 2.1.2 $Yb_2Ti_2O_7$ crystal growth

Stoichiometric YbTO single crystal was prepared with a modified traveling-solvent floating zone method as recently reported [22]. Nonstoichiometric YbTO single crystal and YTO single crystal were prepared with a conventional floating zone method [36], and served as a controlled comparison.

For the crystal growth of stoichiometric YbTO. First polycrystalline YbTO powders were prepared by thoroughly mixing stoichiometric $Yb_2O_3$ and $TiO_2$ with the molar ratio of 1:2. Prior to weighing, $Yb_2O_3$ was preheated at 1000 °C for 10 h in order to remove the moisture. After grinding the mixture, it was sintered at 1000 °C and 1400 °C for 20 h each in air with intermediate grinding. The powders were then compressed to two rods with another additional annealing at 1400 °C for 20 h, which were used to grow the single crystal YbTO by using a double elliptical mirror optical floating zone furnace SC1-MDH from Canon Machinery. The seed rod was the resulting crystal rod with 3.2 mm diameter using the conventional floating zone method with the first fast 50 mm/h growth rate cycle and the second slow 4 mm/h growth rate cycle. The feed rod was the resulting crystal rod with 3.5 mm diameter using the conventional floating zone method with only the first fast 50 mm/h growth rate cycle under 1 atm flowing $O_2$ atmosphere. The top surface of seed rod and bottom surface of feed rod were sanded flat. Two solvent pellets with 3.1 mm diameter and 1.5 mm height were prepared by mixing 30% $TiO_2$ and 70% YbTO powders by mass, then they were melted and joined to the feed and seed rod respectively in the optical furnace before beginning the growth. During the growth, the feed rod was moved downward at a rate of 0.5 mm/h, and the seed rod was moved downward at a rate of 0.7 mm/h. The crystal growth of nonstoichiometric YbTO was used the conventional floating zone method without solvent under 1 atm flowing $O_2$ atmosphere. The feed

rod was moved downward at a rate of 3 mm/h, and the seed rod was moved downward at a rate of 4 mm/h.

### 2.1.3 Substrate preparation

For BIO/RTO heterostructures (R = Dy, Yb, Y), the Laue method is used to determine the orientation of the RTO crystal. Here we used the back-reflection Laue method. As shown in Fig. 2.1(b), the film is between the x-ray source and crystal. According to the Laue pattern and using OrientExpress software, the crystal can be rotated to a particular lattice plane perpendicular to the x-ray beam. In Fig. 2.1(c), this pattern represents that the x-ray beam is perpendicular to the (1,1,1) plane, as shown by its six-fold symmetry.

Then it is crucial to polish the RTO crystal surface to atomic-level smoothness. To realize this, first the crystal surface is polished evenly using sandpaper. Then crystal surface is subsequently polished by using smaller and smaller suspension liquid ($3\mu m \rightarrow 1\mu m \rightarrow 0.05\mu m \rightarrow 0.02\mu m$), each polishing step lasts around 15 min. After polishing the crystal surface using $0.02\mu m$ suspension liquid, thoroughly clean the sample in Ultrasonic cleaner. Etching the sample by putting it in buffered-hydrofluoric acid (BHF) for 10 seconds. Then the sample is rinsed in DI-water for 10 seconds. Finally, annealing the sample in the furnace for 10 hrs under 800 celcius degree temperature.

Finally, atomic force microscopy (AFM) measures the surface topography. As shown in Fig. 2.1(d), a sharp tip at the end of the cantilever moves over the sample surface. A laser is reflected off the backside of the cantilever. The reflection direction changes as the tip moves up and down, which will be detected by the split photodiode to convert the height information.

### 2.1.4 Film growth of $Bi_2Ir_2O_7$

Fig. 2.1(e) shows the technique of Pulsed Laser Deposition (PLD) to do the epitaxial film growth on a substrate. The material is vaporized from the target to form a plasma plume when UV laser beam hits the target. The plasma recondenses on the substrate and forms the epitaxial crystallized film. Whether this process is successful or not depends on many factors [37]: gas atmosphere and pressure inside the chamber, laser energy fluence, depositing temperature. Also, Reflection High-Energy Electron Diffraction (RHEED) is used to detect the roughness of the film in the deposition process. Fig. 2.1(f) shows a representative RHEED pattern of polished YbTO surface, which indicates atomatic-level smoothness.

For BIO/RTO heterostructures (R = Dy, Yb, Y), the RTO single crystals were first aligned by a HUBER Laue X-ray diffractometer and then cut into substrate pieces along the (111) lattice plane by using the Model 650 Low Speed Diamond Wheel Saw from South Bay Technology. All single crystal substrates are 0.5 mm thick. The substrate surfaces were prepared by mechanical polishing process with monocrystalline suspension. The surfaces were characterized by an MFP-3D Atomic Force Microscope from Asylum Research. Thin films of BIO were synthesized by Pulsed Laser Deposition. A KrF excimer laser ($\lambda = 248$ nm) was used at a repetition rate of 2 Hz and the laser beam fluency was 1.7 J/cm$^2$. The BIO films were deposited at 620 °C and 50 mTorr of oxygen pressure. The thickness was controlled by the nominal growth rate of BIO films at 40 pulses/nm and verified by *ex situ* x-ray reflectivity. After deposition, the films were cooled down in 50 mTorr of oxygen pressure.

For BIO/DTO/YSZ heterostructure, Yttria Stabilized Zirconia(YSZ) with (111) out-of-plane orientation is the commercial one from CrysTec company. Thin film samples were synthesized by Pulsed Laser Deposition. A KrF excimer laser ($\lambda = 248$ nm) was used at a repetition rate of 2 Hz and the laser beam fluency is 1.7 J/cm$^2$. The DTO films were first deposited at 800 °C and 0.0133 mbar of oxygen pressure. The

BIO films were then deposited at 620 °C and 0.0667 mbar of oxygen pressure. The thickness was controlled by the nominal growth rate of BIO films at 40 pulses/nm and DTO films at 120 pulses/nm, which were verified by ex situ x-ray reflectivity. After deposition, the films were cooled down in 0.0667 mbar oxygen pressure.

## 2.2 Heterostructure characteristics

### 2.2.1 X-ray diffraction

The structure of polycrystalline RTO is characterized by X-ray powder diffraction. The quality is indicated by $\chi_2$ value after refinement using FullProf_Suite software. The heterostructure is characterized by X-ray diffraction (XRD) and X-ray reflectivity (XRR). For XRR, interference between the film-reflected x-ray beam and the substrate-reflected x-ray beam creates a reflectometry pattern, which determines the thickness of the film. For XRD, constructive interference of scattered X-ray beam happens when the angle satisfies: $n\lambda = 2d_{hkl}\sin\theta$, where $d_{hkl}$ represents the distance between crystallographic planes (h,k,l).

In-house heterosturcture X-ray characterization was done by an X'Pert3 MRD machine. Synchrotron heterosturcture X-ray diffraction was performed at beamline 33-BM at the Advanced Photon Source at the Argonne National Laboratory. The film thickness was extracted from fitting the X-ray reflectivity (XRR) curve. XRR curve is fitted with a model of one homogeneous layer on a substrate. The calculation of the theoretical curve was based on the dynamical theory of X-ray scattering applied on the model of a flat homogeneous slab of given thickness grown on a flat substrate. The surface and interface roughness was included in the model using the distorted-wave Born approximation approach.

### 2.2.2 Resistivity and magnetoresistance measurements

Transport measurement was performed using four-points resistance measurement. Transport measurement above 2 K was performed with a Physical Properties Measurement System (PPMS) from Quantum Design (QD). Transport measurements from 30 mK to 1.0 K were measured in SCM1 at the National High Magnetic Field Laboratory (NHMFL). To change the magnetic field at sub-Kelvin at the NHMFL, the measurements were performed with a slow field sweeping rate at 0.2 T/minute. The trapped flux inside the magnet also leads to a hysteresis around 0.05 T. No significant MR hysteresis within this measurement precision was observed. To vary the field direction at a fixed field strength, the angle-dependent measurements were performed with a low sweeping rate at 2 degrees/minute. All data were measured by utilizing the lock-in technique. The typical applied current was at the order of 10 nA, with a frequency $< 30$ Hz. Samples used in the measurements are of 3 mm (W) $\times$ 3 mm (L) in dimension.

### 2.2.3 AC susceptibility

AC magnetic susceptibility measurement is used to detect the magnetic phase transition with an oscillating external magnetic field of a certain frequency. Two coils are set around the sample. The primary coil applies the oscillating magnetic field while the second one measures the induced voltage, which is proportional to the frequency, change of time-varying magnetic moment and AC field amplitude. If the AC field is small (usually 0.1Oe to10Oe) and only linear response is considered, the induced AC moment is $M_{AC} = (dM/dH) \cdot H_{AC} sin(\omega t)$, which represents the slope of the M(H) curve.

AC susceptibility was measured at NHMFL. The AC susceptibility measurements were conducted with a voltage-controlled current source (Stanford Research, CS580) and lock-in amplifier (Stanford Research, SR830). The phase of the lock-in amplifier was set to measure the first harmonic signal. The rms amplitude of the AC excitation

field was set at 0.35 Oe with the frequency fixed at 470 Hz. The measurement at NHMFL mainly focused on identifying magnetic transitions rather than obtaining absolute magnetic susceptibility values. The unit of the AC susceptibility data was given in arbitrary units because the AC susceptometer was not calibrated within the scope of the experiment. AC susceptibility was measured for YbTO and YbTO-ns seperately, and the transition temperature $T_c$ was defined as the peak position of AC susceptibility.

### 2.2.4 Capacitive torque magnetometry measurements

AC susceptibility is an effective way to probe the magnetic dynamics in crystal. However, this is hardly used to detect magnetic properties in the crystalized film due to its small volume. Torque magnetometry is a good way to measure the anisotropic magnetic response at low temperature. Unlike the AC susceptibility method, it doesn't directly measure the magnetization, but it can reflect the magnetic phase transition in an anisotropic system. Fig. 2.2(a)-(b) shows the setup of cantilever-based torque magnetometry [38]. The measurement quantity here is the capacitance between the cantilever and the gold film, which reflects the deflection of the cantilever. The choice of cantilever type depends on the sample's magnetization: usually for film sample with small magnetization, we choose the thinner cantilever which can be bent easily. The deflection of the cantilever depends on the normal torque value and intrinsic property of the cantilever material: $\tau = -\kappa\delta\theta$. The capacitance is given by: $C = \frac{\epsilon_0 S}{d}$, so the change of capacitance within a small angle is: $C - C_0 = \delta C = \frac{\epsilon_0 S}{d^2}\delta d = \frac{\epsilon_0 S}{d^2} l\delta\theta$. Combining the expression of torque value and the change of capacitance, the torque value is proportional to the capacitance change. For the heterostructure BIO/DTO/YSZ, the transport measurement of BIO film and the torque magnetometry measurement of DTO film can be simultaneously measured, as shown in Fig. 2.2(c).

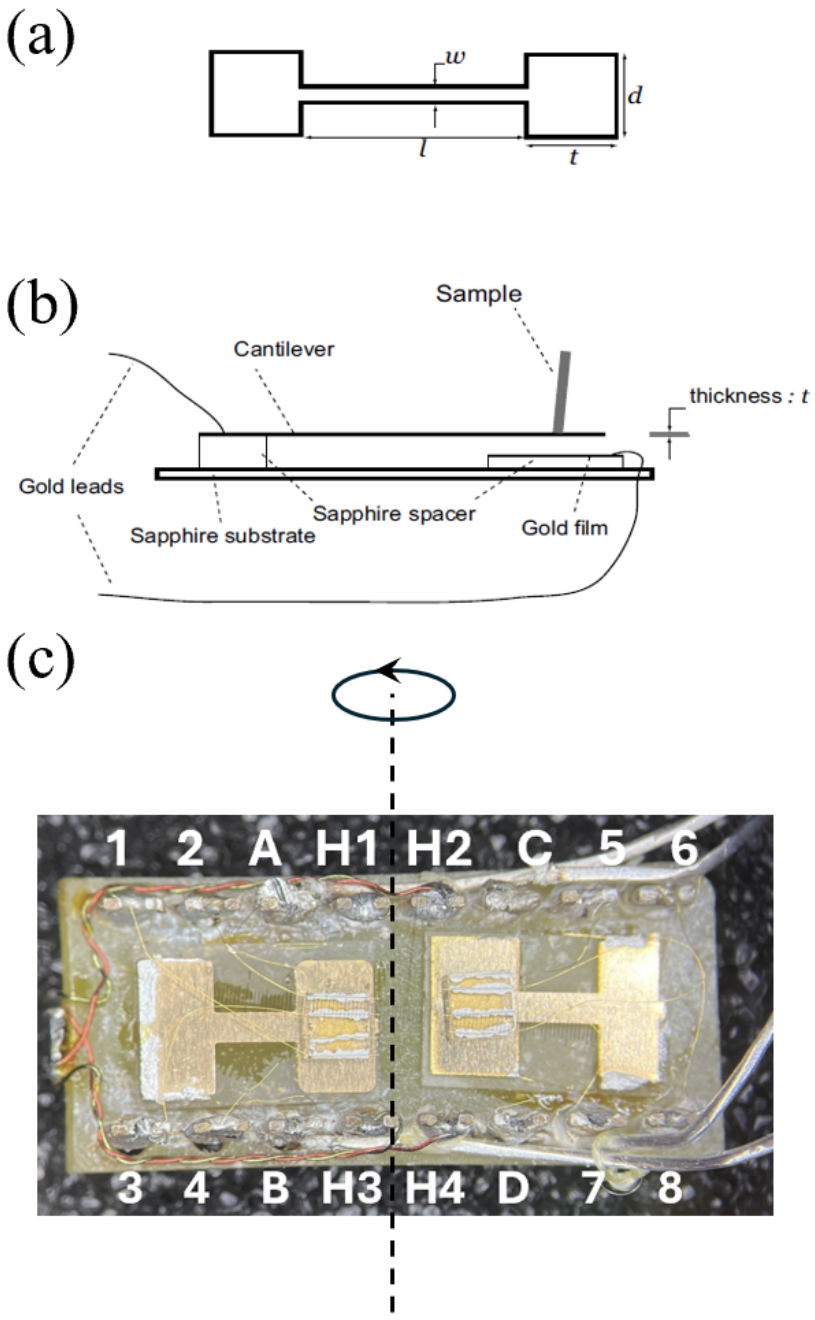


**Figure 2.2:** (a): Shape of the cantilever in the torque magnetometry tenique [38]. (b): Schematic of torque magnetometry setup [38]. (c): Setup of simultaneous measurements of torque responses and resistivity.

# Chapter 3

# Anomalous Magnetoresistance by Breaking Ice Rule in $Bi_2Ir_2O_7/Dy_2Ti_2O_7$ Heterostructure

## 3.1 Introduction

Novel emergent states of quantum magnets often arise from geometric frustration, where local spins residing on the corners of a triangle or tetrahedron cannot agree on any alignment that simultaneously minimizes their energies [2]. Such a spin lattice has a large degree of degeneracy due to an enormous number of configurations at the same or similar energy, leading to exotic ground states, entangled fluctuations, and collective excitations [39, 40, 41, 42, 43, 44], such as magnetic monopole and spinon, which may afford revolutionary quantum technologies [45, 13, 46]. The so-called dipolar spin ice is one of the most iconic representatives of such frustrated magnets. It was first discovered on pyrochlore lattices of Ising spins constrained along the local [111] direction, such as $Ho_2Ti_2O_7$ and $Dy_2Ti_2O_7$ [6, 47, 3]. While the spin-spin

correlation is dominated by the dipolar interaction, the ferromagnetic instability is geometrically frustrated by the local Ising anisotropy [2]. As a result, the ground state of each tetrahedron settles in one of the six-fold degenerate 2-in-2-out configurations, forming a spin ice network throughout the lattice following the ice rule in analog with the proton displacement in the water ice [48]. The non-zero residual entropy has indeed been observed with a value close to that in the water ice [9]. Breaking the ice rule could lead to rich spin dynamics, including emergent magnetic monopoles [12]. For instance, applying a magnetic field along the pyrochlore [111] direction turns the three-dimensional spin ice into a Kagome spin ice [49], and eventually stabilizes the 3-in-1-out/1-in-3-out configuration by condensing the monopoles [2, 39, 50], giving rise to a jump from 3.3 μB/Dy to 5 μB/Dy in $Dy_2Ti_2O_7$ between two magnetization plateaus [51]. The 3-in-1-out/1-in-3-out state is effectively a magnetic charge-ordered state, which is also called the saturated ice [52] where the ice rule is broken everywhere.

However, the spin-ice behaviors have been only observed in highly insulating compound [2, 39, 6], where the spins are hosted by highly localized electrons in the absence of itinerant carriers, such as the f-electrons of $Ho^{3+}$ or $Dy^{3+}$ ions in combination with the empty d-shell of the $Ti^{4+}$ valence state in the pyrochlore titanate [6, 47, 3]. When introducing itinerant carriers, simply replacing the B-site with another element with a metallic configuration often ends up interfering the spin ice state. For instance, the correlated d-electrons in pyrochlore iridates not only exhibit an all-in-all-out ordering of their own at much higher temperatures, but also force the same magnetic order onto the A-site sublattice regardless of the rare earth element [53]. In some cases, the interactions within the rare earth sublattice may modify the transport properties of the d-electron [54, 30, 55] at lower temperatures, such as the fragmented monopole crystal ground state [56] as well as the monopole-density-related magneto-transportation [57]. However, the spin state of the rare earth sublattice is often impaired by the energy scale of the d-electrons, which is much larger than the interaction. This situation indeed applies to a broad class of frustrated magnets beyond spin ice.

In this work, we report the observation of an anomalous magnetoresistance (MR) in epitaxial pyrochlore heterostructures of $Bi_2Ir_2O_7/Dy_2Ti_2O_7$ (BIO/DTO), where DTO hosts the spin ice state and BIO, the only nonmagnetic/time-reversal-invariant member of the pyrochlore iridate series, provides the correlated carriers. We directly grow ultrathin BIO films on DTO single crystals as illustrated in Fig. 3.1. A cusp-like MR anomaly is observed, when the field induces the transition between the Kagome spin ice state and the saturated ice. These results demonstrate an epitaxial interface approach for enabling charge responses and detection of the exotic spin state transitions in insulating frustrated magnets.

## 3.2 Results

DTO single crystal substrates were prepared by the floating zone method [33]. The crystals were first oriented and cut into substrate pieces along the DTO (111) lattice plane. The substrate surfaces were then polished through a five-step process (see details of experimental method in chapter 2) to achieve atomically flat surfaces. Fig. 3.1(c) shows a typical atomic force microscope (AFM) image of the DTO single crystal substrate surface after the process, with a root mean square surface roughness of 1.21 Å. Thin BIO layers were deposited on the DTO substrates by pulsed laser deposition [37]. The BIO/DTO interface was examined with the scanning transmission electron microscopy (STEM). A typical cross-section image in Fig. 3.1(d) shows a sharp epitaxial interface. Energy dispersive X-ray spectroscopic (EDS) map (Fig. 3.2) further confirms no significant interdiffusion across the interface. Fig. 3.1(e) shows a typical specular X-ray diffraction scan covering the DTO [222] to [444] structural peaks, which are accompanied with the corresponding peaks of a BIO film of 3.4 nm, confirming the epitaxial growth. Representative reciprocal space mapping (RSM) shows that the BIO film is in a fully strained state (Fig. 3.3(a)). The film thickness is extracted from fitting the X-ray reflectivity curve (Fig. 3.3(b)&(c)), which also yields a film density consistent with expectation.

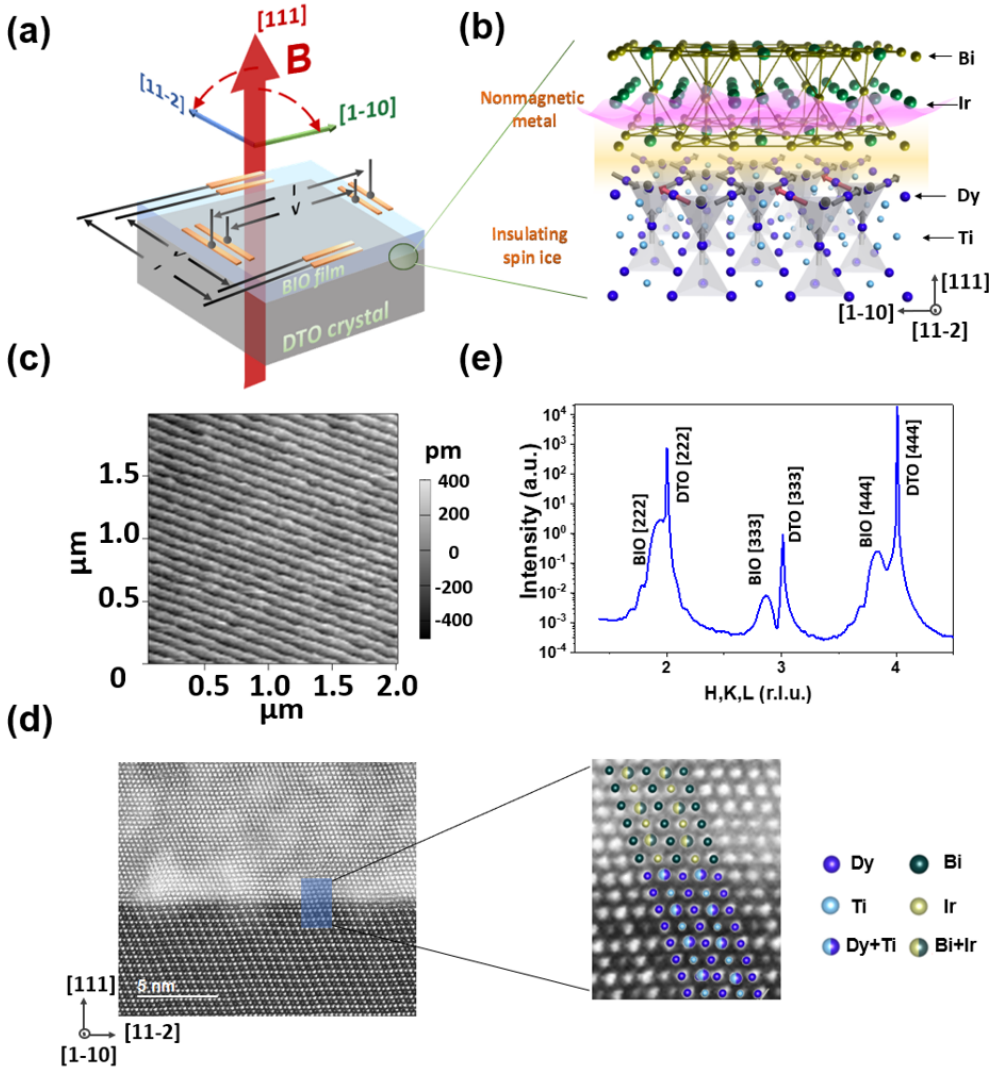


**Figure 3.1:** $Bi_2Ir_2O_7/Dy_2Ti_2O_7$ heterostructure. (a) Schematic diagram of the $Dy_2Ti_2O_7/Bi_2Ir_2O_7$ heterostructure and the measurement configuration. (b) A schematic drawing showing a zoomed region across the interface. The local spins (grey) are shown on the DTO sides with a few of them (red) flipped to break the ice rule and form the '3-in-1-out/1-in-3-out' configuration. A wavy surface curve (pink) is shown on the BIO side to denote charge carrier. (c) A typical AFM image of DTO substrate surface with atomically flat terraces. (d) Transmission electron microscopy image with [1-10] being the lamella surface normal shows the sharp BIO/DTO interface of the heterostructure. The white patches are from focus iron beam milling. A thicker film sample with thickness 10.5nm was used in the TEM study to protect the interface. (e) An X-ray diffraction scan covering the DTO [222] to [444] peaks of a BIO/DTO heterostructure.

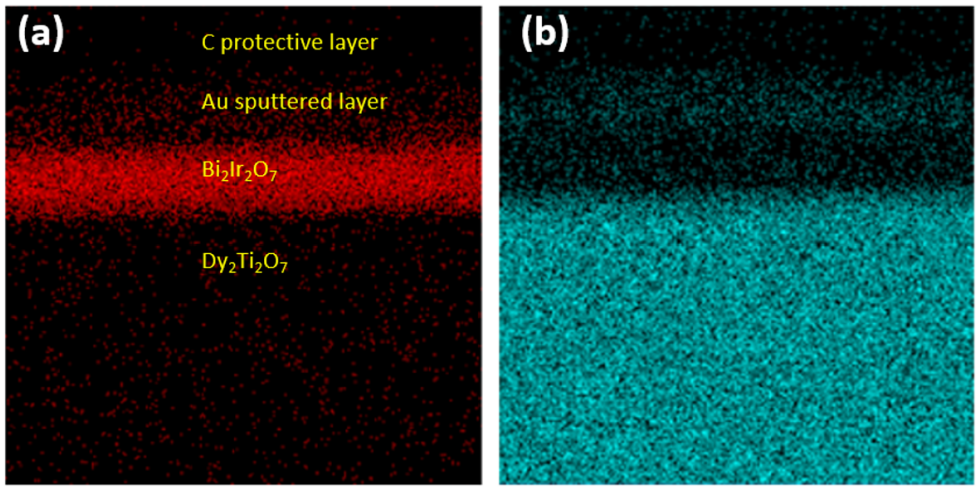


**Figure 3.2:** Energy dispersive spectroscopy images. (a) Bi EDS map; (b) Dy EDS map. The EDS results demonstrate that there is no significant interdiffusion across the interface.

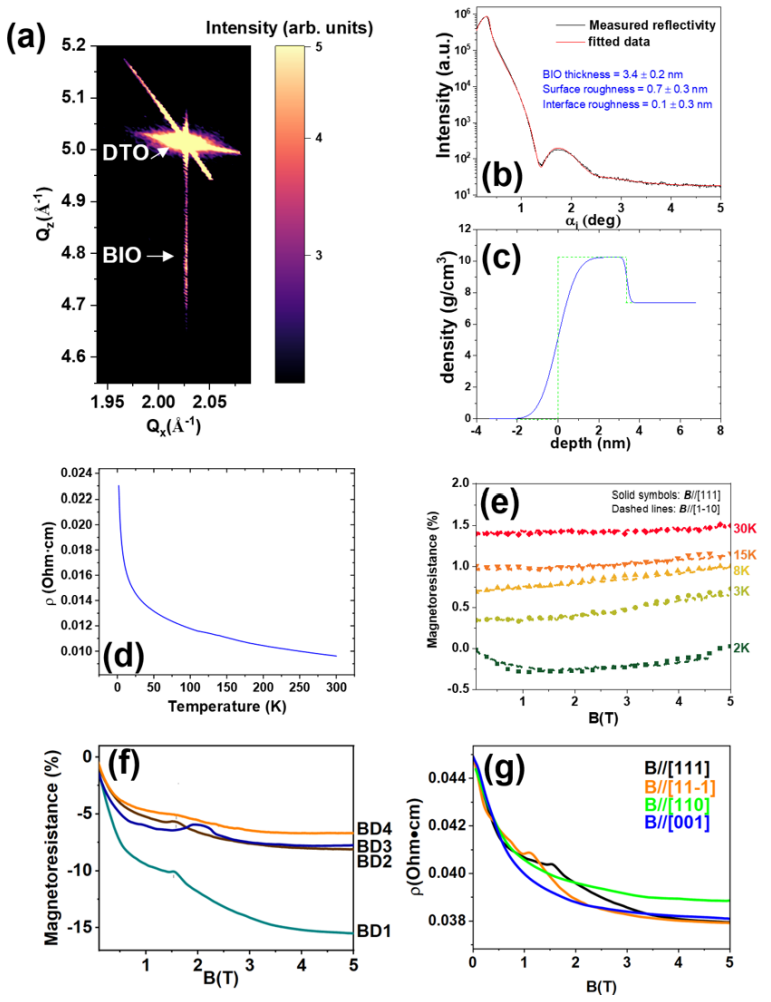


**Figure 3.3:** Additional characterization of the BIO/DTO (BD1) heterostructure. (a) Reciprocal Space Mapping near the DTO [266] reflection, showing the BIO film is fully strained. Here, $Q_x$ and $Q_z$ are the components of the reciprocal space vector along the [-211] and [111] directions, respectively. (b) Representative XRR data. (c) The blue curve shows the resulted depth profile of mean density (i.e. laterally averaged). The depth profile for the undisturbed system prior to including roughness is plotted by the dashed green curve indicating the positions of the surface and the layer/substrate interface. (d) Temperature-dependent resistance from 300 K down to 2 K. (e) Magnetoresistance from 30 K to 2 K is similar between B//[111] and B//[1-10]. A vertical offset was applied for clarity purpose. (f) Magnetoresistance for BIO/DTO (BD1) heterostructures compared with BD2, BD3 and BD4 of similar BIO thickness at 0.03 K. The field direction of the BD3 sample has a 5-degree offset which causes the anomaly to appear at a slightly higher field. (g) Magneto-transport measurement reproduced from Fig. 3.4(d) without the vertical offset, where the magnetoresistance shown in percentage ratio is replaced by the measured resistivity here.

While the all-in-all-out magnetic ordering of the Ir pseudospin-1/2 electrons in the pyrochlore iridates has an increasing ordering temperature with decreasing A-site ionic radius [58], BIO is a bad metal on the paramagnetic side of the quantum critical point [59]. No magnetic ordering or spontaneous time-reversal-symmetry-breaking was found down to 50 mK [29]. Moreover, it has been shown that, although the BIO metallicity will degrade when grown as ultrathin films likely due to weak localization and/or disorder-enhanced electron-electron interaction in two-dimensions, the MR remains rather isotropic when the field is applied along different crystallographic axes [28]. Our ultrathin BIO films on DTO indeed show a weakly increasing resistivity with lowering temperature as well as an isotropic MR (Fig. 3.3(d)&(e)), consistent with previous reports [28]. No temperature-induced transition is observed, indicating that the BIO film remains nonmagnetic. However, an emergent anisotropic anomaly was observed while measuring MR below 1 K. Fig. 3.4(a)&(b) shows MR measurements at 0.03 K with the magnetic field **B** along different directions in the (11-2) plane, while the current is always along the [11-2] axis perpendicular to the field (Fig. 3.1(a)). One can see the overall MR response with **B**//[111] is similar to **B**//[1-10] except a positive cusp-like anomaly around 1.5 T. This anomaly was confirmed in multiple samples (Table 3.1 and Fig. 3.3(f)). It can also be seen that the anomaly has a reduced size in samples with a much thicker BIO film, indicating that the anomaly is caused by the interface with DTO (Table 3.1 and Fig. 3.5(a)). Our AC susceptibility measurement, where the signal is dominated by the bulk of the DTO substrate, shows that this field corresponds to the critical field $B_c$ of the Kagome spin ice-to-saturated ice transition of DTO, and it is higher than the intrinsic value of $B_c \sim 1$ T [52] due to the demagnetization effect of the plate-shape of the crystal substrate (see Fig. 3.1(a) & Fig. 3.6).

Moreover, as we rotate B away from [111], the anomaly displays a clear shift to higher fields with the width of the feature being broadened as well, which is consistent with the fact that the field projection to [111] is decreasing as the field angle increases. A larger external field is thus needed to induce the transition in DTO, and the finite

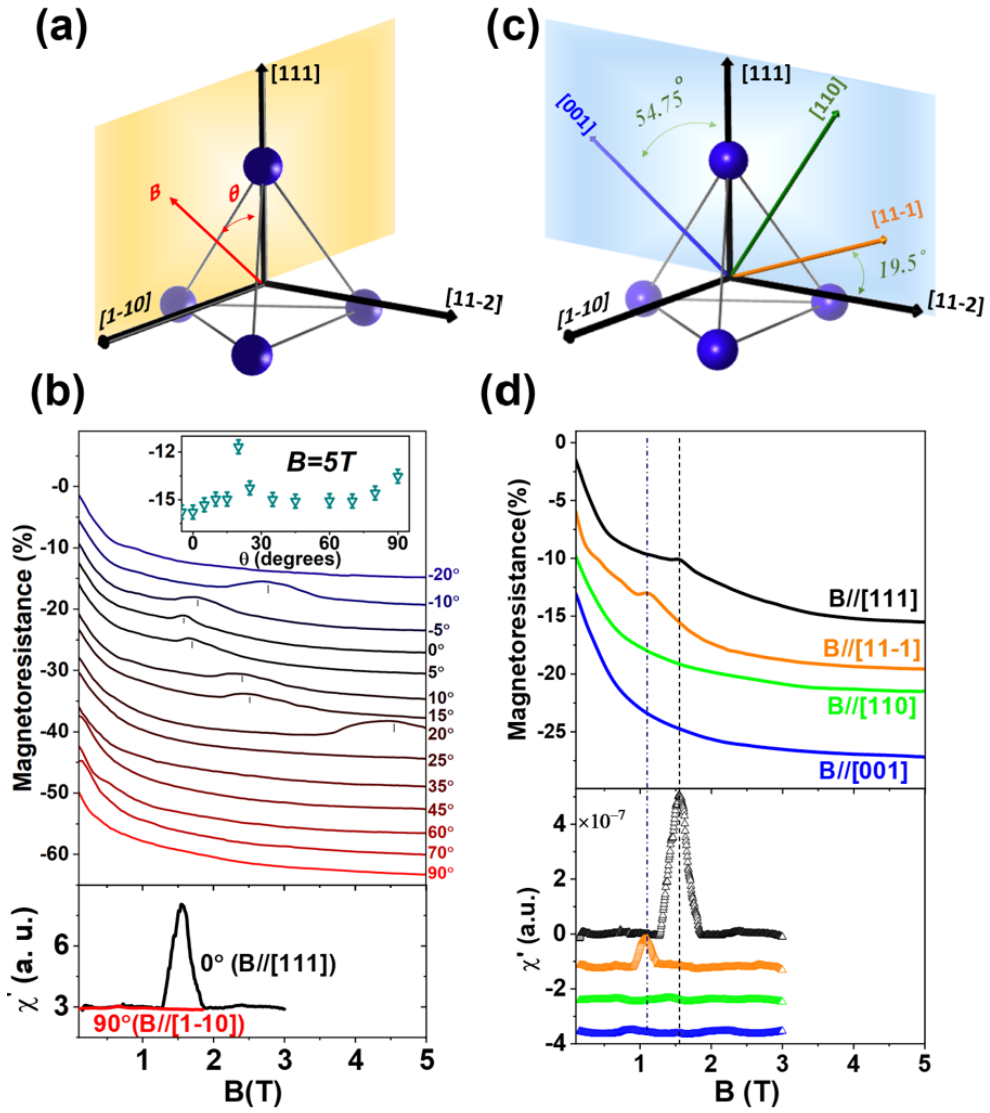


**Figure 3.4:** Magnetoresistance anomaly. (a) Geometric diagram of the MR measurement with **B** in the (11-2) plane, where $\theta$ is the field angle respected to the [111] direction. MR is defined as $\mathrm{MR} = (\mathrm{R(B)} - \mathrm{R_0})/\mathrm{R_0} \times 100\%$, where $\mathrm{R_0}$ is the zero-field resistance. (b) MR (top) and AC susceptibility (bottom) at 0.03 K at selected angles; inset illustrates the MR at each angle when B=5 T. (c) Geometric diagram of the MR measurement with B in the (1-10) plane, which contains four high-symmetry axes. (d) MR (top) and AC susceptibility (bottom) at 0.03 K along the high-symmetry axes in this geometry. Vertical offsets are applied on the curves for clarity.

**Table 3.1:** Sample Information. List of synthesized heterostructures and details about their observed MR anomaly. The anomaly of each sample was refined with a Gaussian function to extract the position and the full-width-at-half-maximum (FWHM). The absolute and relative MR anomaly amplitude were also calculated and provided in the last two columns. The field direction of the BD3 sample has a 5-degree offset which causes the anomaly to appear at a slightly higher field.

| Sample Name | Formula | Film Thickness (nm) | Field Value at which the MR Anomaly Peak Occurs (T) | FWHM (T) | MR peak amplitude (%) | Relative peak amplitude (%) |
|---|---|---|---|---|---|---|
| BD1 | $Bi_2Ir_2O_7$/ $Dy_2Ti_2O_7$ | 3.4 | 1.56 | 0.359 | 0.622(5) | 0.690(6) |
| BD2 | $Bi_2Ir_2O_7$/ $Dy_2Ti_2O_7$ | 3.2 | 1.61 | 0.276 | 1.098(6) | 1.231(7) |
| BD3 | $Bi_2Ir_2O_7$/ $Dy_2Ti_2O_7$ | 3.9 | 2.03 | 0.540 | 0.912(3) | 0.981(3) |
| BD4 | $Bi_2Ir_2O_7$/ $Dy_2Ti_2O_7$ | 4.0 | 1.60 | 0.601 | 0.184(5) | 0.195(5) |
| BD5 | $Bi_2Ir_2O_7$/ $Dy_2Ti_2O_7$ | 23.8 | 1.65 | 0.22 | 0.060(5) | 0.062(5) |
| BD6 | $Bi_2Ir_2O_7$/ $Dy_2Ti_2O_7$ | 41.4 | | | | |
| BY1 | $Bi_2Ir_2O_7$/ $Y_2Ti_2O_7$ | 3.7 | | | | |

*MR peak amplitude = MR at the anomaly peak - background MR
*Relative peak amplitude = (MR at the anomaly peak - background MR) / |background MR|

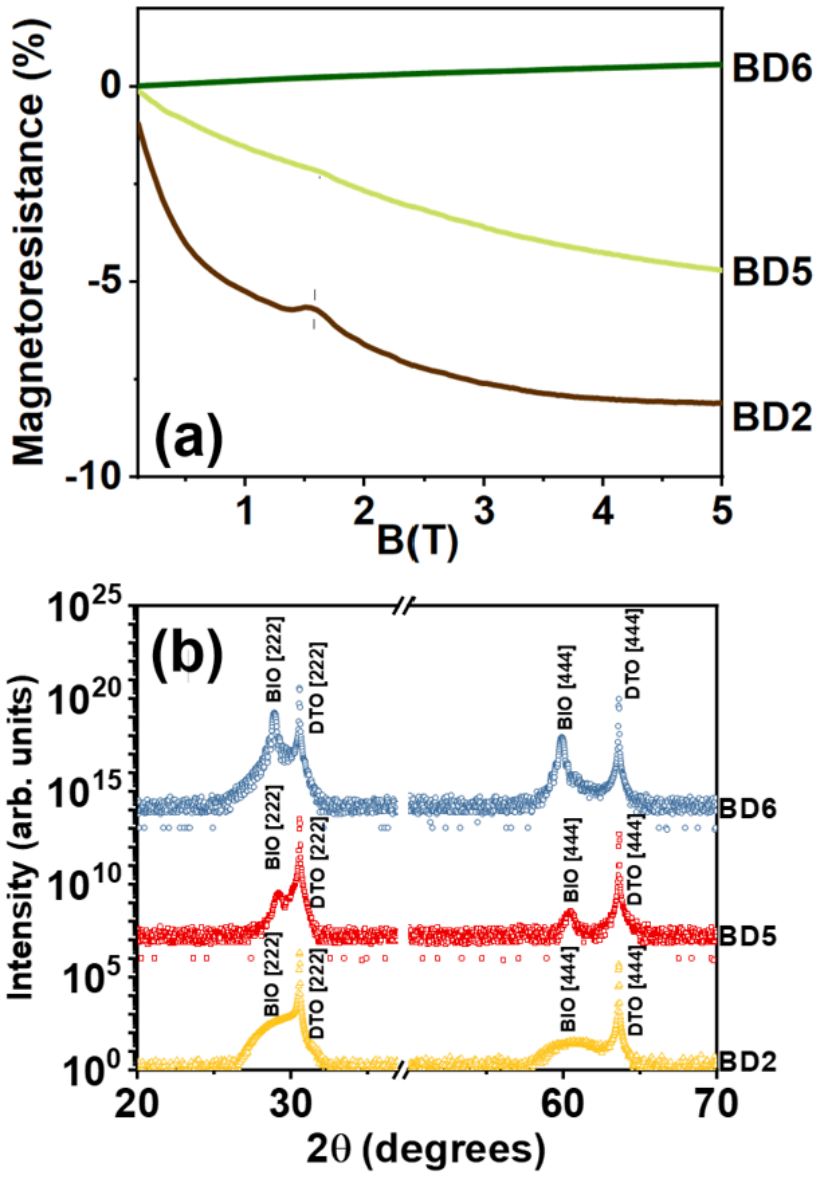


**Figure 3.5:** BIO/DTO heterostructures with different BIO thickness. (a) Magnetoresistance at 0.03 K for the BD2, BD5 and BD6 heterostructures, respectively. (b) Theta-2theta scans for samples BD2, BD5 and BD6.

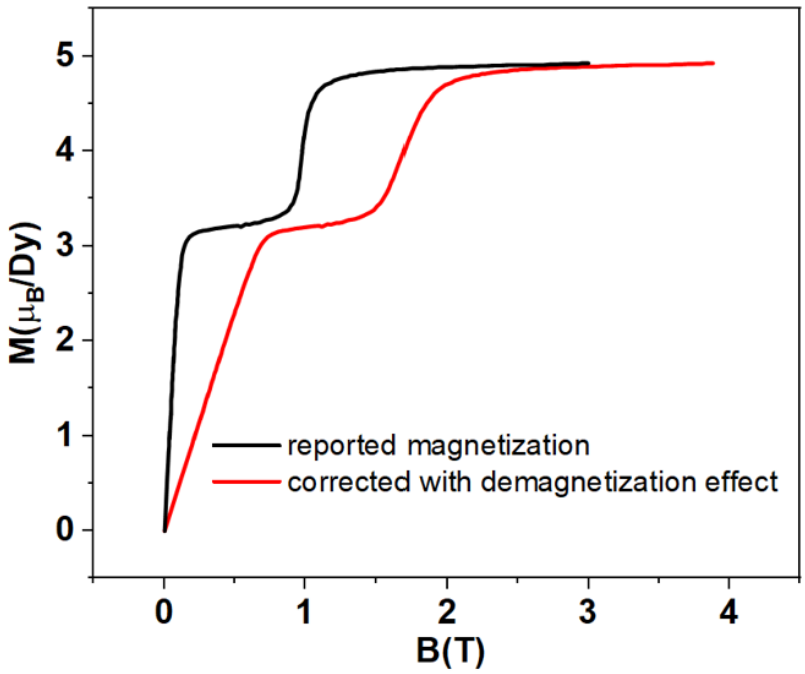


**Figure 3.6:** Correction of the demagnetization field. The reported magnetization [51] of bulk DTO with B//[111] at 0.48 K (black) is used to estimate the demagnetization effect, where the demagnetization factor is calculated to be 0.84 based on the dimensions of the DTO substrate. It can be seen that, when plotting the magnetization against the total external field applied (red), the original ice-rule-breaking transition at 1 T is shifted to 1.5 T, consistent with the reported MR anomaly in this work.

width of the transition is effectively stretched. Moreover, the observed increase is rapid and clearly does not follow any simple cosine function, which is a signature of the field-induced transition in spin ice due to geometric frustration [60, 61]. Deriving $B_c$ from the dipolar spin ice model indeed shows that $B_c$ diverges when the field deviates from [111] by $\sim 20°$ (Fig. 3.7), which is consistent with the fact that the anomaly is quickly shifted beyond the measured field range and the shape of the MR curve by that point is virtually the same as that with **B**//[1-10]. (The asymmetric behavior between the positive and negative angles is due to a small instrumental misalignment $\sim 2°$, see Fig. 3.7 for details). The angle-controlled transition is further illustrated in the inset of Fig. 3.4(b), where the MR at 5 T is extracted and plotted against the field angle from [111] ($\theta = 0°$) to [1-10] ($\theta = 90°$). One can see a sharp increase of the resistivity around the critical angle $\theta_c \sim 20°$ due to the anomaly. Interestingly, the resistivity on both sides of $\theta_c$ shows a much smaller but visible difference, which can be attributed to the fact that DTO remains a spin ice at 5 T with $\theta > \theta_c$ while becoming a saturated ice with $\theta < \theta_c$. The remnant spin disorder in the former is likely to elevate the resistivity compared with the latter.

Fig. 3.4(c)-(d) shows representative MR curves of the BIO/DTO heterostructure at 0.03 K measured in another configuration where B is applied in the (1-10) plane with current along the [1-10] axis (Fig. 3.1(a)). This setup allows the field to access multiple high-symmetry axes, including [110], [11-1], and [001], in addition to [111] as shown in Fig. 3.4(c). One can see that, while the overall MR response remains similar for all directions, the MR curve with **B**//[11-1] clearly shows an extra positive anomaly that is absent with **B**//[110] and **B**//[001] but is similar to the case of **B**//[111]. This observation is consistent with the fact that [111] and [11-1] are two equivalent axes in DTO. The difference is that the anomaly with **B**//[11-1] is at 1 T, which is lower than that with **B**//[111] and close to the intrinsic $B_c$. We again confirmed this behavior by AC susceptibility measurements, which show in the bottom panel of Fig. 3.4(d) that the peaks in correspondence to the transition for **B**//[111] and **B**//[11-1] indeed occur at different fields and match the fields of their

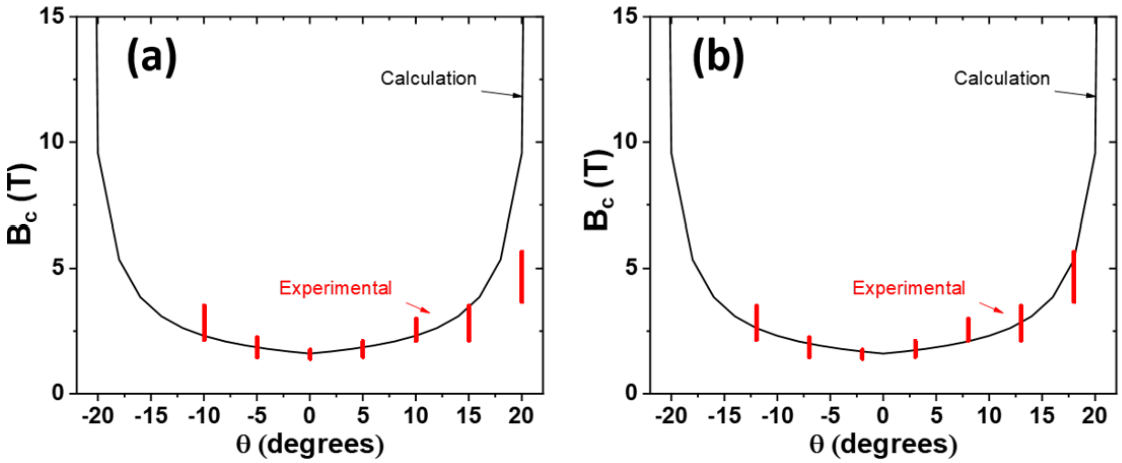


**Figure 3.7:** Shift of the critical field. (a) Shift of the MR anomaly when the magnetic field deviates from the [111] axis (extracted from Fig. 3.4(b)); and (b) the result after correcting a 2° misalignment. The red vertical lines mark the region of the MR anomaly at each field direction.

MR anomalies, respectively. The shift of $B_c$ between [111] and [11-1] is attributed to the much stronger demagnetization effect for the surface normal direction [111]. By comparison, the AC susceptibility is featureless for **B**//[110] and **B**//[001]. All the observations above corroborate that the MR anomaly of the BIO layer is indeed a result of the field-induced ice-rule-breaking transition in the insulating DTO substrate and is remarkably sensitive to any shift of $B_c$. Note that the observed positive cusp-like anomaly cannot be attributed to the DTO stray field on BIO because the magnetization jump of the DTO transition would increase the effective field on BIO and lead to a negative step-like MR jump instead. In addition, the resistivity at 5 T with **B**//[110] is also larger than that of **B**//[111] and [11-1] (Fig. 3.3(g)), consistent with the impact of the remnant spin disorder in the spin ice state as discussed with the previous configuration.

## 3.3 Discussion

This result demonstrates that forming a heterostructure can effectively introduce interactions between the charge carriers from one side and the frustrated spins on the other side. The excellent consistency in the critical field between MR and the bulk-sensitive AC susceptibility reveals the robustness of this method. Note that the field, regardless of its direction, always locally flips the moments to partially lift the 2-in-2-out degeneracy of the Dy tetrahedron within the spin ice state. Yet the MR anomaly only occurs when the transition to the saturated ice state is induced, indicating that the charge carriers are particularly sensitive to the ice-rule-breaking spin flips. Given that the Kagome spin ice-to-saturated ice transition is a first order transition [2, 51, 52], a phenomenological mechanism of the anomalous MR responses can be depicted with the coexistence of the two spin states in the Kagome plane perpendicular to the field (since the triangular plane is polarized in both cases). As illustrated in Fig. 3.8(a), a boundary of the two regions is defined by the spins that connect tetrahedra hosting the 2-in-2-out and 3-in-1-out/1-in-3-out configuration

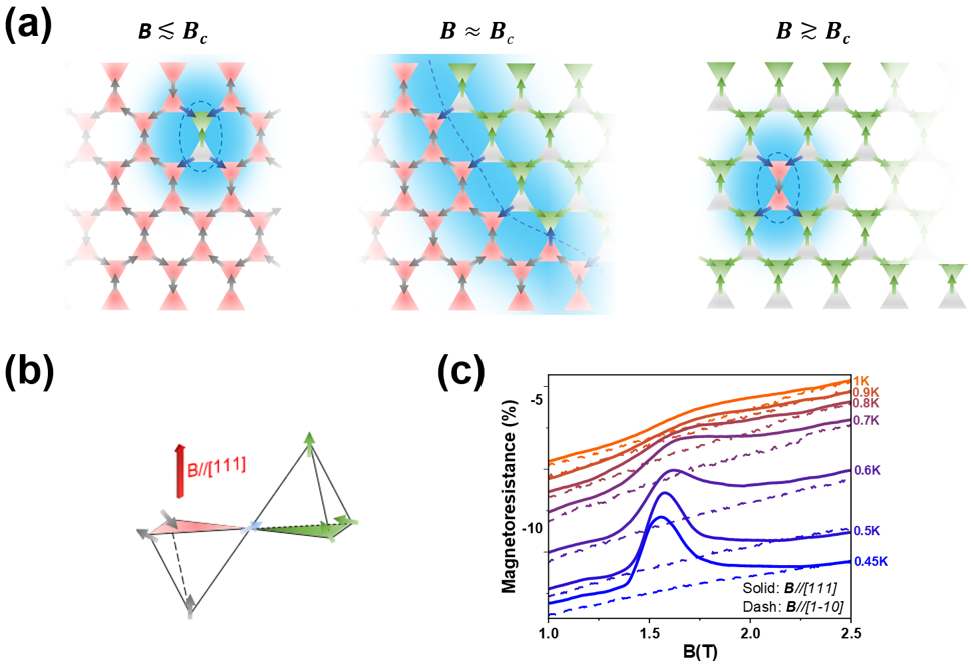


**Figure 3.8:** Phenomenological mechanism. (a) Schematics showing the boundary in the Kagome layer between the Kagome spin ice and the saturated ice state. The tetrahedra with the 2-in-2-out configuration and the 3-in-1-out (1-in-3-out) configuration are in red and green, respectively. The blue arrows denote the sites that connect the two regions with the area highlighted in light blue indicating the boundary region where the spins are less stable. A three-dimensional schematic is showed in panel (b) for a pair of the tetrahedra across the boundary. (c) MR in the region of the anomaly from 0.45 K to 1 K. The solid and dashed lines were measured with **B**//[111] and **B**//[1-10], respectively. The curves are vertically shifted for clarity and comparison purposes.

(Fig. 3.8(b)), respectively. The spins nearby the boundary are most unstable and fluctuating, thus potentially introducing extra scattering to the charge carriers when entering one region from another which increases the resistivity. Fig. 3.8(a) shows a cartoon of how the density of these boundaries may increase and decrease across the critical regime, capturing the enhanced resistivity during the transition manifested by the positive sign and the cusp shape of the anomaly. As discussed earlier in the angle-dependent data, although the different degrees of spin disorder of the two states may still induce a difference in the resistivity outside the transition region, this effect is smaller than the anomaly likely due to the fact that local moments are more stable away from the transition.

To further verify this picture, we measured a 3.7 nm BIO film on nonmagnetic $Y_2Ti_2O_7$ substrate as a reference sample and observed isotropic MR as functions of temperature and magnetic field without any anomaly (Fig. 3.9). This comparison confirms that DTO influences the transport properties of the BIO film mainly in its transition regime. In other words, the anomaly is a charge response to the magnetic fluctuations in the transition region, and it has a peak-like line shape similar to the AC susceptibility. Although a microscopic theory is yet to be developed to describe the interaction of the Dy moment and the BIO carriers, it likely depends on the hybridization between the localized f-states at the Dy sites and the itinerant states of Ir d-electrons since such an interaction is usually captured by the Anderson Model [62, 63] for metals with local moments. The difference here is that the localized moments and the itinerant carriers are on opposite sides of the heterostructure and they couple across the interface. We note that the spin Hall effect (SHE) in metals may also produce anisotropic MR responses through the so-called spin hall magnetoresistance when in direct contact with an insulating magnet [64]. However, SHE does not require the field-induced transition and does not account for the fact that the anomaly only occurs near the critical field of the transition, excluding SHE and any other process irrelevant to the field-induced transition from being the underlying mechanism. In fact, spin hall magnetoresistance requires an orthonormal

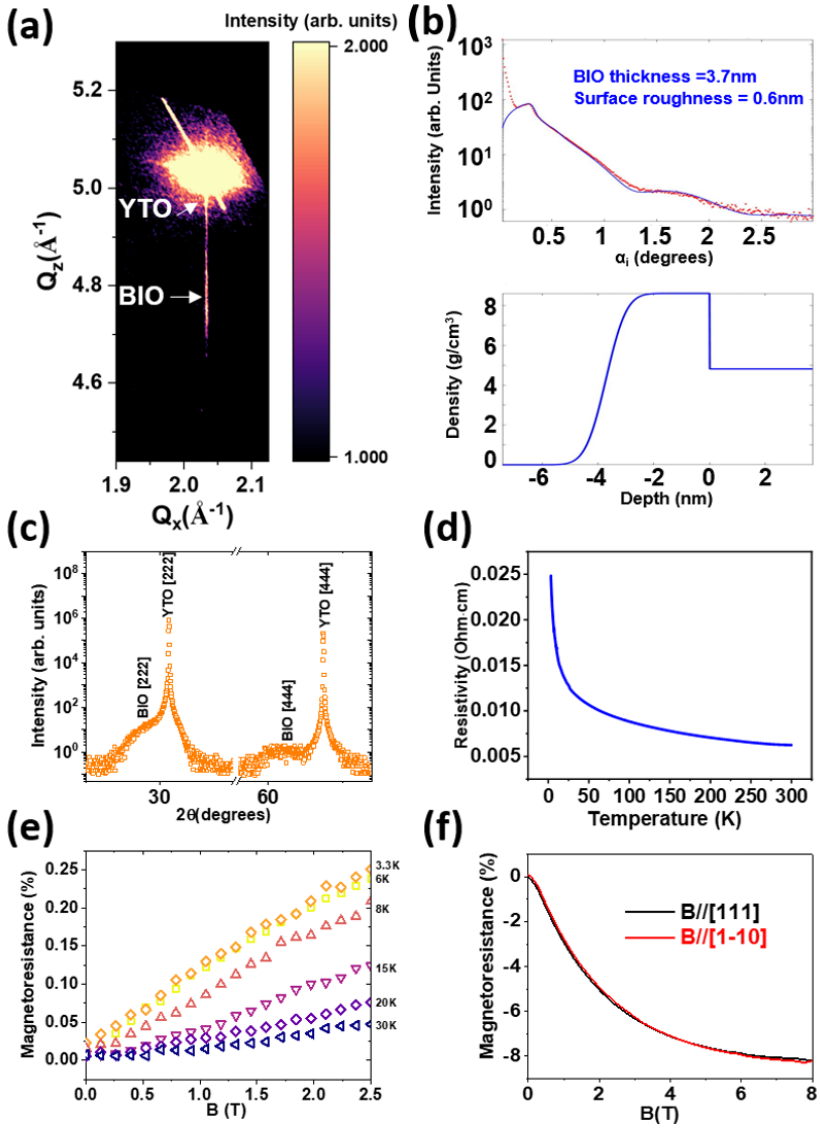


**Figure 3.9:** Characterization of the $Bi_2Ir_2O_7/Y_2Ti_2O_7$ (BY1) heterostructure. (a) Reciprocal Space Mapping near the YTO [266] reflection, showing the BIO film is fully strained. Here, $Q_x$ and $Q_z$ are the components of the reciprocal space vector along the [-211] and [111] directions, respectively. (b) Representative XRR data and the resulted depth profile. (c) Theta-2theta scans covering the YTO [222] and [444] peaks. (d) Temperature-dependent resistivity and (e) Magnetoresistance above 2 K. (f) Magnetoresistance at 0.03 K. No difference is observed when the magnetic field **B** is applied along [111] (black) and [1-10] (red).

geometry among the surface normal, current direction and magnetization, which is obviously unnecessary for the observed anomaly in the BIO/DTO heterostructure. In addition, the observed anomaly could not be attributed to the magnetocaloric effect as it is expected to cause responses of opposite signs when sweeping the magnetic field upward and downward, which was not observed in our experiment.

Studies of the field-temperature phase diagram of spin ice have shown that the field-induced phase boundary is terminated at elevated temperature and the transition becomes a continuous crossover as there is no sharp distinction between the Kagome spin ice and the saturated ice anymore [39, 51]. This behavior has been understood with an analogy to the liquid–gas transition in the context of a transition between a low-density phase and a higher-density phase of magnetic monopoles [12, 49, 50, 51]. For comparison, we studied the thermal evolution of the MR anomaly with $\mathbf{B}//[111]$ between 0.45 K and 1 K. The obtained result displayed as the solid lines in Fig. 3.8(c) shows that, while the anomaly overall remains around 1.5 T, it weakens in magnitude, broadens in width, and upshifts slightly in field with increasing temperature, likely due to the thermal broadening of the Kagome spin ice-to-saturated ice transition near its critical end point [2]. The dashed lines were measured with $\mathbf{B}//[1\text{-}10]$ and serve as a reference for comparison at each temperature. The anomaly eventually starts to vanish at $\sim$0.9 K and becomes hardly visible. These observations are consistent with the field-temperature phase diagram as well as the disappearing of the spin ice state in DTO due to thermal fluctuation [48, 9, 12] around 1K, confirming the sensitivity of the charge carriers to the abrupt change at the boundary between the two spin states until they are no longer distinguishable above the critical endpoint of the transition [51].

To summarize, the experimental observation of an emergent MR anomaly in BIO that responds to and closely tracks the Kagome ice-to-saturated ice transition in insulating DTO demonstrated that creating epitaxial heterostructures is a highly promising approach to introduce interactions between localized frustrated spins and correlated charge carriers. It opens the possibilities of electronically probing the

spin ice states under other control parameters, such as pressure and epitaxial strain [65, 66], as well as investigating charge conversion of the monopole condensation [12] excitations under non-equilibrium stimuli [67, 68]. Recently, the magnetic monopole dynamics was detected by a magnetization noise spectrometer in the spin ice state of DTO [69, 70, 71, 72] as well as during the transition between two 2-in-2-out states of artificial spin ice [73]. A two-dimensional monopole gas was also proposed at the heteroepitaxial interface of the 2-in-2-out state and the all-in-all-out [74]. Such behaviors may manifest in electronic transport, too, when interfaced with charge carriers, providing another detection method and a potential route to application. The interfacial approach can readily be extended to other non-conducting frustrated quantum magnets, such as spin liquid and quantum spin ice [2, 40, 41, 42, 43, 44, 45, 13, 46] for electronically detecting these exotic spin states and triggering electronic responses. The successful creation of functional heterostructure between DTO and BIO also showcases the potential of complex oxide heterostructures of the pyrochlore structure [75].

# Chapter 4

# Anomalous Proximitized Transport in Metal/Quantum Magnet Heterostructure $Bi_2Ir_2O_7/Yb_2Ti_2O_7$

## 4.1 Introduction

Spin-electronics roots in the dependence of electronic transport on the magnetization [76, 77]. This concept has been extended well beyond ferromagnets to antiferromagnets, ferrimagnets, and other magnets where the magnetic order can be described as a classical vector [78, 79, 80].Electronic transport can be controlled in such magnetic systems by reorienting the moments, which however must overcome energy barriers and inevitably cause power dissipation. Quantum mechanics, on the other hand, provides an attractive alternative for one spin state to transit to another spin state through quantum tunneling. Such quantum effect is one of the salient features of quantum magnets, where the magnetic state is a superposition of multiple distinct collective spin configurations due to quantum spin fluctuation (QSF) [81, 13, 44, 82].

Static magnetic orders are thus often strongly suppressed in quantum magnets, and the conventional quasiparticle picture [83] may break down in describing the low-energy excitations due to the absence of sharp spin waves. Indeed, exotic QSF-driven excitations are believed to be highly correlated and entangled, holding promises for quantum computation [84, 43, 44, 82, 13, 85, 86, 87], with spinon and Majornana fermion being two well-known examples that have been intensively studied in quantum magnets [88, 89, 90, 91, 92].

Despite the great technological potential [93], it is not yet clear how to exploit such many-body magnetic quantum effects to control electronic transport. A key reason is that the spin degree of freedom in most quantum magnets originates from strongly localized electronic states and they interact without free electrons [13, 94, 82, 95, 96]. In fact, many intriguing quantum magnets are good insulators. $Yb_2Ti_2O_7$ (YbTO) is an excellent example of such insulating quantum magnets [97, 98, 21, 17, 18, 16, 99], which is currently under extensive studies due to the proposed quantum spin ice state and multiphase competition [14, 100, 101, 15, 102]. Its ferromagnetic (FM) ground state is strongly suppressed [22] with very broad dispersive spin waves due to a significant mixture from antiferromagnetic (AFM) configurations [Fig. 4.1] alongside an intense flat mode near the spin-wave gap [26, 24, 103, 25]. This intriguing quantum dynamics arises from the strong QSF near the FM-AFM phase boundary [24, 103], and persists at finite temperatures even above $T_c$ [26, 104]. If an effective coupling to charge carriers can be introduced while preserving the quantum dynamics, one may exploit such QSF of local moments to mediate electronic transport for better understanding of the quantum magnetism and enabling new spin-electronic functionality.

Here we demonstrate proximitized electric transport for investigating and harnessing the quantum effects of YbTO crystals by forming an epitaxial heterostructure [Fig. 4.1] with ultrathin film of nonmagnetic metal $Bi_2Ir_2O_7$ (BIO). The feasibility of this hetero-epitaxial synthesis [105] was recently demonstrated between BIO and $Dy_2Ti_2O_7$ (DTO) [106, 6, 9, 12, 49, 107]. In contrast to the classical spin ice physics of

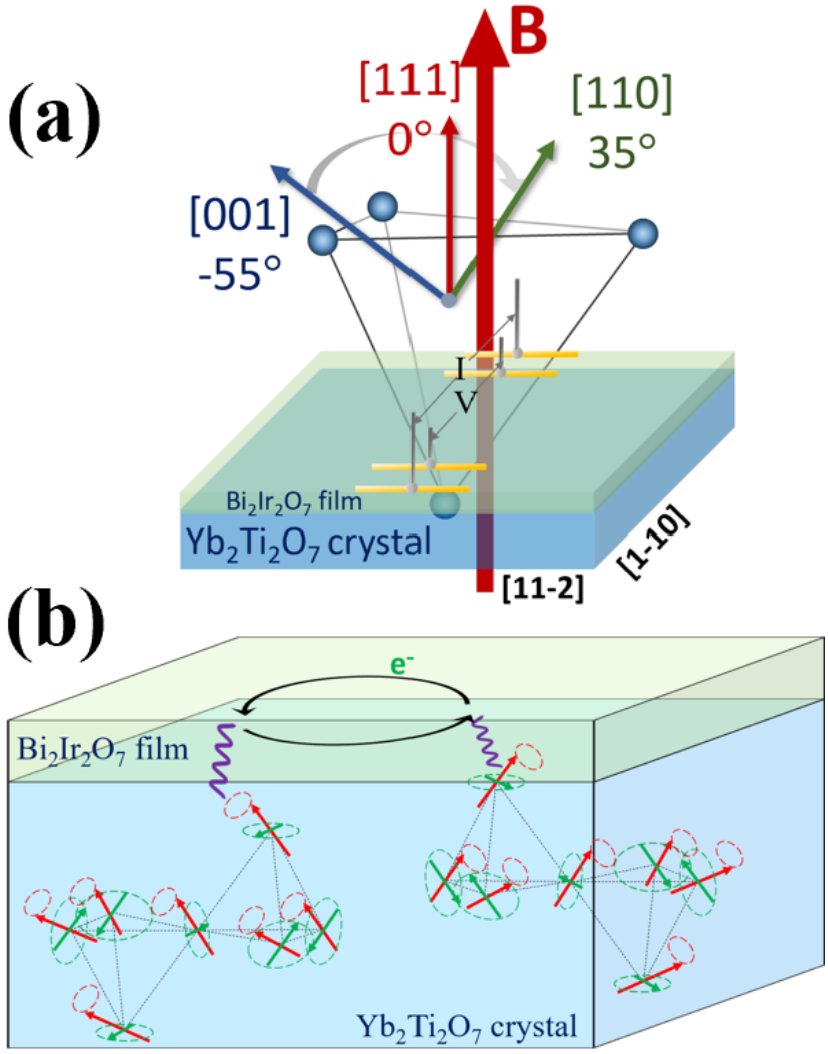


**Figure 4.1:** (a) Schematic diagram of the interface of BIO/YbTO heterostructure and the measurement configuration. (b) Schematic diagram of the scattering process on the interface of BIO/YbTO heterostructure. The tetrahedra illustrate the coexistence of FM (red arrows with freedom to rotate around the local [001] axis) and AFM (green arrows with freedom to totate in the local (111) plane) phase of YbTO crystal structure.

DTO, we find that the interfacial impact on the electronic transport of the BIO thin film is drastically enhanced by YbTO due to the QSF of YbTO, which is highlighted by an anomalous scaling of the BIO resistivity with temperature and magnetic field that reflects the unconventional spin-wave dynamics of YbTO. Our findings provide compelling evidence for a distinct avenue to access and explore quantum magnetism through proximitized electric transport. The realization of transport control of itinerant electrons through localized quantum spin degrees of freedom in the insulator could enable potential applications in spintronic devices.

## 4.2 Results

### 4.2.1 Synthesis

To couple the QSF of localized spins with charge carriers, we devised and synthesized the epitaxial heterostructure of $Bi_2Ir_2O_7/Yb_2Ti_2O_7$ (BIO/YbTO) [Fig. 4.1] by depositing a nominally 4 nm-thick BIO thin film onto a (111)-oriented stoichiometric YbTO single crystal substrate. BIO is an ideal carrier provider since it is a nonmagnetic metal with a pyrochlore structure [108] compatible with YbTO. Since the properties of YbTO is believed to be sensitive to disorder, we prepared stoichiometric YbTO single crystal with a modified traveling-solvent floating zone method as recently reported [22]. The lattice parameter of our stoichiometric YbTO single crystal is 10.03377(5) Å [Fig. 4.2(b)], consistent with the previous report [22]. The epitaxy of the heterostructure was confirmed by cross-section transmission electron microscope (TEM) [Fig. 4.3(b)] with energy dispersive spectroscopy [Fig. 4.4]. X-ray diffraction [Fig. 4.3(c)] also confirmed the single-phase epitaxial growth. The actual thickness of the BIO film to be discussed below was measured to be 3.9 nm [Fig. 4.3(e)] by X-ray reflectivity.

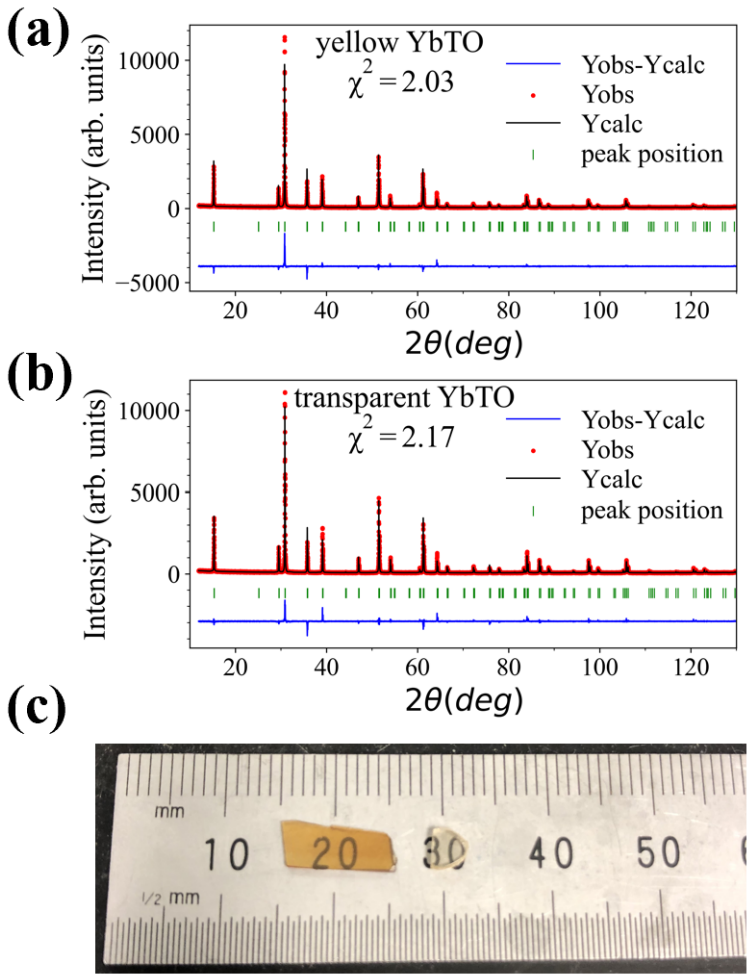


**Figure 4.2:** Powder X-ray diffraction patterns for YbTO-ns and YbTO. (a) The refined lattice parameter is 10.04150(6) Å for YbTO-ns. (b) The refined lattice parameter is 10.03377(5) Å for YbTO. (c) Yellow YbTO-ns (left) and transparent colorless YbTO (right).

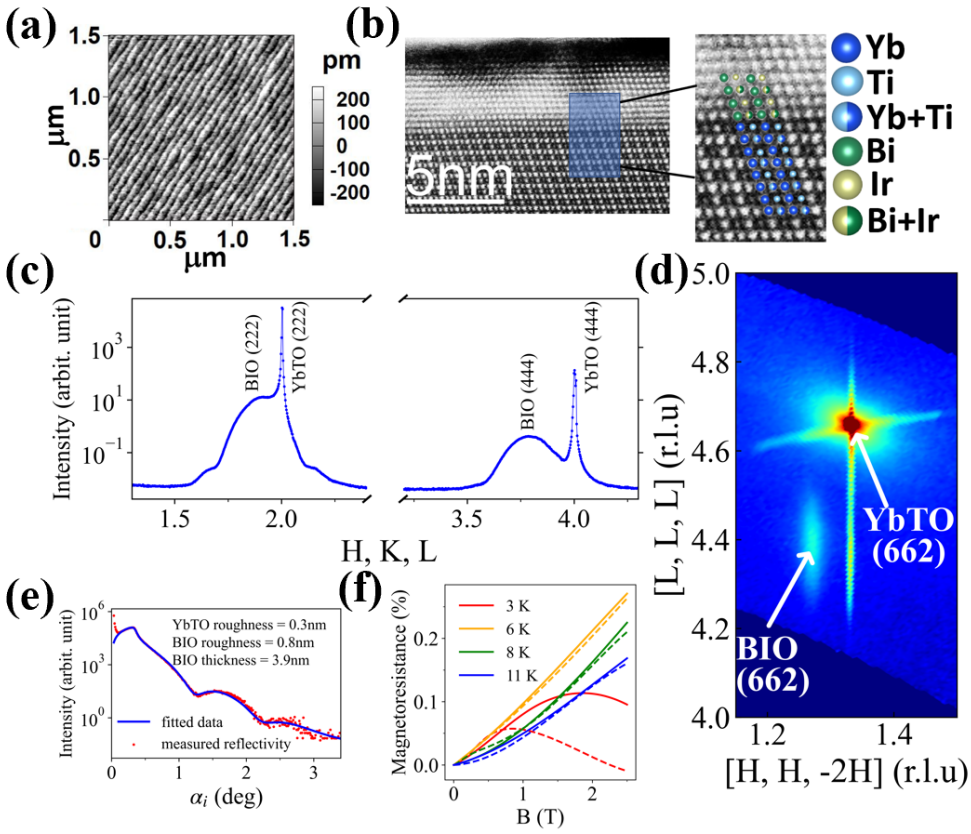


**Figure 4.3:** All data were taken for heterostructure with 3.9 nm BIO film deposited on YbTO, which is the one discussed in the main text. (a) A representative atomic-force-microscope image of the YbTO substrate surface after cutting the YbTO crystal into (111)-oriented substrates and carefully polishing them to atomic flatness. The root mean square surface roughness is ∼0.92 Å. (b) Atomic resolution high-angle-annular-dark field-STEM image of the interface. The TEM lamella surface normal is [1-10], which shows a sharp epitaxial interface. A magnified image is shown to indicate the cations on both sides of the interface. (c) Specular X-ray diffraction scan of the (222) and (444) structural peaks showing only the substrate peaks and the corresponding film peaks. (d) Reciprocal Space Mapping (RSM) near the YbTO (662) reflection, showing the relaxation strain state of the BIO film. (e) Representative X-ray reflectivity (XRR) data. (f) Magnetoresistance (MR) above 3 K. For the dashed line, the field is applied along out-of-plane [111] axis. For the solid line, the field is applied along [001] axis. It is almost isotropic between B // [111] and B // [001] without any extra features.

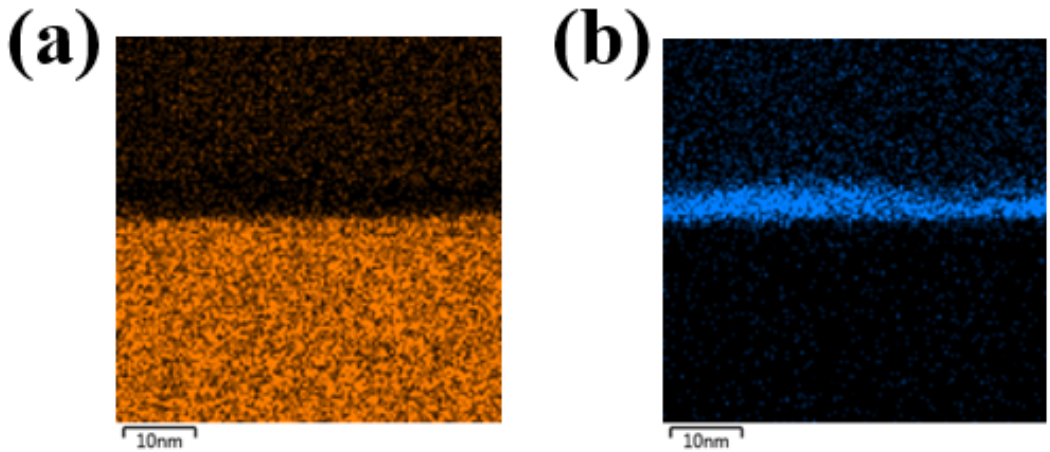


**Figure 4.4:** Energy Dispersive Spectroscopy (EDS) images of heterostructure BIO/YbTO. The EDS results demonstrate that there is no significant interdiffusion across the interface. (a): Yb EDS images. (b): Bi EDS images.

### 4.2.2 Proximitized transport due to FM-AFM competition

The influence of YbTO magnetism becomes evident when comparing the resistivity of the BIO/YbTO heterostructure with a reference sample where the BIO film was grown on a nonmagnetic $Y_2Ti_2O_7$ (YTO) single crystal substrate [Fig. 4.5(a)]. In the high-temperature regime, both samples exhibit a similar trend as a function of temperature. The resistivity increases slowly with decreasing temperature [29] due to weak localization and/or disorder-enhanced electron-electron interaction in two-dimensions [108], especially at such reduce thickness. Nonetheless, the resistivity curves above 2 K can be mapped to each other by a scaling factor between BIO/YbTO and BIO/YTO heterostructures. However, in the sub-Kelvin regime, thermal fluctuations are suppressed, the impact of quantum magnetism takes over, and notable distinctions arise. Specifically, the resistivity of BIO/YbTO experiences a sharp increase at low temperatures, following a $1/T$ scaling [Fig. 4.5(b)], i.e., $\rho \propto 1/T$. Remarkably, this scaling behavior persists even below the FM transition temperature $T_c$ of YbTO ($\sim$ 224 mK [Fig. 4.6(a)]). In contrast, the resistivity of BIO/YTO remains varying gradually, and the $1/T$ scaling is clearly absent. Similarly, the $1/T$ scaling was not observed in the BIO/DTO heterostructure [see Fig. 4.7].

We find this scaling behavior highly unusual. In the simplest Drude picture, the resistivity is inversely proportional to an effective relaxation time $\tau$. If the proximity effect arises from scattering processes due to the exchange interactions between the spins of the charge carriers and the localized spins in the magnetic insulator like YbTO, the resultant electron relaxation time will have a temperature dependence governed by the spin fluctuations in the magnetic insulator [109]:

$$\frac{1}{\tau(T)} \propto \int \mathrm{d}\omega \int \mathrm{d}^2\mathbf{q}\, \mathcal{S}(\mathbf{q},\omega,T)\Phi(\mathbf{q}), \tag{4.1}$$

where $\mathcal{S}(\mathbf{q},\omega,T)$ is the dynamical spin correlation functions in YbTO, and $\Phi(\mathbf{q})$ is a form factor that accounts for the phase space of scattering determined by the Fermi surface structure of BIO. In the temperature range of interests, one can

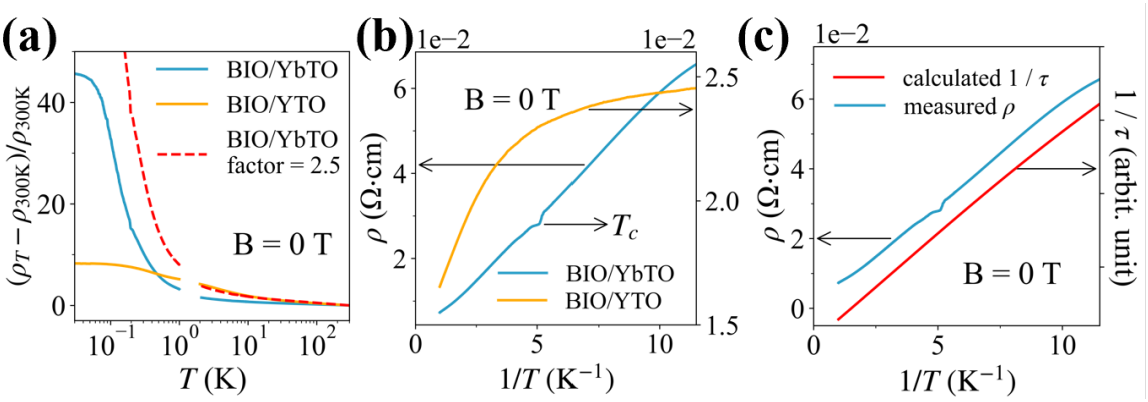


**Figure 4.5:** (a) Temperature dependence of the normalized resistivity for the BIO/YbTO (blue) and BIO/YTO (orange) heterostrutures from 300 K to 87 mK at zero magnetic field. The temperature gap between 1 to 2 K is due to the fact that two instruments were used to measure the high and low temperature resistivity, respectively. The red dashed line is obtained by multiplying the blue line with a factor of 2.5 to illustrate the similar temperature dependence of the two samples at high temperatures and their drastic difference at low temperature. In other words, it is possible to scale the two samples at high temperature region but not the low temperature region. (b) The zero-field resistivity plotted as a function of $1/T$ in the low temperature region. While the BIO/YbTO curve shows a linear behavior down to about 100 mK, the BIO/YTO curve is clearly sub-linear. The kink position on BIO/YbTO curve corresponds to the FM transition temperature of YbTO at zero field. (c) The inverse effective relaxation time (red line) calculated from Eq. (4.1) shows a same $1/T$ dependence as the resistivity does.

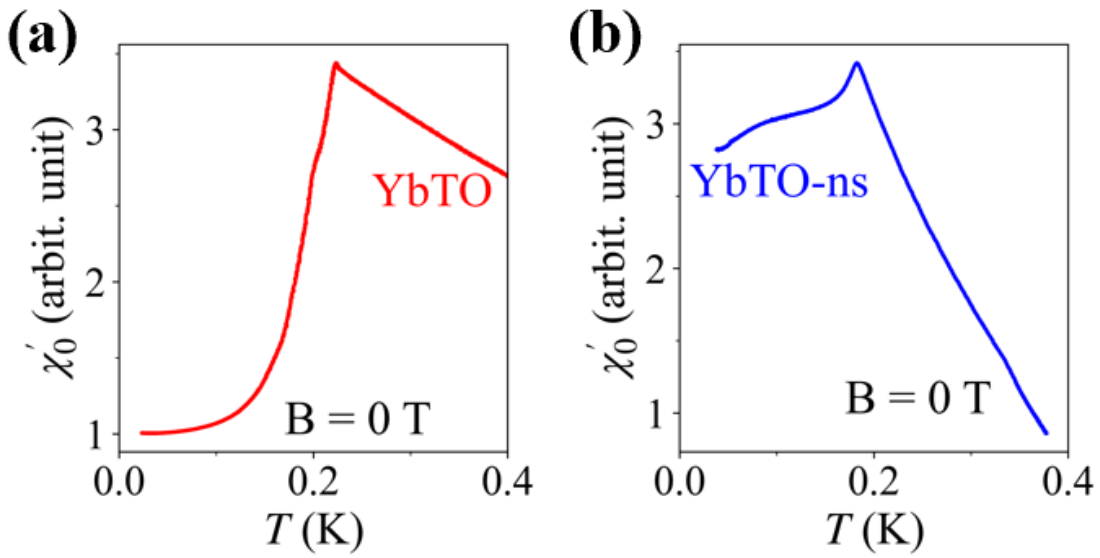


**Figure 4.6:** Temperature sweep of AC susceptibility at zero field for YbTO and YbTO-ns

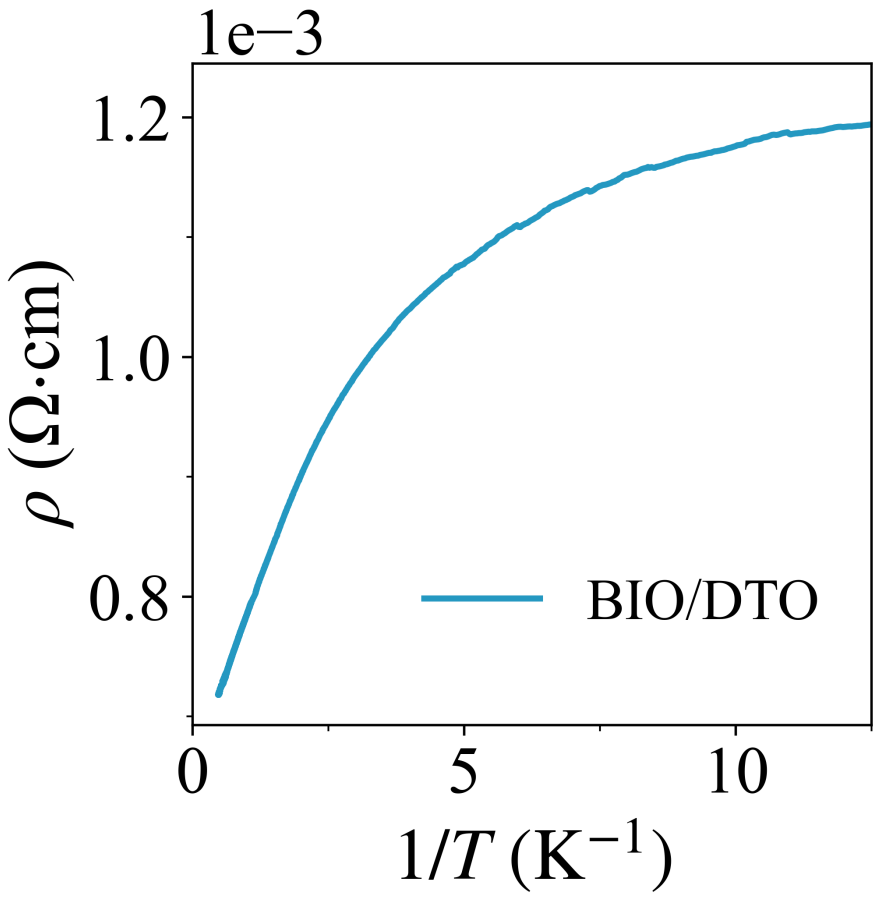


**Figure 4.7:** $T^{-1}$ dependence of the resistivity for BIO/DTO at zero field. This sample is the one used in reference [105].

assume that other scattering channels, such as electron-electron, electron-phonon, and impurity scatterings, have a much weaker temperature dependence. The observed $1/T$ scaling behavior then clearly contradicts what one would expect based a conventional spin-wave picture for an FM order, where the thermal occupation of bosonic spin waves increases as temperature increases and yields a shorter relaxation time, leading to a positive contribution to the resistivity. Instead, a previous theoretical study has shown that the $1/T$ behavior of itinerant frustrated magnets can be attributed to quantum fluctuations in a liquid-like spin state below the Curie-Weiss temperature [110].

To evaluate such a mechanism, we refer to the dynamical structure factor $\mathcal{S}(\mathbf{q}, \omega, T)$ reported by a recent inelastic neutron scattering experiment [25] on YbTO in the low-energy regime of tens of $\mu$eV. It was found that, due to proximity to a quantum critical point among the FM, AFM, and spin liquid phases [111], $\mathcal{S}(\mathbf{q}, \omega, T)$ exhibits a dynamical scaling behavior

$$k_B T \mathcal{S}(\mathbf{q}, \omega, T) \sim 2 \left( \frac{1}{\exp(x) - 1} + 1 \right) \frac{Bx}{R^2 + x^2}, \tag{4.2}$$

where $x = \hbar\omega / k_B T$ with fitted parameters $B = 0.0181$ and $R = 0.80$ [25]. By inserting this scaling form into Eq. (4.1), one can calculate the reversed relaxation time of the charge carriers due to the YbTO QSF. After performing the frequency integral up to a small cutoff at 4.3 $\mu$eV, we indeed arrived at a $1/T$-like behavior of the reversed relaxation time as shown in Fig. 4.5(c), resembling the $1/T$ behavior of the BIO resistivity. This behavior is robust against different cutoff values in a wide range, as demonstrated in Fig. 4.8 with the cutoff from 0.086 $\mu$eV to 8.6 $\mu$eV. The temperature dependence of the BIO resistivity therefore reflects the scaling behavior of the QSF in YbTO.

This proximitized transport behavior can be tuned by magnetic field. When applying a field along [001] to suppress the YbTO QSF at 30 mK, the BIO resistivity decreases rapidly below 1 T [Fig. 4.9(a)]. The decrease quickly slows down as the field

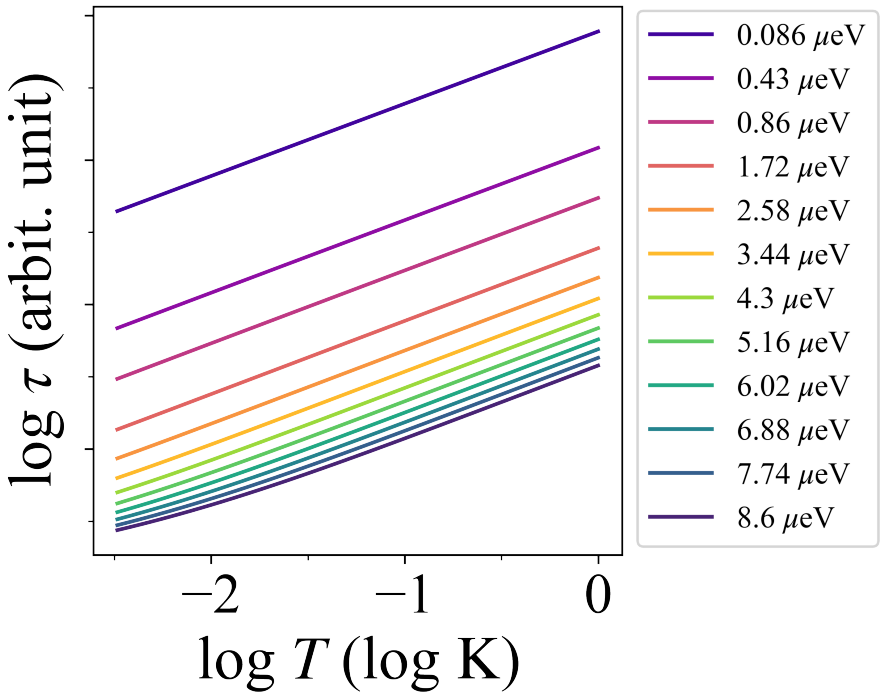


**Figure 4.8:** Logarithm of calculated relaxation time as a function of logarithm of temperature. This figure shows the results under different integral frequency cutoff from 0.086 $\mu$eV to 8.6 $\mu$eV energy cutoff in Eq. (2).

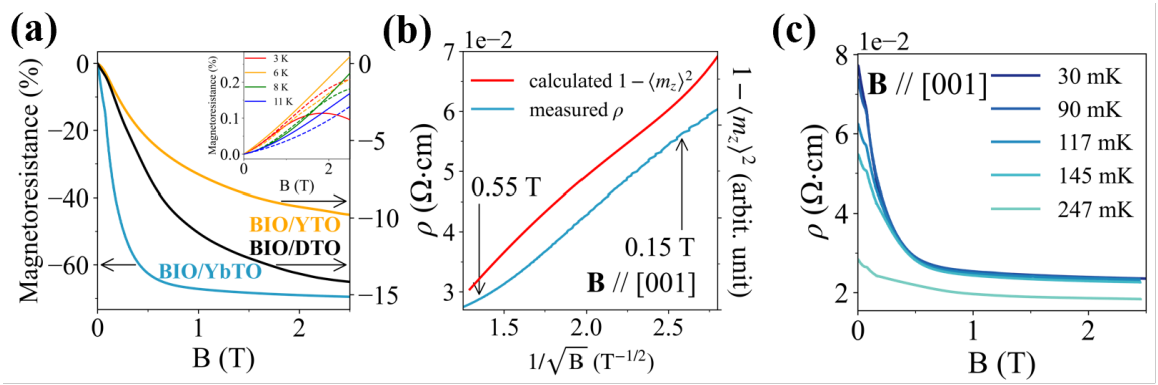


**Figure 4.9:** Field-dependent resistivity of BIO/YbTO. (a) MR of BIO/YbTO, BIO/DTO and BIO/YTO at 30 mK with B // [001]. Inset: MR of BIO/YbTO (solid lines) and BIO/YTO (dashed lines) above 3 K with B // [001]. (b) Blue line: The resistivity of BIO/YbTO at 30 mK with B // [001] plotted against $1/\sqrt{B}$ for the low field region where the MR shows the strongest negative drop. Red line: The calculated $1-\langle m_z\rangle^2$ that represents the amplitude of the transverse spin fluctuations shows a similar $1/\sqrt{B}$ dependence as the resistivity does. (c) Field dependence of the resistivity of BIO/YbTO with B // [001] at four temperatures below $T_c$ of YbTO and one slightly above.

approaches 1 T, resulting in a nearly flat magnetoresistance (MR) curve beyond that point. This rapid recovery of the conductivity can be understood from the fact that the AFM fluctuations are strongly suppressed by the external magnetic field through enforcing the FM order [24]. In fact, the broad spin waves of YbTO have been shown to disappear quickly under magnetic field by inelastic neutron scattering [24]. This sharp negative MR by tens of percents at small fields is also in remarkable contrast with the gradual and slow decrease observed in the BIO/YTO reference sample across the entire measured field range. This distinction disappears at elevated temperatures above 3 K, when thermal fluctuations dominate over quantum fluctuations, and the MR of BIO/YTO and BIO/YbTO becomes virtually the same as seen in the inset of [Fig. 4.9(a)]. One can make a similar comparison with the reported BIO/DTO heterostructure[105]. They both have a positive sign and a similar amplitude around 0.2% at high temperatures. Such a similarity again points to the dominant role of the thermal fluctuations in the BIO transport properties at high temperatures. Their difference emerges at low temperatures where thermal fluctuations are suppressed. At 30 mK, other than a relatively small anomaly ($\sim$ 1%) when the field induces the ice rule-breaking transition of classical spin ice in DTO, the MR of BIO/DTO is overall very similar to BIO/YTO and thus distinct from the large sharp negative MR observed here for BIO/YbTO [Fig. 4.9(a)]. This comparison highlights the drastically enhanced impact of quantum spins on the proximitized transport.

Quantitatively, we find a $1/\sqrt{\mathrm{B}}$ scaling for the sharp resistivity drop [Fig. 4.9(b)] through logarithmic fitting of the MR at 30 mK, which is also absent in BIO/YTO [Fig. 4.10(a)]. Again, such an algebraic scaling cannot be explained by conventional spin waves, as the Bose-Einstein distribution would result in exponentially suppression of spin fluctuations due to the low temperature (30 mK) and the field-induced gap [112]. Instead, we resort to a simple model that has been used to capture the magnetic-field dependence of the spin fluctuations of YbTO at the mean-field level [104]. Specifically, taking a coarse-grained magnetization parameterized by a unit vector $\mathbf{m}$ leads to the following potential energy that describes the competition between the

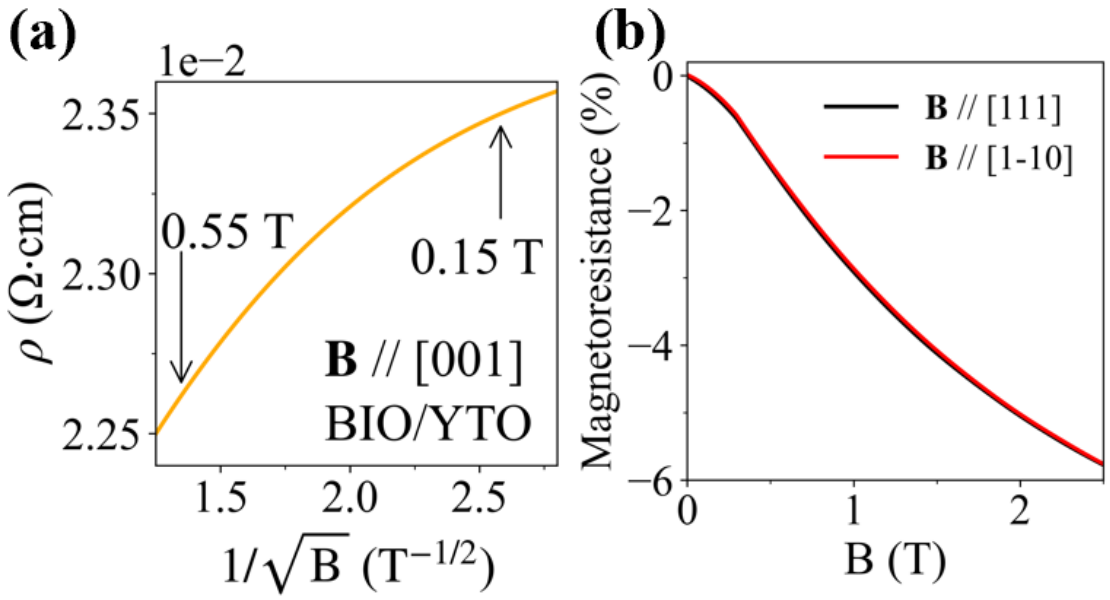


**Figure 4.10:** (a) $B^{-\frac{1}{2}}$ dependence of the resistivity of BIO/YTO at 30 mK with magnetic fields applied along [001] axis. (b) MR of BIO/YTO at 30 mK with magnetic fields applied along [111] and [1-10] separately.

Zeeman energy and the magnetic anisotropy [104]:

$$U = -\mathbf{B}\cdot\mathbf{m} - K_1\sum_i(\mathbf{m}\cdot\mathbf{e}_i)^4 - K_2\prod_i(\mathbf{m}\cdot\mathbf{e}_i)^2. \tag{4.3}$$

The form of the anisotropy respects the cubic symmetry of YbTO, and the parameters $K_1 = 0.14$ and $K_2 = -0.55$ have been used to match the magnetic-field induced phase transitions and the corresponding critical field strengths [104]. For a magnetic field applied along the $z$ direction (i.e., [001]), the thermal average $1 - \langle m_z\rangle^2$ measures the magnitude of the allowed transverse fluctuations. One can see in Fig. 4.9(b) that it increases with decreasing field and roughly reproduces the $1/\sqrt{\mathrm{B}}$ scaling observed in MR. The effective cubic anisotropy here can be viewed as a coarse-grained result of interactions between the four spins on a single Yb tetrahedron, suggesting that short-range correlations largely contribute to the fluctuations and the proximitized MR.

The combined temperature-magnetic field control on the proximitized transport is presented in Fig. 4.9(c), where the unnormalized MR curves at different temperatures all flatten above 1 T and clearly converge to a similar level. In other words, the strong temperature dependence of the resistivity only occurs around zero field, and the temperature dependence becomes minimal once the external magnetic field effectively suppresses spin fluctuations. As a result, the negative MR at small fields is most pronounced at lower temperatures, while thermal fluctuations reduce its sensitivity. These findings provide compelling evidence that the BIO resistivity offers an effective means of assessing the magnitudes of YbTO QSF.

### 4.2.3 Proximitized transport due to field-induced transition

The proximitized transport strongly responds to the field-induced transitions of YbTO as well. Note that both BIO film and crystal show the linear isotropic MR above 2 K [108]. Significant anisotropy arises here for BIO/YbTO. With B // [110] and B // [111] [Fig. 4.11(a)], the MR initially shows a sharp negative response similar to B //

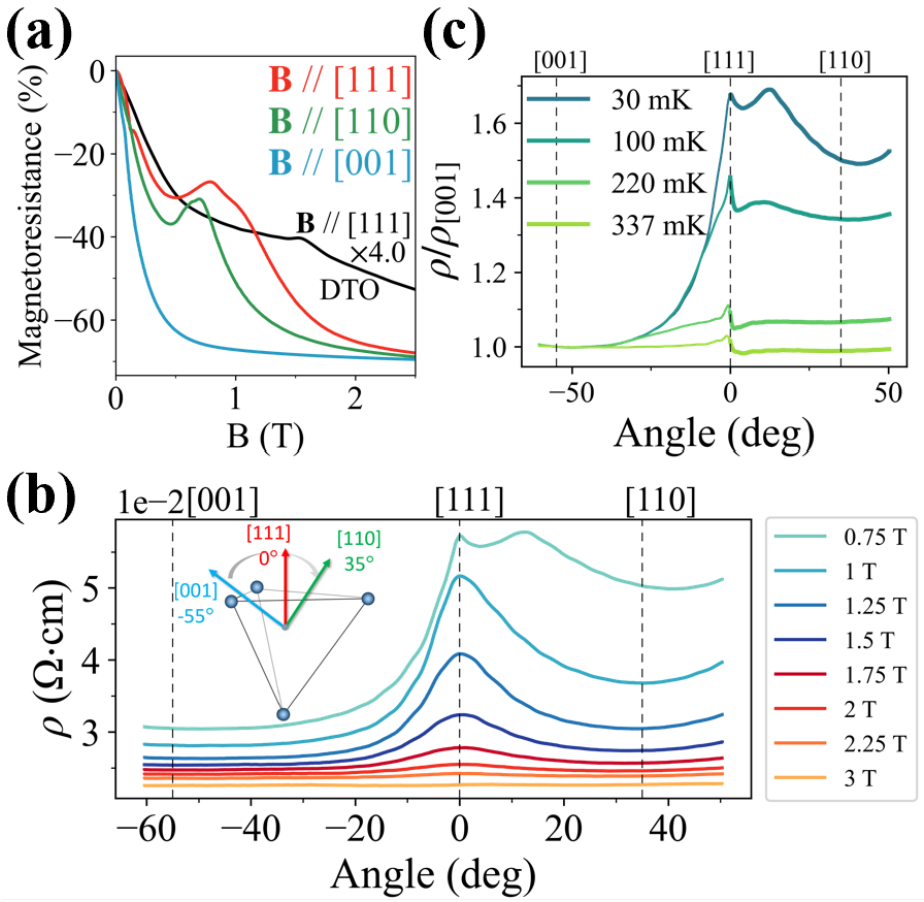


**Figure 4.11:** Angle-dependent MR of BIO/YbTO. (a) MR at 30 mK with magnetic field applied along three high-symmetric directions. Black line is MR of BIO/DTO at 30 mK with magnetic field applied along [111] axis. This black line is multiplied with a factor of 4 for better visualization. (b) Field angular scans of the resistivity at 30 mK under seven different field strengths above the critical field of B // [111] and one field strength slightly below. Insert: The measurement configuration. The applied field is vertical and the current is along [1-10]. (c) Field angular scans of the resistivity at 0.75 T at three temperatures below $T_c$ and one above. For the purpose of comparison, the scans are normalized by the resistivity with B // [001] at each temperature.

[001]. However, the rate of decrease slows down followed by an upturn. As the field continues to increase, the MR becomes negative again, resulting in a broad peak-like feature. These anisotropic behaviors are absent in the BIO/YTO reference sample [Fig. 4.10(b)], indicating that they originate from the YbTO quantum magnetism. The locations of the peak-like feature around 0.7 T and 0.79 T for B // [110] and B // [111], respectively, well align with the critical fields of the YbTO phase transition [26, 104] driven by the competition between the cubic magnetic anisotropy and the Zeeman energy [14] described above by Eq. (4.3). Specifically, since <001> is the easy axis of the canted FM order, a [111] field is an effective transverse field that enforces a polarized state by mixing the three spontaneous <001> configurations, causing enhanced fluctuations which are now captured by the BIO resistivity. For comparison, this peak-like feature is much more pronounced than the MR anomaly due to the classical spin-ice transition in the BIO/DTO heterostructure [105], showcasing again the much stronger impacts of quantum spin systems than classical spin systems on proximitized transport.

The pronounced peak-like feature must be driven by is the YbTO QSFs rather than its stray field. The stray field near the boundary of a magnetic material is proportional to the magnetization. The magnetization of DTO along <111> (both the Kagome ice state and the 3-in-1-out state) is much larger than the magnetization of YbTO of all directions [104, 5]. Therefore, if the stray field dictates the size of the anomaly or any feature in MR, one would expect it to be much more significant in BIO/DTO than BIO/YbTO. Moreover, if an MR feature is driven by the stray field, it should resemble the shape of the M(B) curve, which means the BIO/DTO anomaly would have a step-like shape because of the sharp magnetization jump. Meanwhile, the M(B) curve of YbTO has no jump but just changes slope via a kink at the critical field. This expectation based on stray field is clearly inconsistent with the experimental observations of the MR measurements.

At field above 2 T, both MR curves with B // [110] and B // [111] become flatten deep into the field-polarized state where the fluctuations are completely suppressed.

They also converge to the same level as B // [001]. Such weak dependence on the field direction at high fields shows that the orientation of the magnetization of YbTO has little impact on charge transport in BIO despite the magnetic anisotropy, which can be explained by the fact that the field-polarized state can be described as a classical order parameter. This observation was further confirmed by angular scans that continuously rotate the field from [001] to [111], and to [110]. As seen in [Fig. 4.11(b)], the resistivity displayed almost no angle dependence at 3 T. Only when the field decreases toward the critical field, the angle dependence becomes dramatically stronger, with the resistivity showing a rapid increase near [111] where the fluctuations are the strongest. The resistance changed smoothly with the field angle without any kink, indicating that the field is continuously tuning the strength of spin fluctuations.

What is also particularly interesting is that when the field dropped below the critical field of [111], as shown at 0.75 T, a sharp dip in the angular change around [111] was observed, leading to a double-peak-like shape. This behavior can be attributed to the domain conversion of the spontaneous canted FM order since [111] is the hard axis and thus the tipping point of domain re-population [26]. The dip likely marks the narrow angular range of domain coexistence. More importantly, as seen in Fig. 4.11(c), this dip persists at temperatures above $T_c$, capturing the famous reentrant behavior of the FM state in the [111] field-temperature phase diagram [26] that is a signature of the strong QSF in YbTO. All the transport behaviors discussed above are well reproducible in different samples [Fig. 4.12].

### 4.2.4 Impacts of YbTO nonstoichiometry

Given the remarkable sensitivity of the proximitized transport to the YbTO quantum magnetism, we performed the same measurements on a BIO film grown on a nonstoichiometric YbTO (YbTO-ns) substrate (See Fig. 4.2) to investigate the impact of site disorder between the $Yb^{3+}$ and $Ti^{4+}$ ions. This disorder is known to effectively suppress the spontaneous FM order and further broaden the spin wave

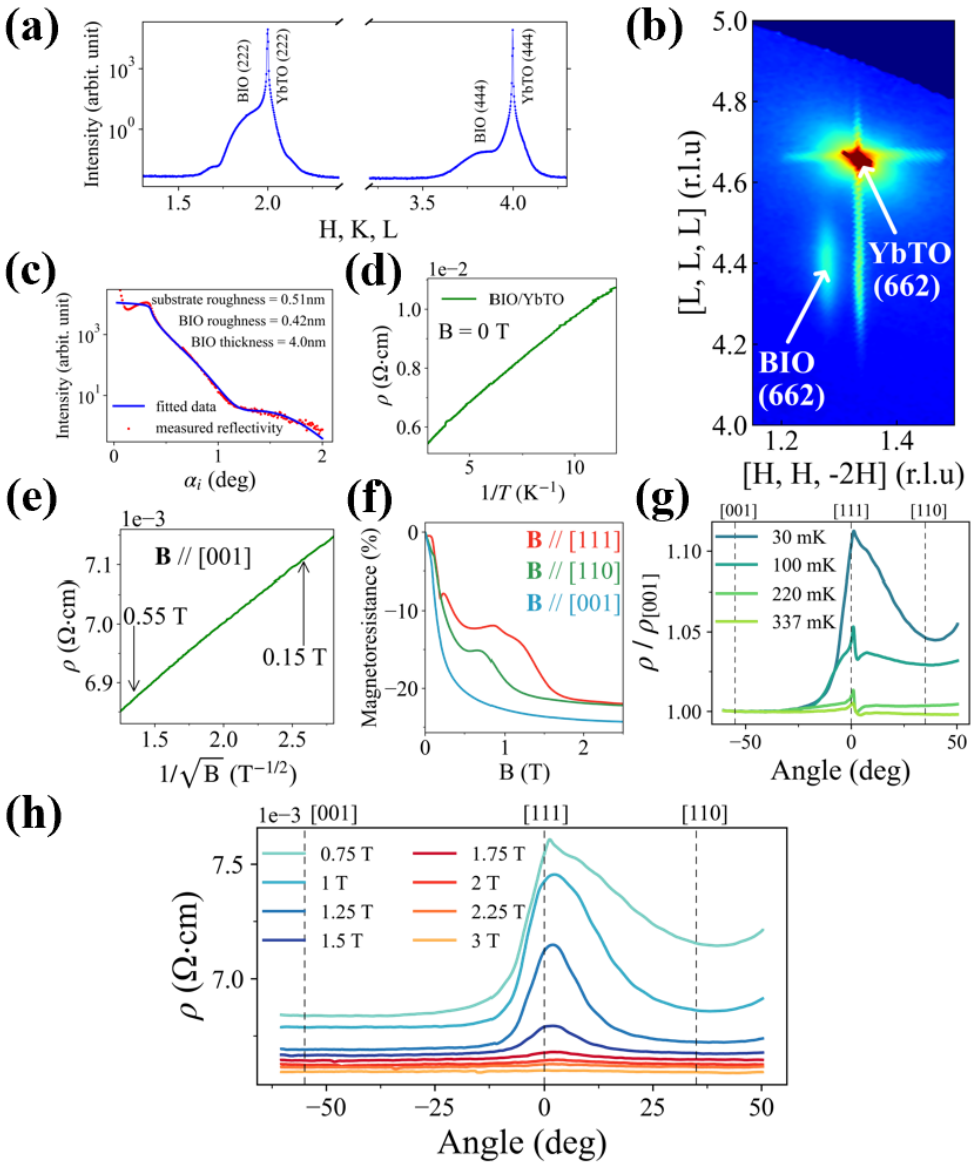


**Figure 4.12:** All data were taken for heterostructure with 4.0 nm BIO film deposited on YbTO, which is the one to show the reproducibility. (a) X-ray diffraction pattern collected on the surface of BIO/YbTO heterostructrue of (222) and (444) structural peaks. (b) RSM near the YbTO (662) reflection, showing the relaxation strain state of the BIO film. (c) Representative XRR data. (d) $T^{-1}$ dependence of the resistivity for BIO/YbTO at zero field. (e) $B^{-\frac{1}{2}}$ dependence of the resistivity of BIO/YbTO at 30 mK with magnetic field applied along [001] axis. (f) MR at 30 mK with magnetic field applied along three high-symmetric directions. (g) Angle dependence of the normalized resistivity at several temperatures with 0.75 T magnetic field. (h) Angle dependence of the resistivity at 30 mK with several selected fields above 0.75 T.

spectra [22, 24]. Fig. 4.13(a-c) shows that the MR is overall similar to that in the stoichiometric case, including the sharp negative MR, the $1/\sqrt{B}$ dependence, and the response to the field-induced transition. These results are consistent with the resistive contribution from short-range fluctuations. Notably, the unnormalized MR with B // [001] reveals an enhanced resistivity at zero-field and low temperatures, indicating the presence of significant QSF despite the disorder. However, a sub-linear deviation from the $1/T$ scaling can be observed in Fig. 4.13(d), suggesting that the temperature dependence of the resistivity is more sensitive to the spatial coherence in the spin fluctuations, which may arise from either the inhomogeneity of the exchange interactions or an overall deviation from the quantum critical regime. In fact, the dynamical scaling behavior of YbTO described by Eq. (4.2) was observed in stoichiometric YbTO crystals [25].

## 4.3 Discussion

It has been a long-standing puzzle at what levels coherent quantum fluctuations play a role in materials close to realizing exotic quantum spin liquids. In certain candidate systems, the extremely broad excitation spectrum may be understood as spin waves from magnetically disordered ground states [113], and spin fluctuations mainly consist of thermal occupation of spin-wave modes. Recent inspirations are offered along the lines of witnessing quantum entanglement through magnetic spectrum [114], anomalous thermal transport experiments [115], and magnetic noise characterization [116], etc. Proximitized electric transport study of QSF demonstrated in this work offers several advantages, such as a higher temperature resolution and an enhanced sensitivity to low-energy fluctuations with large-momentum transfer, where scattering processes are particularly efficient in reducing the electron relaxation time.

It is remarkable to see that the thin film resistivity of our heterostructure construction well captures the essential properties of the bulk quantum magnetism, despite the potential complications from the interface. The same transition temperature and

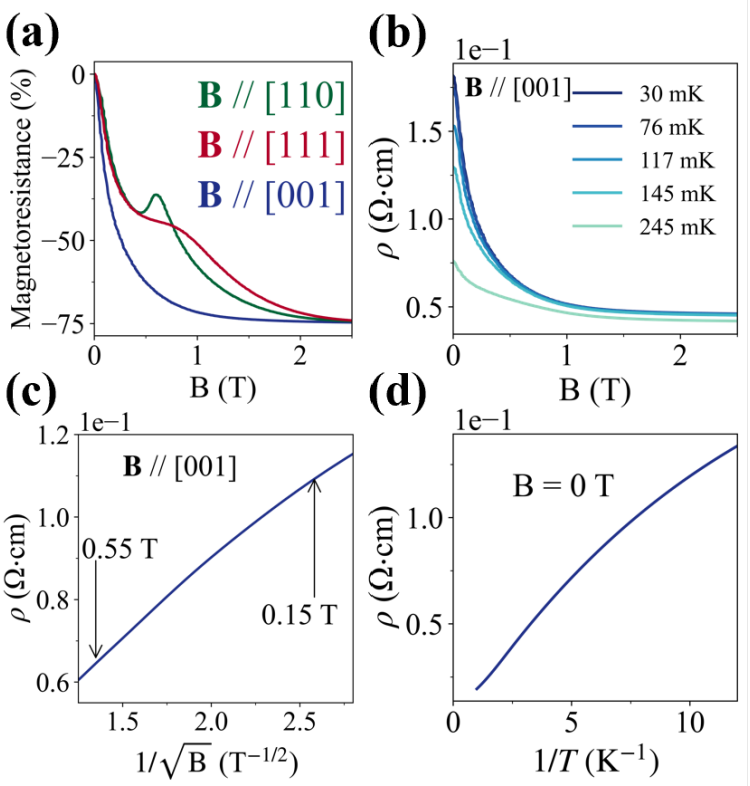


**Figure 4.13:** Resistivity behavior of a 4.2 nm thick BIO film on YbTO-ns. (a) MR at 30 mK with magnetic field applied along three high-symmetric directions shows the initial sharp negative drop. It flattens with increasing field when B // [001], whereas the additional features appear at the critical fields for B // [110] and B // [111]. (b) Field dependence of the resistivity with B // [001] at five temperatures similar to BIO/YbTO shown in Fig. 4.9(c). (c) $1/\sqrt{\mathrm{B}}$ dependence of the resistivity at 30 mK with B // [001]. (d) $1/T$ dependence of the resistivity at zero field. Compared with BIO/YbTO [Fig. 4.5(b)], a sublinear deviation can be seen.

critical field between proximitized transport and susceptibility indicate the Yb-Yb interface magnetism is at least qualitatively the same as the bulk. Note that all the matrix elements of the Yb-Yb exchange matrix are finite for bulk YbTO [14], and they account for all symmetry components of the exchange interaction, i.e., XY-like ($J_1$), Ising-like ($J_2$), pseudodipolar ($J_3$), and DM ($J_4$) interactions. Any quantitative difference at the interface could be accounted for by modifications of these parameters. The experimental facts discussed above indicate that such changes at the interface (if any) make no significant difference, at least from the prospect of the proximitized transport.

In summary, our investigation on the electric transport properties of a BIO film deposited on a YbTO single crystal shows a large enhancement in resistance due to the proximity to quantum magnetism at low temperatures. The observed scaling behaviors of the resistance with temperature and magnetic field strongly point to the mechanism of QSF-mediated scattering of electrons at the interface. Moreover, the distinct responses under different field directions highlights how the MR of BIO accurately captures the magnetic anisotropy of the field-induced quantum phase transitions in YbTO. Overall, our study establishes a novel approach to realize strong correlation between the electronic transport and the QSF by employing a heterostructure comprising a metallic film epitaxially grown on a quantum magnet, which provides guidelines for future exploration of proximitized transport phenomena derived from insulting quantum magnets. Furthermore, the thermal and magnetic controls of the proximitized transport hold promise for potential applications in spintronics by leveraging the unique properties of quantum magnetism.

# Chapter 5

# Spin ice states in $Dy_2Ti_2O_7$ thin film revealed by magnetic torque and proximitized transport

## 5.1 Introduction

Geometrical frustration is an important driving force for novel emergent magnetic states. One of the most important prototypes is the classical spin ice found in rare earth pyrochlores below the freezing temperature $T_s$, such as $Dy_2Ti_2O_7$ (DTO) and $Ho_2Ti_2O_7$ (HTO) [3, 117, 118, 6, 119, 120, 121]. It is a magnetic analog of water ice [8] and exhibits emergent magnetic monopole excitation [12, 122, 123, 50, 124, 125]. The basic building block is the tetrahedron of the Ising spins [4, 126] that point either in or out of the tetrahedron and must settle in one of the six degenerate 2-in-2-out (2:2) spin configurations as a result of the competition between their ferromagnetic dipolar interaction and antiferromagnetic superexchange interaction [106, 127, 128, 48]. The degeneracy rapidly grows as the 2:2 tetrahedra connect to each other according to the ice rule within the pyrochlore structure, giving rise to the non-zero residual entropy [9]. More interestingly, flipping a spin necessarily breaks the ice rule and effectively

creates a pair of magnetic monopole and antimonopole by turning two 2:2 tetrahedra into the 1-in-3-out and 3-in-1-out configurations, respectively [51, 5, 129]. When such spin flip is induced everywhere in the lattice by a magnetic field along a <111> axis, the monopole/antimonopole density increases drastically as they condensate into the magnetic charge-ordered state, i.e., the so-called saturated ice (3:1) state. This ice-rule-breaking transition is thus described as the liquid-gas transition of the magnetic monopoles with a critical end point $T_c$ in the field-temperature phase diagram. [130, 11, 131, 132].

While the rich spin ice physics has been extensively studied in the bulk crystals during the last three decades, epitaxial engineering is considered recently as a new route to tuning the spin ice behavior through, for instance, dimensional reduction [133] and/or strain effect [134]. However, experimental results on spin ice pyrochlore thin films have been limited, and the conclusions are far from clear [66, 135, 65, 136, 137, 74, 75, 138]. In particular, two studies showed that thick HTO films have similar magnetic anisotropy and magnetization to HTO crystal [135, 66], which was measured above 1.8 K and well above the temperatures of the spin ice behaviors [106, 130]. On the other hand, two other studies suggested that the Pauling entropy is released in DTO films based on heat capacity and a spin-ordered state may exist [65, 136], which could be attributed to strain effect according to Monte Carlo simulations [138]. But the exact magnetic structure is not yet clear. The limited studies highlight the general challenge in experimentally characterizing thin films of insulating frustrated magnets at ultralow temperatures due to the small sample volume and the presence of the substrate, both of which hinder the use of conventional bulk techniques, such as AC susceptibility and neutron scattering.

Here we demonstrate a measurement method that simultaneously probes proximitized electric transport and capacitive torque magnetometry (CTM) on a DTO thin film. The results unambiguously show the existence of the ice-rule breaking transition as functions of magnetic field and field angle. The behavior of the transition can be described by the well-established dipolar spin ice model but with a reduced effective

exchange interaction compared with the bulk. The temperature dependence also reveals a lower freezing temperature than the bulk. This experimental approach thus allows placing film samples on the same phase diagram as the bulk crystals, and is promising for thin film engineering of other frustrated magnets.

## 5.2 Results

We synthesized the epitaxial DTO thin film of ∼18 nm thickness on the (111)-oriented Yttria Stabilized Zirconia (YSZ) substrate, which is the most common and commercially available substrate for pyrochlore thin films. The DTO film was capped it by a $Bi_2Ir_2O_7$ (BIO) thin film of ∼3 nm thickness [Fig. 5.1(a)] to enable proximitized transport measurements. BIO is a non-magnetic pyrochlore metal [29, 28, 139]. Our recent work on epitaxial BIO thin films deposited on DTO single crystal substrates has demonstrated that the BIO resistivity is sensitive to the ice-rule-breaking transition of bulk DTO through a magnetoresistance (MR) anomaly which faithfully tracks the transition with field angle and temperature [105]. If the electric transport of the BIO layer here is sensitive to the transition in the DTO thin film as well, it will provide another efficient probe. Scanning transmission electron microscopy (STEM) images in Fig. 5.1(b) showed a highly epitaxial pyrochlore structure for both the DTO and BIO layers as well as sharp BIO/DTO and DTO/YSZ interfaces. No significant interdiffusion across the interface was found by energy dispersive X-ray spectroscopic (EDS) map [Fig. 5.2]. The epitaxial growth of both DTO and BIO layers was also confirmed by the specular scan of X-ray diffraction [Fig. 5.3(a)]. Reciprocal Space Mapping (RSM) [Fig. 5.3(b)] showed that the out-of-plane lattice spacing $d_{111}$ of the DTO film is 5.75 Å, which is roughly 1.7% smaller than bulk DTO, and the in-plane spacing $d_{11-2}$ is 4.19 Å, which is 1.4% larger than bulk DTO. The BIO reflection was not resolved within the measurement statistics likely due to the small thickness. From X-ray diffraction [Fig. 5.3(a)] the out-of-plane lattice spacing $d_{111}$ of the BIO

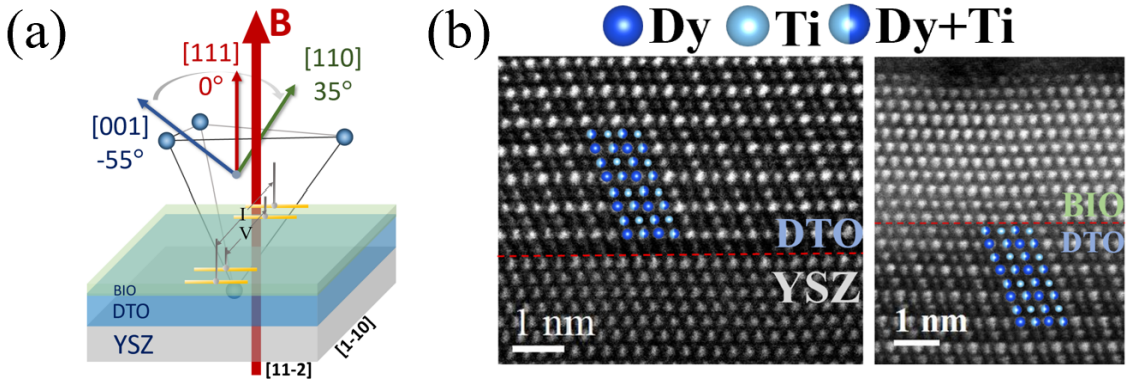


**Figure 5.1:** (a): Schematic diagram of the heterostructure BIO/DTO/YSZ and its measurement configuration. The current is along [1-10] axis, and the magnetic field is always perpendicular to the current. (b): Scanning transmission electron microscopy image with [1-10] being the lamella surface normal shows the sharp BIO/DTO/YSZ interface of the heterostructure.

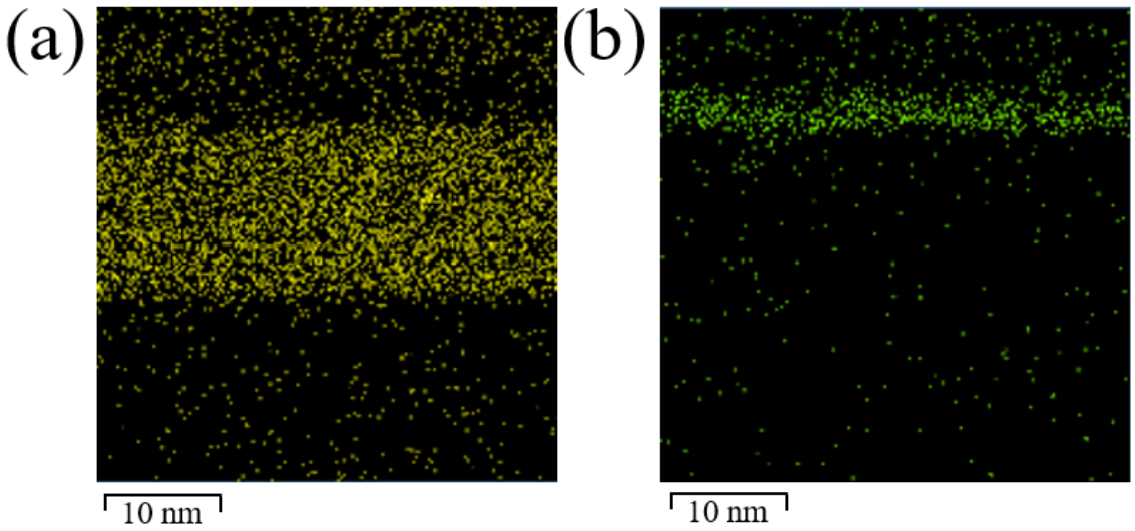


**Figure 5.2:** Energy dispersive spectroscopy images. (a) Dy EDS map; (b) Bi EDS map. The EDS results demonstrate that there is no significant interdiffusion across the interface. All data were taken for heterostructure with 2.7 nm BIO film deposited on 17.6 nm DTO film, which is on YSZ substrate.

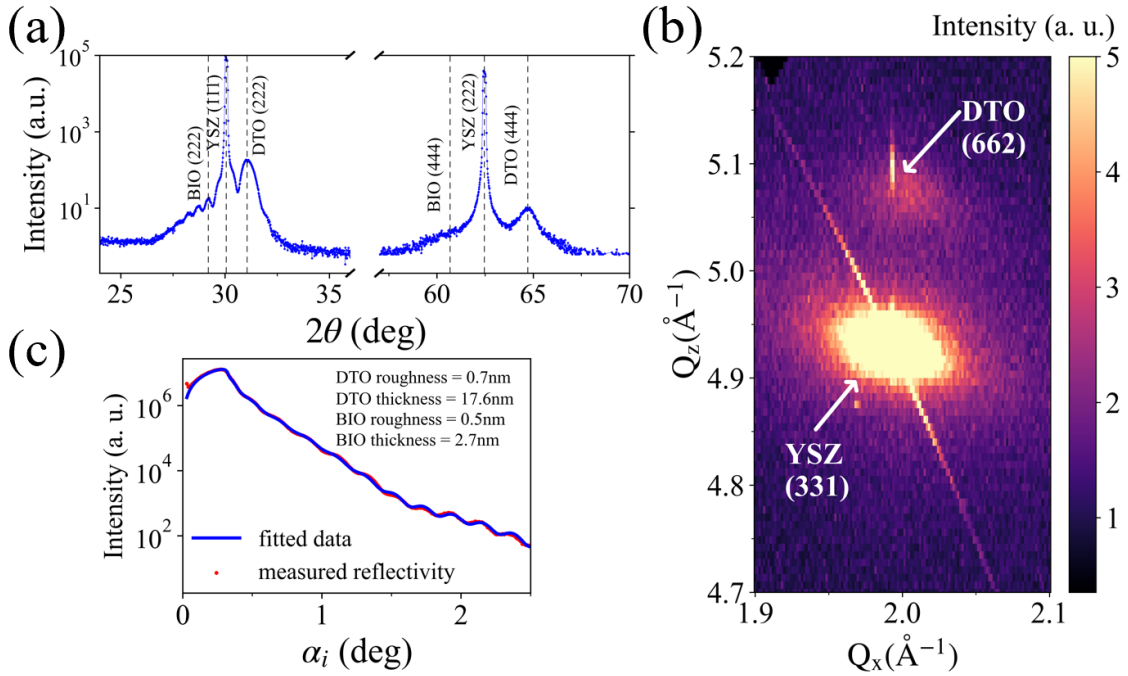


**Figure 5.3:** (a): An X-ray diffraction scan covering the (222) and (444) peaks of BIO/DTO/YSZ heterostructure. (b): Reciprocal Space Mapping (RSM) of DTO film near the YSZ (331) reflection. A weak diffuse background was observed on the right side of the (662) reflection, indicating that the DTO film is mostly strained with minor relaxation. (c): X-ray reflectivity scan (red dashed line) and corresponding fitted curve (blue solid line) of BIO/DTO/YSZ heterostructure. The specific sample used for obtaining the transport and CTM data has a 2.7 nm-thick BIO layer and a 17.6 nm-thick DTO layer extracted by fitting the X-ray reflectivity.

film is 6.10 Å, which is 2.5 % larger than bulk BIO. The thickness of the BIO layer and DTO layer is verified by X-ray reflectivity [Fig. 5.3(c)].

While the BIO resistivity is expected to probe the DTO layer by extra scattering of the electrons at the interface due to fluctuations of the Dy moments [105, 140], it is necessary to have another independent measure that probes the bulk of the DTO film. Capacitive torque magnetometry (CTM) is an effective tool for this purpose thanks to the high resolution of the cantilever deflection that measures magnetization vector via the torque signal [38]. Performing these two measurements simultaneously allows direct comparison of the magnetic signals of the same material from different origins. Fig. 5.4(a) shows the resistivity and the capacitance change at 0.03 K as a function of the magnetic field angle $\theta$ when a 10 T field was applied and rotated within the (1-10) plane from the [001], [111], [110], [11-1], and to [00-1] axis. The current was along [1-10] and thus always normal to the field. Note that 10 T is well above the critical field of the transition in DTO crystals when the field is along <111>. Rotating it away from <111> is expected to trigger the transition back to the (2:2) state at critical angles. As one can see, when the field deviates from [111] toward [110] or [001], the BIO resistivity exhibited sharp spikes at the same angles as the sharp jumps of the torque. The same behavior occurred when the field deviates from [11-1] toward [110] or [00-1]. The sharp jumps of the torque are known as turnovers of the magnetization vector when the ice-rule-breaking transition occurs by flipping the $\alpha$ or $\beta$ spin chain as observed for HTO crystal [61]. The overall angle dependence is in fact similar to HTO and characteristic of a spin-ice system. A minor difference is the asymmetry between the two critical angles on the two sides of [110] due to the demagnetization field effect of the film sample, which shifts the effective [110] principle axis of the magnetization away from the crystalline [110] axis toward [111]. Nonetheless, the result confirms that the torque signal is driven by the DTO film since neither BIO nor YSZ would display these features. The fact that the BIO resistivity also responds to the transition but with spikes instead of jumps confirms that the nature of the proximitized transport is not magnetization change but enhanced scattering from the

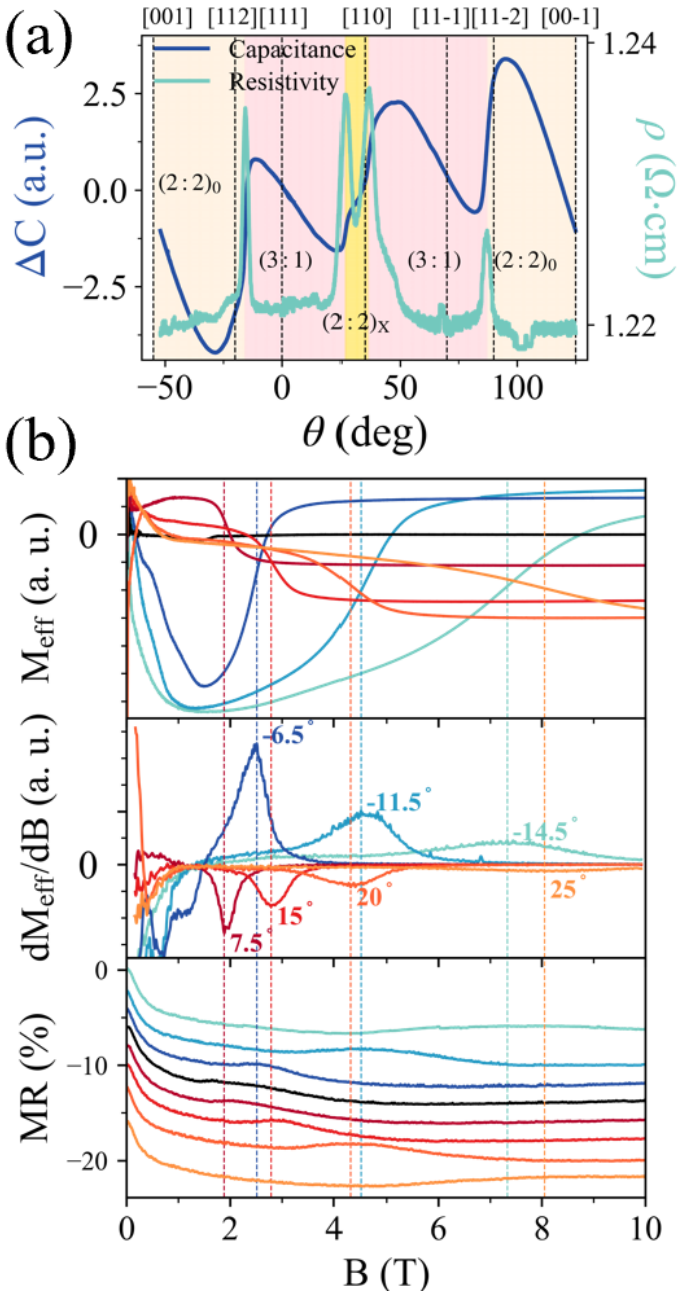


**Figure 5.4:** (a): The measured capacitance change C(B) − C(0 T) and resistivity as a function of angle in (1-10) plane with 10 T applied magnetic field at 0.03 K (blue line is capacitance change and green line is resistivity). (b): The field dependence results at 0.03 K with the magnetic field along different directions around [111] axis in the (1-10) plane. Positive angle is from [111] towards [110] axis and negative angle is from [111] towards [112] axis. Top panel: Effective magnetic moment vs. magnetic field. Middle panel: Derivative of effective magnetic moment vs. magnetic field. Bottom panel: Magnetoresistance (MR) vs. magnetic field.

unstable and fluctuating $\alpha$ or $\beta$ spin chain during the transition. The remarkable consistency of the critical angles between the two measurements also indicates no significant difference between the bulk of the DTO film and its interfacial region near BIO.

We further performed field scan measurements to determine the critical field as a function of $\theta$. Fig. 5.4(b) shows the results at 0.03 K with **B** along several directions around [111] in the (1-10) plane. We define the origin of $\theta$ as the [111] direction. The top panel shows the effective magnetic moment $M_{eff}$, which is obtained via dividing the capacitance change by external magnetic field: $(C(B) - C(0\ T))/B$. At high enough magnetic fields, $M_{eff}$ always reaches a flat plateau because for all these field angles the (3:1) state is reached [Fig. 5.1(a)] where the magnetization is saturated. The plateau has opposite signs for positive and negative angles because the torque is the cross-product of the magnetization vector and the field: $\tau = \mathbf{m} \times \mathbf{B}$, and the magnetization vector is along [111] in the (3:1) state. The plateau is thus reached by a drastic increase or decrease of $M_{eff}$, similar to the reported CTM data on HTO crystal [61]. This behavior is primarily due to the directional change of the magnetization vector during the ice-rule-breaking transition. Therefore, one can calculate the first-order derivative of this part of the $M_{eff}$ curve (central panel), and define the peak or dip as the critical field position $B_c$ [Fig. 5.4(b)]. Interestingly, an anomaly arises exactly at $B_c$ for all angles as well for the MR of the BIO layer (bottom panel). From both $dM_{eff}/dB$ and MR, one can see the same angular evolution of $B_c$: as **B** rotates away from [111] axis, $B_c$ increases and both the peak/dip and the anomaly broaden at the same time. This is due to the fact that the field projection along [111] is decreasing. As a result, a larger field is needed to induce the ice-rule-breaking transition, and the width of the transition is stretched. All the data clearly demonstrates that the ice-rule-breaking transition is preserved in the DTO thin film. Similar to the angle scan, the MR anomaly shows the proximitized transport reflects the fluctuations during the transition, whereas the torque probes the change of the magnetization.

It is known that the angular dependence of $B_c$ [60, 141] is directly related to the effective nearest-neighbor magnetic interaction $J_{eff} = J_{nn} + D_{nn}$, where $J_{nn}$ and $D_{nn}$ are the nearest-neighbor superexchange interaction and nearest-neighbor dipolar interaction of the "dipolar spin ice" model (DSIM) [128, 48]. Specifically, when **B** rotates around [111] in the (1-10) plane, $B_c$ follows an angular relation as [60]:

$$B_c = \begin{cases} \frac{0.6J_{eff}}{\cos\theta + 2\sqrt{2}\sin\theta} + B_{dem} & (\theta \leqslant 0) \\ \\ \frac{0.6J_{eff}}{\cos\theta - \sqrt{2}\sin\theta} + B_{dem} & (\theta \geqslant 0) \end{cases} \tag{5.1}$$

where $B_{dem}$ is the demagnetization field caused by the plate-shape of the (111)-oriented sample. As shown in Fig. 5.5, this relation well reproduces the angular dependence of $B_c$ of a DTO crystal observed in our previous work [105] with $J_{eff}$ = 1.01 K, which is consistent with the reported values [60]. However, $B_c$ of the DTO film clearly deviates from this relation. Simply adjusting $J_{eff}$ does not account for this inconsistency because the deviation is asymmetric between the positive and negative sides of $\theta$ whereas the impact of $J_{eff}$ on both sides is equivalent. This observation suggests a geometric modification within the tetrahedron. Note that a key condition of Eq. 5.1 is that the local axis of the Ising spin intersects the center of the tetrahedron, which can be defined as the origin (0,0,0) [Fig. 5.5]. This condition may not be true in thin film, e.g., due to distortion of the tetrahedron. If one assumes that the crossing point of all four Ising spin axes shifts away from (0,0,0) along [111] to $(\epsilon, \epsilon, \epsilon)$, e.g., due to compression of the tetrahedron, Eq. 5.1 must be modified as:

$$B_c = \begin{cases} \frac{0.6J_{eff}\sqrt{3\epsilon^2 - 2\epsilon + 3}/\sqrt{3}}{\cos\theta(1-3\epsilon) + 2\sqrt{2}\sin\theta} + B_{dem} & (\theta \leqslant 0) \\ \\ \frac{0.6J_{eff}\sqrt{3\epsilon^2 - 2\epsilon + 3}/\sqrt{3}}{\cos\theta(1-3\epsilon) - \sqrt{2}\sin\theta} + B_{dem} & (\theta \geqslant 0) \end{cases} \tag{5.2}$$

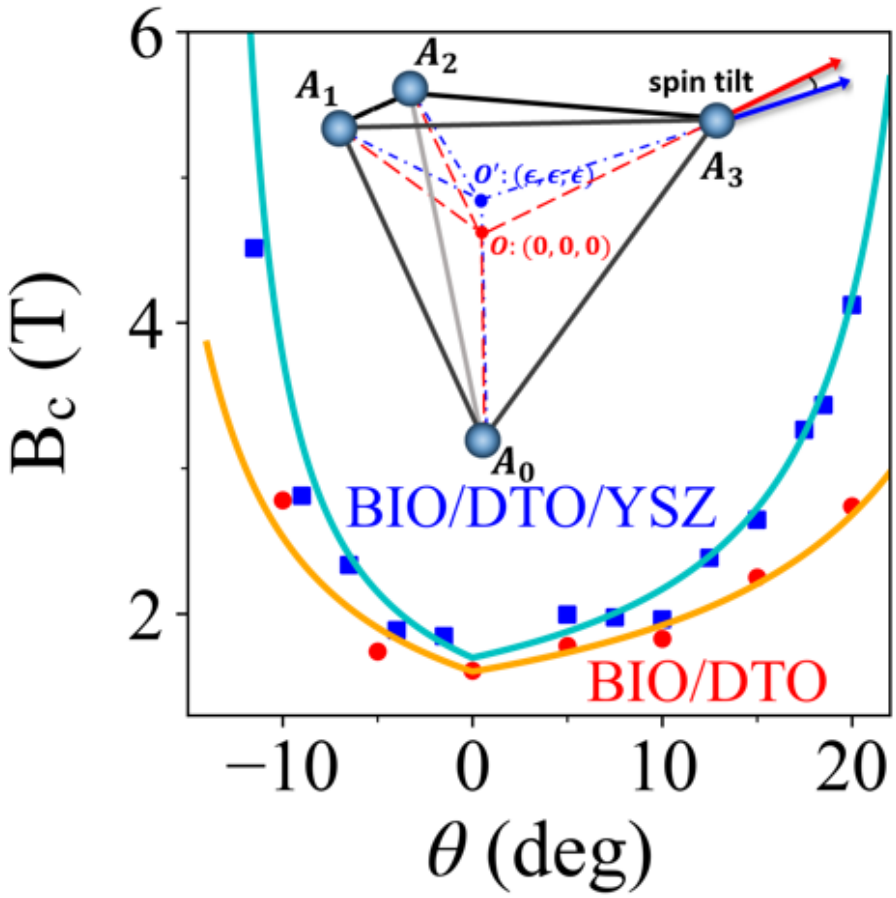


**Figure 5.5:** Experimental and simulated field-angle dependence of the critical field $B_c$. The deep blue dots represent the measured result of BIO/DTO/YSZ which is extracted from the MR anomaly in Fig. 5.4(b) (bottom) by fitting exponentially modified Gaussian distribution, and the light blue line corresponds to Eq. 5.2 with $J_{eff}$ = 0.66 K, $\epsilon$ = 0.1, and $B_{dem}$ = 0.88 T. The red dots represent $B_c$ extracted from the MR anomaly [105] of BIO/DTO by fitting exponentially modified Gaussian distribution, and the orange line corresponds to Eq. 5.1 with $J_{eff}$ = 1.01 K and $B_{dem}$ = 0.7 T. The error bar of fitting for two heterostructures is less than 0.03 T. Field-angle dependence of the critical field $B_c$ shows the consistency by using other extraction methods in Fig. 5.6. The difference of $B_{dem}$ between DTO film and crystal is due to the much thinner vertical dimension of the film than the crystal substrate. Inset: Schematic that shows the off-center of the Ising spins. The coordinate of the tetrahedron corners are: $A_0(-1,-1,-1), A_1(1,-1,1), A_2(-1,1,1), A_3(1,1,-1)$.

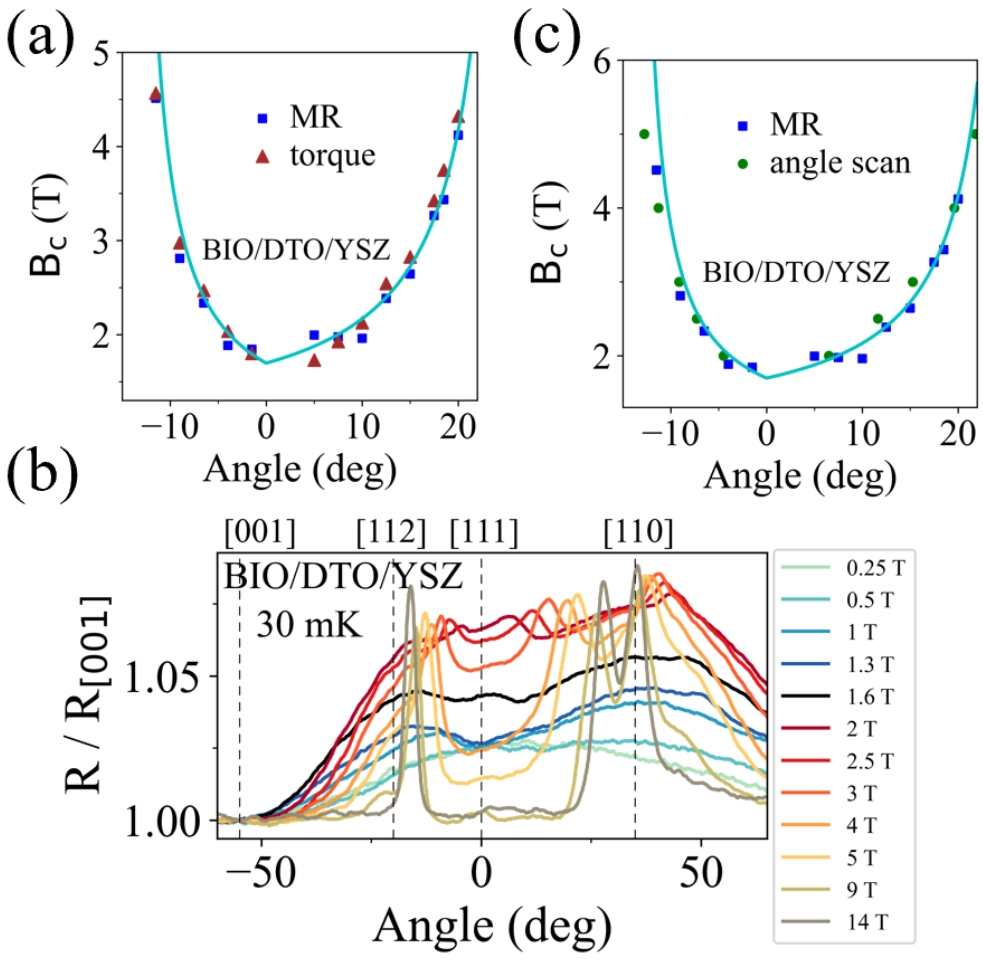


**Figure 5.6:** (a): Experimental field-angle dependence of the critical field $B_c$ in BIO/DTO/YSZ heterostructure. The brown dots represent the measured result which is extracted from the peaks in the derivative of effective magnetic moment in Fig. 5.4(b) (middle). The blue dots represent the measured result which is extracted from the MR anomaly in Fig. 5.4(b) (bottom) by fitting exponentially modified Gaussian distribution. The result of these two methods is close to each other. (b): Normalized resistivity as a function of angle in (1-10) plane from [001] to [110] axis at 30 mK for BIO/DTO/YSZ heterostructure, the applied magnetic field varies from 0.25 T to 14 T. (c): Experimental field-angle dependence of the critical field $B_c$ in BIO/DTO/YSZ heterostructure. The green dots represent the measured result which is extracted from the peaks in Fig. 5.6(b). The blue dots represent the measured result which is extracted from the MR anomaly in Fig. 5.4(b) (bottom) by fitting exponentially modified Gaussian distribution. The result of these two methods is close to each other.

Interestingly, this modified relation (light blue curve) now reproduces $B_c$ of the DTO film (deep blue dots) very well, and the fitting yields $J_{eff} = 0.66$ K and $\epsilon = 0.1$, which corresponds to $\sim 3.2°$ tilt of the Ising spin axis. Note that, simply adjusting $\epsilon$ without changing $J_{eff}$ will not reproduce the observed angular dependence since $J_{eff}$ and $\epsilon$ stand for fundamentally different effects.

The significant reduction of $J_{eff}$ in the film from the bulk crystal suggests that the ice states are more vulnerable to thermal fluctuations, implying a reduced freezing temperature and a lower critical end point of the ice-rule-breaking transition [128]. To verify the changes to these two temperature scales, we measured the thermal evolution at $\theta = 18°$, which is in between [111] and [110]. As shown in Fig. 5.7(a), the height of the BIO MR anomaly, quantified as the peak amplitude based on an exponentially modified Gaussian fitting to the anomaly, starts to decrease around 0.21 K. This decrease can be seen more clearly in Fig. 5.7(c). The anomaly becomes practically invisible around 0.65 K. For comparison, The peak amplitude of BIO/DTO heterostructure starts to decrease around 0.5 K and becomes practically invisible around 1.0 K [105], which are close to the critical end point temperature $T_c$ around 0.5 K and the freezing temperature $T_s$ around 1.2 K reported for DTO crystals [11, 130, 128, 142] and indicate the thermal evolution of the MR anomaly can capture these two temperature scales. The overall significant downshift of the thermal evolution shows that $T_c$ and $T_s$ are both reduced in the DTO film, which is consistent with a reduced $J_{eff}$. The downshift is captured by the concurrently measured CTM as well [Fig. 5.7(b)] by tracking the temperature where the step-like jump of $M_{eff}$ starts to smear. This behavior signifies a smooth rotation of the magnetization vector between [110] and [111], which occurs when the transition becomes a crossover above $T_c$. Above $T_s$, the rotation is fully continuous, and the CTM curve becomes an almost linear line. Therefore, both CTM and proximitized transport show the same reduced thermal stability of the ice states.

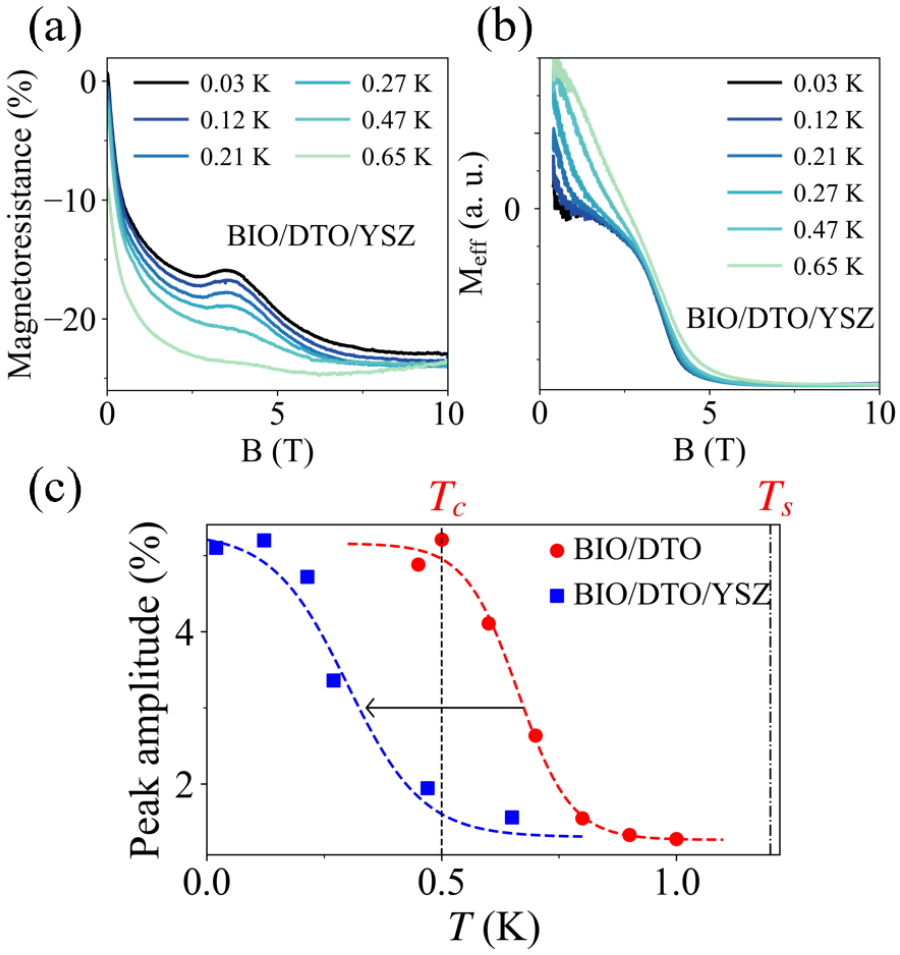


**Figure 5.7:** (a): The MR anomaly for BIO/DTO/YSZ while **B** deviates from [111] to [110] by $\sim 18°$. (b): The effective magnetic moment for BIO/DTO/YSZ while **B** deviates from [111] to [110] by $\sim 18°$. (c): The amplitude of the BIO MR anomaly at different temperatures extracted from exponentially modified Gaussian fittings. The blue dot is for BIO/DTO/YSZ heterostructure extracted from Fig. 5.7(a), and the red dot is for BIO/DTO heterostructure extracted from Ref. [105]. The shift from red dashed line to blue dashed line indicates the overall significant downshift of the thermal evolution from DTO crystal to DTO film.

## 5.3 Discussion

To estimate $T_s$ from $J_{eff}$, one may follow the phase diagram of the Ising pyrochlore from the Monte Carlo calculation on the DSIM. Specifically, the phase diagram presents a relationship between $T_s/D_{nn}$ and $J_{nn}/D_{nn}$, and predicts that the (2:2) state persists in the presence of an antiferromagnetic exchange interaction up to $J_{nn}/D_{nn} \sim -0.91$ [128]. To estimate $J_{nn}/D_{nn}$ from $J_{eff}$, we utilized the fact that $D_{nn}$ is inverse proportional to the volume, and obtained $D_{nn} = 2.24$ K based on the lattice parameters and the reported values of $D_{nn}$ of other Dy-based pyrochlores. That leads to $J_{nn} = -1.58$ K and hence $J_{nn}/D_{nn} = -0.7$, which corresponds to $T_s$ =0.81 K according to the DSIM phase diagram (Fig. 5.8). This value is indeed reduced from the bulk crystal.

Nevertheless, this analysis allow us to put the DTO film on the DSIM phase diagram for comparison with not only DTO crystal but also other Dy-based spin ice pyrochlores. Our previous studies [142] showed that, when increasing chemical pressure (decreasing lattice parameter) from $Dy_2Sn_2O_7$ to $Dy_2Ti_2O_7$ and to $Dy_2Ge_2O_7$, the system is pushed toward the critical value of $J_{nn}/D_{nn}$, as shown in Fig. 5.8. For the smallest $Dy_2Ge_2O_7$, $J_{nn}/D_{nn} = -0.73$, which is comparable to that of the DTO thin film. One important prediction of the DSIM is that the spin ice state survives until $J_{nn}/D_{nn}$ = -0.91. Passing this critical point, the system would enter the antiferromagnetic ordering regime. While reaching this critical point is a long-sought goal of the spin ice studies, no bulk Dy or Ho-pyrochlores has achieved it yet. $Dy_2Ge_2O_7$ is the smallest Dy-pyrochlore studied so far and it has to been prepared under high pressure to stabilize its cubic structure. Our study here shows that thin film engineering provides another route to this goal and the combined magnetic torque-proximitized transport measurement offers an effective probe. In the future, heterostructures with different substrates by replacing YSZ to introduce different types and different strength of strain effects are highly desirable to achieve this goal.

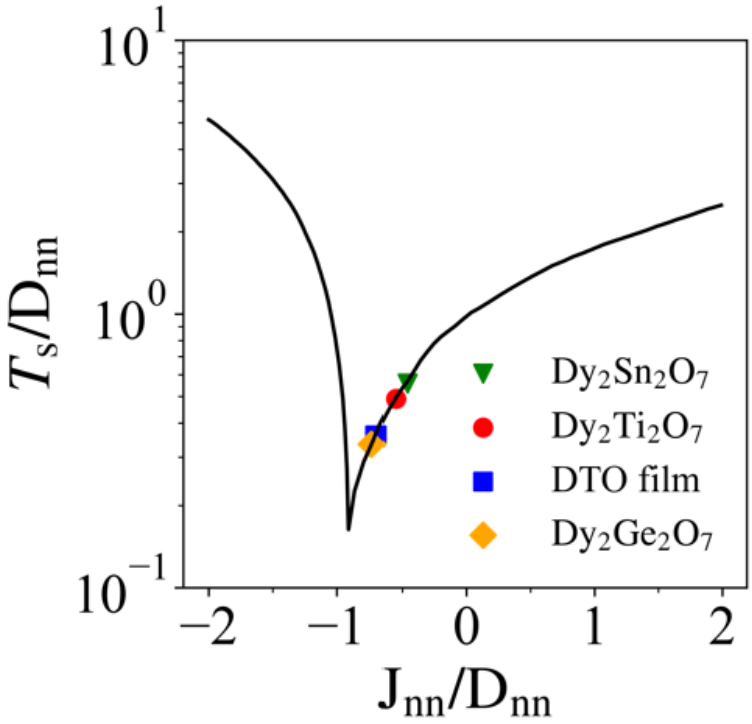


**Figure 5.8:** Dependencies of the short-range ordering temperature $T_s/D_{nn}$ on $J_{nn}/D_{nn}$ ratio for Dy pyrochlore system. The solid lines are the DSIM model calculation from Ref. [128] and the data pionts for bulk Dy-pyrochlores are from Ref. [142].

In summary, the MR and CTM results proves that the DTO thin film on YSZ still has the spin ice ground state but with modified magnetic interactions likely due to a combination of volume compression and geometric distortion under the epitaxial strain. Thin film engineering is thus a promising method to drive the system toward the critical point of the DSIM phase diagram and explore potentially new magnetic properties. In general, our results show that both the CTM and the MR are able to probe thin layers of insulating frustrated magnets but from different perspectives. While the former detects the magnetization vector, the latter is sensitive to the fluctuations. Their consistency in tracking the transition demonstrates that proximitized transport is an efficient probe, which could potentially be applicable even if the magnetic signal of the bulk of the film is beyond the CTM detection because the response of the itinerant electrons only relies on the interfacial coupling with the local moments but not the sample volume.

# Chapter 6

# Summary

This dissertation focused on harnessing the pyrochlore heterostructures, which combine the insulating GFQMs and spin-orbit entangled correlated metal, to study the exotic magnetic excitations in GFQMs. We have discussed three different heterostructures based on different choices of GFQMs.

In chapter 3, we show that, by designing a $Bi_2Ir_2O_7/Dy_2Ti_2O_7$ heterostructure, the breaking of the spin-ice rule in insulating $Dy_2Ti_2O_7$ leads to a charge response in the conducting $Bi_2Ir_2O_7$ measured as anomalous magnetoresistance during the field-induced Kagome ice-to-saturated ice transition. The magnetoresistive anomaly also captures the characteristic angular and temperature dependence of this ice-rule-breaking transition, which has been understood as magnetic monopole condensation. These results demonstrate a novel heteroepitaxial approach for electronically probing the transition between exotic insulating spin states, laying out a blueprint for the metallization of frustrated quantum magnets.

In chapter 4, we show that the quantum fluctuations of a localized frustrated magnet induce strong proximitized charge transport of the conduction electrons in a synthetic heterostructure comprising an epitaxial $Bi_2Ir_2O_7$ ultrathin film on the single crystal of $Yb_2Ti_2O_7$. The proximity effects are evidenced by the scaling behavior of the $Bi_2Ir_2O_7$ resistance in correspondence with the dynamic scaling of the dynamic

spin correlation function of $Yb_2Ti_2O_7$, which is a result of quantum fluctuations near a multi-phase quantum critical point. The proximitized transport in $Bi_2Ir_2O_7$ can be effectively tuned by magnetic field through suppressing the quantum spin fluctuations as well as inducing transitions via magnetic anisotropy in $Yb_2Ti_2O_7$. It establishes a new pathway for harnessing quantum spin fluctuations in magnetic insulators with electric transport, offering exciting prospects for potential applications in the realm of quantum spintronics.

In chapter 5, we synthesized 18nm-thick $Dy_2Ti_2O_7$ thin film on YSZ substrate and capped by a thin conductive $Bi_2Ir_2O_7$ layer, and performed capacitive torque magnetometry and proximitized magnetoresistance measurements simultaneously. The results confirmed that the ice-rule-breaking phase transition survives in the thin film but with a significantly reduced effective nearest-neighbor interaction compared to the bulk crystal. This study demonstrates that both torque magnetometry and proximitized transport are able to probe the exotic magnetism but from different perspective and may combine as an effective tool for thin films of insulating frustrated magnets.

# Bibliography


[1] Hung T Diep et al. *Frustrated spin systems*. World scientific, 2013. 1

[2] Claudine Lacroix, Philippe Mendels, and Frédéric Mila. *Introduction to frustrated magnetism: materials, experiments, theory*, volume 164. Springer Science & Business Media, 2011. 1, 24, 25, 37, 41, 42

[3] Jason S Gardner, Michel JP Gingras, and John E Greedan. Magnetic pyrochlore oxides. *Reviews of Modern Physics*, 82(1):53, 2010. 1, 2, 4, 6, 24, 25, 67

[4] Bruno Tomasello, Claudio Castelnovo, Roderich Moessner, and Jorge Quintanilla. Single-ion anisotropy and magnetic field response in the spin-ice materials $Ho_2Ti_2O_7$ and $Dy_2Ti_2O_7$. *Physical Review B*, 92(15):155120, 2015. 2, 3, 67

[5] H Fukazawa, RG Melko, R Higashinaka, Y Maeno, and MJP Gingras. Magnetic anisotropy of the spin-ice compound $Dy_2Ti_2O_7$. *Physical Review B*, 65(5):054410, 2002. 2, 5, 61, 68

[6] R Siddharthan, BS Shastry, AP Ramirez, A Hayashi, RJ Cava, and S Rosenkranz. Ising pyrochlore magnets: Low-temperature properties,"ice rules," and beyond. *Physical Review Letters*, 83(9):1854, 1999. 3, 4, 24, 25, 44, 67

[7] A Bertin, Y Chapuis, P Dalmas De Réotier, and A Yaouanc. Crystal electric field in the $R_2Ti_2O_7$ pyrochlore compounds. *Journal of Physics: Condensed Matter*, 24(25):256003, 2012. 3, 4, 8

[8] Linus Pauling. The structure and entropy of ice and of other crystals with some randomness of atomic arrangement. *Journal of the American Chemical Society*, 57(12):2680–2684, 1935. 4, 67

[9] Arthur P Ramirez, A Hayashi, Robert Joseph Cava, R Siddharthan, and BS Shastry. Zero-point entropy in 'spin ice'. *Nature*, 399(6734):333–335, 1999. 5, 25, 41, 44, 67

[10] Kazuyuki Matsuhira, Zenji Hiroi, Takashi Tayama, Seishi Takagi, and Toshiro Sakakibara. A new macroscopically degenerate ground state in the spin ice compound dy2ti2o7 under a magnetic field. *Journal of Physics: Condensed Matter*, 14(29):L559, 2002. 5, 6

[11] Ryuji Higashinaka, Hideto Fukazawa, Kazuhiko Deguchi, and Yoshiteru Maeno. Low temperature specific heat of $Dy_2Ti_2O_7$ in the kagome ice state. *Journal of the Physical Society of Japan*, 73(10):2845–2850, 2004. 6, 7, 68, 79

[12] Claudio Castelnovo, Roderich Moessner, and Shivaji L Sondhi. Magnetic monopoles in spin ice. *Nature*, 451(7174):42–45, 2008. 6, 7, 8, 25, 41, 42, 44, 67

[13] Leon Balents. Spin liquids in frustrated magnets. *Nature*, 464(7286):199–208, 2010. 8, 24, 42, 43, 44

[14] Kate A Ross, Lucile Savary, Bruce D Gaulin, and Leon Balents. Quantum excitations in quantum spin ice. *Physical Review X*, 1(2):021002, 2011. 8, 44, 61, 66

[15] LiDong Pan, NJ Laurita, Kate A Ross, Bruce D Gaulin, and NP Armitage. A measure of monopole inertia in the quantum spin ice $Yb_2Ti_2O_7$. *Nature Physics*, 12(4):361–366, 2016. 8, 44

[16] Elsa Lhotel, SR Giblin, Martin R Lees, Geetha Balakrishnan, LJ Chang, and Yukio Yasui. First-order magnetic transition in $Yb_2Ti_2O_7$. *Physical Review B*, 89(22):224419, 2014. 8, 44

[17] Lieh-Jeng Chang, Shigeki Onoda, Yixi Su, Ying-Jer Kao, Ku-Ding Tsuei, Yukio Yasui, Kazuhisa Kakurai, and Martin Richard Lees. Higgs transition from a magnetic coulomb liquid to a ferromagnet in $Yb_2Ti_2O_7$. *Nature communications*, 3(1):992, 2012. 8, 44

[18] RM D'Ortenzio, HA Dabkowska, SR Dunsiger, BD Gaulin, MJP Gingras, T Goko, JB Kycia, L Liu, T Medina, TJ Munsie, et al. Unconventional magnetic ground state in $Yb_2Ti_2O_7$. *Physical Review B*, 88(13):134428, 2013. 9, 44

[19] HWJ Blöte, RF Wielinga, and WJ Huiskamp. Heat-capacity measurements on rare-earth double oxides r2m2o7. *Physica*, 43(4):549–568, 1969. 9

[20] Lieh-Jeng Chang, Martin R Lees, Isao Watanabe, Adrian D Hillier, Yukio Yasui, and Shigeki Onoda. Static magnetic moments revealed by muon spin relaxation and thermodynamic measurements in the quantum spin ice yb 2 ti 2 o 7. *Physical Review B*, 89(18):184416, 2014. 9

[21] A Yaouanc, P Dalmas De Réotier, C Marin, and V Glazkov. Single-crystal versus polycrystalline samples of magnetically frustrated $Yb_2Ti_2O_7$: specific heat results. *Physical Review B*, 84(17):172408, 2011. 9, 44

[22] KE Arpino, BA Trump, AO Scheie, TM McQueen, and SM Koohpayeh. Impact of stoichiometry of $Yb_2Ti_2O_7$ on its physical properties. *Physical Review B*, 95(9):094407, 2017. 9, 10, 17, 44, 46, 64

[23] Steffen Säubert, Allen Scheie, Christopher Duvinage, Jonas Kindervater, Shu Zhang, HJ Changlani, Guangyong Xu, SM Koohpayeh, Oleg Tchernyshyov, Collin L Broholm, et al. Orientation dependence of the magnetic phase diagram of $Yb_2Ti_2O_7$. *Physical Review B*, 101(17):174434, 2020. 9, 10, 11

[24] Allen Scheie, Jonas Kindervater, Shu Zhang, Hitesh J Changlani, Gabriele Sala, Georg Ehlers, Andre Heinemann, Gregory S Tucker, Seyed M Koohpayeh, and Collin Broholm. Multiphase magnetism in $Yb_2Ti_2O_7$. *Proceedings of the National Academy of Sciences*, 117(44):27245–27254, 2020. 10, 11, 44, 57, 64

[25] Allen Scheie, Owen Benton, Mathieu Taillefumier, Ludovic DC Jaubert, Gabriele Sala, Niina Jalarvo, Seyed M Koohpayeh, and Nic Shannon. Dynamical scaling as a signature of multiple phase competition in $Yb_2Ti_2O_7$. *Physical Review Letters*, 129(21):217202, 2022. 10, 11, 44, 54, 64

[26] A Scheie, J Kindervater, S Säubert, C Duvinage, C Pfleiderer, HJ Changlani, S Zhang, Leland Harriger, K Arpino, SM Koohpayeh, et al. Reentrant phase diagram of $Yb_2Ti_2O_7$ in a <111>magnetic field. *Physical Review Letters*, 119(12):127201, 2017. 9, 44, 61, 62

[27] William Witczak-Krempa, Gang Chen, Yong Baek Kim, and Leon Balents. Correlated quantum phenomena in the strong spin-orbit regime. *Annu. Rev. Condens. Matter Phys.*, 5(1):57–82, 2014. 13

[28] Jiun-Haw Chu, Jian Liu, Han Zhang, Kyle Noordhoek, Scott C Riggs, Maxwell Shapiro, Claudy Ryan Serro, Di Yi, M Mellisa, SJ Suresha, et al. Possible scale invariant linear magnetoresistance in pyrochlore iridates $Bi_2Ir_2O_7$. *New Journal of Physics*, 21(11):113041, 2019. 13, 14, 30, 69

[29] TF Qi, OB Korneta, Xiangang Wan, LE DeLong, P Schlottmann, and G Cao. Strong magnetic instability in correlated metallic $Bi_2Ir_2O_7$. *Journal of Physics: Condensed Matter*, 24(34):345601, 2012. 12, 30, 50, 69

[30] S Nakatsuji, Y Machida, Y Maeno, T Tayama, T Sakakibara, J Van Duijn, L Balicas, JN Millican, RT Macaluso, and Julia Y Chan. Metallic spin-liquid behavior of the geometrically frustrated kondo lattice $Pr_2Ir_2O_7$. *Physical Review Letters*, 96(8):087204, 2006. 12, 25

[31] Kazuyuki Matsuhira, Makoto Wakeshima, Ryo Nakanishi, Takaaki Yamada, Akira Nakamura, Wataru Kawano, Seishi Takagi, and Yukio Hinatsu. Metal–insulator transition in pyrochlore iridates $Ln_2Ir_2O_7$ (Ln= Nd, Sm, and Eu). *Journal of the Physical Society of Japan*, 76(4):043706, 2007. 12

[32] Bohm-Jung Yang and Yong Baek Kim. Topological insulators and metal-insulator transition in the pyrochlore iridates. *Physical Review B*, 82(8):085111, 2010. 12

[33] D Prabhakaran and AT Boothroyd. Crystal growth of spin-ice pyrochlores by the floating-zone method. *Journal of Crystal Growth*, 318(1):1053–1056, 2011. 15, 26

[34] SM Koohpayeh, David Fort, and JS Abell. The optical floating zone technique: A review of experimental procedures with special reference to oxides. *Progress in Crystal Growth and Characterization of Materials*, 54(3-4):121–137, 2008. 17

[35] SM Koohpayeh. Single crystal growth by the traveling solvent technique: A review. *Progress in Crystal Growth and Characterization of Materials*, 62(4):22–34, 2016. 17

[36] QJ Li, LM Xu, C Fan, FB Zhang, YY Lv, B Ni, ZY Zhao, and XF Sun. Single crystal growth of the pyrochlores $R_2Ti_2O_7$ (R= rare earth) by the optical floating-zone method. *Journal of crystal growth*, 377:96–100, 2013. 17

[37] G. K. Hubler D. B. Chrisey. *Pulsed laser deposition of thin films*. Wiley, 1994. 19, 26

[38] Lu Li. *Torque magnetometry in unconventional superconductors*. Princeton University, 2008. 22, 23, 73

[39] C Castelnovo, R Moessner, and Shivaji Lal Sondhi. Spin ice, fractionalization, and topological order. *Annu. Rev. Condens. Matter Phys.*, 3(1):35–55, 2012. 24, 25, 41

[40] Michel JP Gingras and Paul A McClarty. Quantum spin ice: a search for gapless quantum spin liquids in pyrochlore magnets. *Reports on Progress in Physics*, 77(5):056501, 2014. 24, 42

[41] Johannes Knolle and Roderich Moessner. A field guide to spin liquids. *Annual Review of Condensed Matter Physics*, 10(1):451–472, 2019. 24, 42

[42] Nic Shannon, Olga Sikora, Frank Pollmann, Karlo Penc, and Peter Fulde. Quantum ice: a quantum monte carlo study. *Physical review letters*, 108(6):067204, 2012. 24, 42

[43] Lucile Savary and Leon Balents. Quantum spin liquids: a review. *Reports on Progress in Physics*, 80(1):016502, 2016. 24, 42, 44

[44] Yi Zhou, Kazushi Kanoda, and Tai-Kai Ng. Quantum spin liquid states. *Reviews of Modern Physics*, 89(2):025003, 2017. 24, 42, 43, 44

[45] Kimball A Milton. Theoretical and experimental status of magnetic monopoles. *Reports on Progress in Physics*, 69(6):1637, 2006. 24, 42

[46] Giulia Semeghini, Harry Levine, Alexander Keesling, Sepehr Ebadi, Tout T Wang, Dolev Bluvstein, Ruben Verresen, Hannes Pichler, Marcin Kalinowski, Rhine Samajdar, et al. Probing topological spin liquids on a programmable quantum simulator. *Science*, 374(6572):1242–1247, 2021. 24, 42

[47] Taras Yavors' kii, Tom Fennell, Michel JP Gingras, and Steven T Bramwell. Dy 2 ti 2 o 7 spin ice: a test case for emergent clusters in a frustrated magnet. *Physical review letters*, 101(3):037204, 2008. 24, 25

[48] Steven T Bramwell and Michel JP Gingras. Spin ice state in frustrated magnetic pyrochlore materials. *Science*, 294(5546):1495–1501, 2001. 25, 41, 67, 76

[49] Y Tabata, H Kadowaki, Kazuyuki Matsuhira, Z Hiroi, N Aso, E Ressouche, and B Fåk. Kagome ice state in the dipolar spin ice $Dy_2Ti_2O_7$. *Physical Review Letters*, 97(25):257205, 2006. 25, 41, 44

[50] Ludovic DC Jaubert and Peter CW Holdsworth. Signature of magnetic monopole and dirac string dynamics in spin ice. *Nature Physics*, 5(4):258–261, 2009. 25, 41, 67

[51] T Sakakibara, T Tayama, Z Hiroi, Kazuyuki Matsuhira, and Seishi Takagi. Observation of a liquid-gas-type transition in the pyrochlore spin ice compound $Dy_2Ti_2O_7$ in a magnetic field. *Physical Review Letters*, 90(20):207205, 2003. 25, 34, 37, 41, 68

[52] Sarah Mostame, Claudio Castelnovo, Roderich Moessner, and Shivaji L Sondhi. Tunable nonequilibrium dynamics of field quenches in spin ice. *Proceedings of the National Academy of Sciences*, 111(2):640–645, 2014. 25, 30, 37

[53] Xiangang Wan, Ari M Turner, Ashvin Vishwanath, and Sergey Y Savrasov. Topological semimetal and fermi-arc surface states in the electronic structure of pyrochlore iridates. *Physical Review B—Condensed Matter and Materials Physics*, 83(20):205101, 2011. 25

[54] Jasmine N Millican, Robin T Macaluso, Satoru Nakatsuji, Yo Machida, Yoshiteru Maeno, and Julia Y Chan. Crystal growth and structure of r2ir2o7 (r= pr, eu) using molten kf. *Materials research bulletin*, 42(5):928–934, 2007. 25

[55] Kazuyuki Matsuhira, Masashi Tokunaga, Makoto Wakeshima, Yukio Hinatsu, and Seishi Takagi. Giant magnetoresistance effect in the metal–insulator transition of pyrochlore oxide nd2ir2o7. *Journal of the Physical Society of Japan*, 82(2):023706, 2013. 25

[56] Emilie Lefrançois, V Cathelin, Elsa Lhotel, Julien Robert, Pascal Lejay, Claire V Colin, Benjamin Canals, Françoise Damay, Jacques Ollivier, B Fåk, et al. Fragmentation in spin ice from magnetic charge injection. *Nature communications*, 8(1):209, 2017. 25

[57] Matthew J Pearce, K Götze, A Szabó, TS Sikkenk, Martin R Lees, AT Boothroyd, D Prabhakaran, Claudio Castelnovo, and PA Goddard. Magnetic monopole density and antiferromagnetic domain control in spin-ice iridates. *Nature Communications*, 13(1):444, 2022. 25

[58] Hiroshi Shinaoka, Shintaro Hoshino, Matthias Troyer, and Philipp Werner. Phase diagram of pyrochlore iridates: all-in–all-out magnetic ordering and non-fermi-liquid properties. *Physical Review Letters*, 115(15):156401, 2015. 30

[59] Hongbin Zhang, Kristjan Haule, and David Vanderbilt. Metal-insulator transition and topological properties of pyrochlore iridates. *Physical review letters*, 118(2):026404, 2017. 30

[60] H Sato, K Matsuhira, T Sakakibara, T Tayama, Z Hiroi, and S Takagi. Field-angle dependence of the ice-rule breaking spin-flip transition in $Dy_2Ti_2O_7$. *Journal of Physics: Condensed Matter*, 19(14):145272, 2007. 35, 76

[61] Naween Anand, Kevin Barry, Jennifer N Neu, David E Graf, Qing Huang, Haidong Zhou, Theo Siegrist, Hitesh J Changlani, and Christianne Beekman. Investigation of the monopole magneto-chemical potential in spin ices using capacitive torque magnetometry. *Nature Communications*, 13(1):3818, 2022. 35, 73, 75

[62] Philip Warren Anderson. Localized magnetic states in metals. *Physical Review*, 124(1):41, 1961. 39

[63] Karsten Held and Ralf Bulla. Mott transition of the f-electron system in the periodic anderson model with nearest neighbor hybridization. *The European Physical Journal B-Condensed Matter and Complex Systems*, 17:7–10, 2000. 39

[64] Tomas Jungwirth, Jörg Wunderlich, and Kamil Olejník. Spin hall effect devices. *Nature materials*, 11(5):382–390, 2012. 39

[65] Laura Bovo, X Moya, D Prabhakaran, Yeong-Ah Soh, AT Boothroyd, ND Mathur, G Aeppli, and ST Bramwell. Restoration of the third law in spin ice thin films. *Nature Communications*, 5(1):3439, 2014. 42, 68

[66] Kevin Barry, Biwen Zhang, Naween Anand, Yan Xin, Arturas Vailionis, Jennifer Neu, Colin Heikes, Charis Cochran, Haidong Zhou, Yiming Qiu, et al. Modification of spin-ice physics in $Ho_2Ti_2O_7$ thin films. *Physical Review Materials*, 3(8):084412, 2019. 42, 68

[67] Sean R Giblin, Steven T Bramwell, Peter CW Holdsworth, Dharmalingam Prabhakaran, and Ian Terry. Creation and measurement of long-lived magnetic monopole currents in spin ice. *Nature Physics*, 7(3):252–258, 2011. 42

[68] SJ Li, ZY Zhao, C Fan, B Tong, FB Zhang, J Shi, JC Wu, XG Liu, HD Zhou, X Zhao, et al. Low-temperature thermal conductivity of dy 2 ti 2 o 7 and yb 2 ti 2 o 7 single crystals. *Physical Review B*, 92(9):094408, 2015. 42

[69] Ritika Dusad. *Magnetic Monopole Noise*. Springer Nature, 2020. 42

[70] Azar B Eyvazov, Ritika Dusad, Timothy JS Munsie, Hanna A Dabkowska, Graeme M Luke, Ethan R Kassner, JC Seamus Davis, and Anna Eyal. Common glass-forming spin-liquid state in the pyrochlore magnets dy 2 ti 2 o 7 and ho 2 ti 2 o 7. *Physical Review B*, 98(21):214430, 2018. 42

[71] Ethan R Kassner, Azar B Eyvazov, Benjamin Pichler, Timothy JS Munsie, Hanna A Dabkowska, Graeme M Luke, and JC Séamus Davis. Supercooled spin liquid state in the frustrated pyrochlore dy2ti2o7. *Proceedings of the National Academy of Sciences*, 112(28):8549–8554, 2015. 42

[72] Franziska KK Kirschner, Felix Flicker, Amir Yacoby, Norman Y Yao, and Stephen J Blundell. Proposal for the detection of magnetic monopoles in spin ice via nanoscale magnetometry. *Physical Review B*, 97(14):140402, 2018. 42

[73] Mateusz Goryca, Xiaoyu Zhang, Jing Li, AL Balk, JD Watts, Chris Leighton, Cristiano Nisoli, Peter Schiffer, and SA Crooker. Field-induced magnetic monopole plasma in artificial spin ice. *Physical Review X*, 11(1):011042, 2021. 42

[74] Ludi Miao, Yonghun Lee, AB Mei, MJ Lawler, and KM Shen. Two-dimensional magnetic monopole gas in an oxide heterostructure. *Nature Communications*, 11(1):1341, 2020. 42, 68

[75] Étienne Lantagne-Hurtubise, Jeffrey G Rau, and Michel JP Gingras. Spin-ice thin films: large-n theory and monte carlo simulations. *Physical Review X*, 8(2):021053, 2018. 42, 68

[76] SA Wolf, DD Awschalom, RA Buhrman, JM Daughton, von S von Molnár, ML Roukes, A Yu Chtchelkanova, and DM Treger. Spintronics: a spin-based electronics vision for the future. *Science*, 294(5546):1488–1495, 2001. 43

[77] Atsufumi Hirohata and Koki Takanashi. Future perspectives for spintronic devices. *Journal of Physics D: Applied Physics*, 47(19):193001, 2014. 43

[78] Vincent Baltz, Aurelien Manchon, M Tsoi, Takahiro Moriyama, T Ono, and Y Tserkovnyak. Antiferromagnetic spintronics. *Reviews of Modern Physics*, 90(1):015005, 2018. 43

[79] Tomas Jungwirth, X Marti, P Wadley, and J Wunderlich. Antiferromagnetic spintronics. *Nature nanotechnology*, 11(3):231–241, 2016. 43

[80] EV Gomonay and VM Loktev. Spintronics of antiferromagnetic systems. *Low Temperature Physics*, 40(1):17–35, 2014. 43

[81] Subir Sachdev. Quantum phase transitions. *Physics world*, 12(4):33, 1999. 43

[82] C Broholm, RJ Cava, SA Kivelson, DG Nocera, MR Norman, and T Senthil. Quantum spin liquids. *Science*, 367(6475):0668, 2020. 43, 44

[83] Matthew B Stone, Igor A Zaliznyak, Tao Hong, Collin L Broholm, and Daniel H Reich. Quasiparticle breakdown in a quantum spin liquid. *Nature*, 440(7081):187–190, 2006. 44

[84] Chetan Nayak, Steven H Simon, Ady Stern, Michael Freedman, and Sankar Das Sarma. Non-abelian anyons and topological quantum computation. *Reviews of Modern Physics*, 80(3):1083, 2008. 44

[85] Mathieu Taillefumier, Owen Benton, Han Yan, Ludovic DC Jaubert, and Nic Shannon. Competing spin liquids and hidden spin-nematic order in spin ice with frustrated transverse exchange. *Physical Review X*, 7(4):041057, 2017. 44

[86] Sean K Takahashi, Jiaming Wang, Alexandre Arsenault, Takashi Imai, Mykola Abramchuk, Fazel Tafti, and Philip M Singer. Spin excitations of a proximate kitaev quantum spin liquid realized in $Cu_2IrO_3$. *Physical Review X*, 9(3):031047, 2019. 44

[87] David Aasen, Roger SK Mong, Benjamin M Hunt, David Mandrus, and Jason Alicea. Electrical probes of the non-abelian spin liquid in kitaev materials. *Physical Review X*, 10(3):031014, 2020. 44

[88] Alexei Kitaev. Anyons in an exactly solved model and beyond. *Annals of Physics*, 321(2):2–111, 2006. 44

[89] A Banerjee, CA Bridges, J-Q Yan, AA Aczel, L Li, MB Stone, GE Granroth, MD Lumsden, Y Yiu, Johannes Knolle, et al. Proximate kitaev quantum spin liquid behaviour in a honeycomb magnet. *Nature materials*, 15(7):733–740, 2016. 44

[90] Yuichi Kasahara, Tsuneya Ohnishi, Yuta Mizukami, Osamu Tanaka, Shuji Ma, Kaori Sugii, Nobuyuki Kurita, Hidekazu Tanaka, Joji Nasu, Yukitoshi Motome, et al. Majorana quantization and half-integer thermal quantum hall effect in a kitaev spin liquid. *Nature*, 559(7712):227–231, 2018. 44

[91] Takuya Yokoi, Shuji Ma, Yuichi Kasahara, Shigeru Kasahara, Takasada Shibauchi, Nobuyuki Kurita, Hidekazu Tanaka, Joji Nasu, Yukitoshi Motome, Claudius Hickey, et al. Quantum criticality and emergent dirac fermions in a frustrated magnet. *Science*, 373(6553):568–573, 2021. 44

[92] Simon Trebst and Cormac Hickey. The kitaev quantum spin liquid: a review. *Physics Reports*, 950:1–82, 2022. 44

[93] Yoshinori Tokura, Masashi Kawasaki, and Naoto Nagaosa. Emergent functions of quantum materials. *Nature Physics*, 13(11):1056–1068, 2017. 44

[94] MR Norman. Colloquium: Herbertsmithite and the search for the quantum spin liquid. *Reviews of Modern Physics*, 88(4):041002, 2016. 44

[95] Jinsheng Wen, Shun-Li Yu, Shiyan Li, Weiqiang Yu, and Jian-Xin Li. Experimental identification of quantum spin liquids. *npj Quantum Materials*, 4(1):12, 2019. 44

[96] Lucy Clark and Aly H Abdeldaim. Quantum spin liquids from a materials perspective. *Annual Review of Materials Research*, 51:495–519, 2021. 44

[97] KA Ross, JPC Ruff, CP Adams, JS Gardner, HA Dabkowska, Y Qiu, JRD Copley, and BD Gaulin. Two-dimensional kagome correlations and field induced

order in the ferromagnetic XY pyrochlore $Yb_2Ti_2O_7$. *Physical Review Letters*, 103(22):227202, 2009. 44

[98] Jordan D Thompson, Paul A McClarty, Henrik M Rønnow, Louis P Regnault, Andreas Sorge, and Michel JP Gingras. Rods of neutron scattering intensity in $Yb_2Ti_2O_7$: compelling evidence for significant anisotropic exchange in a magnetic pyrochlore oxide. *Physical Review Letters*, 106(18):187202, 2011. 44

[99] JD Thompson, Paul A McClarty, D Prabhakaran, I Cabrera, T Guidi, and R Coldea. Quasiparticle breakdown and spin hamiltonian of the frustrated quantum pyrochlore $Yb_2Ti_2O_7$ in a magnetic field. *Physical Review Letters*, 119(5):057203, 2017. 44

[100] Julien Robert, Elsa Lhotel, Gyorgy Remenyi, S Sahling, Isabelle Mirebeau, Claudia Decorse, Benjamin Canals, and Sylvain Petit. Spin dynamics in the presence of competing ferromagnetic and antiferromagnetic correlations in $Yb_2Ti_2O_7$. *Physical Review B*, 92(6):064425, 2015. 44

[101] J Gaudet, KA Ross, E Kermarrec, NP Butch, G Ehlers, HA Dabkowska, and BD Gaulin. Gapless quantum excitations from an icelike splayed ferromagnetic ground state in stoichiometric $Yb_2Ti_2O_7$. *Physical Review B*, 93(6):064406, 2016. 44

[102] Viviane Peçanha-Antonio, Erxi Feng, Yixi Su, Vladimir Pomjakushin, Franz Demmel, Lieh-Jeng Chang, Robert J Aldus, Yinguo Xiao, Martin R Lees, and Thomas Brückel. Magnetic excitations in the ground state of $Yb_2Ti_2O_7$. *Physical Review B*, 96(21):214415, 2017. 44

[103] Sylvain Petit. On the way to understanding $Yb_2Ti_2O_7$. *Proceedings of the National Academy of Sciences*, 117(47):29263–29264, 2020. 44

[104] Steffen Säubert, Allen Scheie, Christopher Duvinage, Jonas Kindervater, Shu Zhang, HJ Changlani, Guangyong Xu, SM Koohpayeh, Oleg Tchernyshyov,

Collin L Broholm, et al. Orientation dependence of the magnetic phase diagram of $Yb_2Ti_2O_7$. *Physical Review B*, 101(17):174434, 2020. 44, 57, 59, 61

[105] Han Zhang, Chengkun Xing, Kyle Noordhoek, Zhaoyu Liu, Tianhao Zhao, Lukas Horák, Qing Huang, Lin Hao, Junyi Yang, Shashi Pandey, et al. Anomalous magnetoresistance by breaking ice rule in $Bi_2Ir_2O_7/Dy_2Ti_2O_7$ heterostructure. *Nature Communications*, 14(1):1404, 2023. 44, 53, 57, 61, 69, 73, 76, 77, 79, 80

[106] ST Bramwell, MJ Harris, BC Den Hertog, MJP Gingras, JS Gardner, DF McMorrow, AR Wildes, AL Cornelius, JDM Champion, RG Melko, et al. Spin correlations in $Ho_2Ti_2O_7$: a dipolar spin ice system. *Physical Review Letters*, 87(4):047205, 2001. 44, 67, 68

[107] Ludovic DC Jaubert, Mark J Harris, Tom Fennell, Roger G Melko, Steven T Bramwell, and Peter CW Holdsworth. Topological-sector fluctuations and curie-law crossover in spin ice. *Physical Review X*, 3(1):011014, 2013. 44

[108] Jiun-Haw Chu, Jian Liu, Han Zhang, Kyle Noordhoek, Scott C Riggs, Maxwell Shapiro, Claudy Ryan Serro, Di Yi, M Mellisa, SJ Suresha, et al. Possible scale invariant linear magnetoresistance in pyrochlore iridates $Bi_2Ir_2O_7$. *New Journal of Physics*, 21(11):113041, 2019. 46, 50, 59

[109] I Balberg. Critical resistance and magnetoresistance in magnetic materials. *Physica B+ C*, 91:71–81, 1977. 50

[110] Zhentao Wang, Kipton Barros, Gia-Wei Chern, Dmitrii L Maslov, and Cristian D Batista. Resistivity minimum in highly frustrated itinerant magnets. *Physical Review Letters*, 117(20):206601, 2016. 54

[111] Han Yan, Owen Benton, Ludovic Jaubert, and Nic Shannon. Theory of multiple-phase competition in pyrochlore magnets with anisotropic exchange

with application to $Yb_2Ti_2O_7$, $Er_2Ti_2O_7$, and $Er_2Sn_2O_7$. *Physical Review B*, 95(9):094422, 2017. 54

[112] JN Fuchs, DM Gangardt, Tassilo Keilmann, and GV Shlyapnikov. Spin waves in a one-dimensional spinor bose gas. *Physical Review Letters*, 95(15):150402, 2005. 57

[113] Shu Zhang, Hitesh J Changlani, Kemp W Plumb, Oleg Tchernyshyov, and Roderich Moessner. Dynamical structure factor of the three-dimensional quantum spin liquid candidate $NaCaNi_2F_7$. *Physical Review Letters*, 122(16):167203, 2019. 64

[114] Pontus Laurell, Allen Scheie, Chiron J Mukherjee, Michael M Koza, Mechtild Enderle, Zbigniew Tylczynski, Satoshi Okamoto, Radu Coldea, D Alan Tennant, and Gonzalo Alvarez. Quantifying and controlling entanglement in the quantum magnet $Cs_2CoCl_4$. *Physical Review Letters*, 127(3):037201, 2021. 64

[115] Max Hirschberger, Peter Czajka, SM Koohpayeh, Wudi Wang, and N Phuan Ong. Enhanced thermal hall conductivity below 1 kelvin in the pyrochlore magnet $Yb_2Ti_2O_7$. *arXiv preprint arXiv:1903.00595*, 2019. 64

[116] Shubhayu Chatterjee, Joaquin F Rodriguez-Nieva, and Eugene Demler. Diagnosing phases of magnetic insulators via noise magnetometry with spin qubits. *Physical Review B*, 99(10):104425, 2019. 64

[117] Mark J Harris, ST Bramwell, DF McMorrow, TH Zeiske, and KW Godfrey. Geometrical frustration in the ferromagnetic pyrochlore $Ho_2Ti_2O_7$. *Physical Review Letters*, 79(13):2554, 1997. 67

[118] Sergei V Isakov, R Moessner, and Shivaji Lal Sondhi. Why spin ice obeys the ice rules. *Physical Review Letters*, 95(21):217201, 2005. 67

[119] ST Bramwell and MJ Harris. Frustration in ising-type spin models on the pyrochlore lattice. *Journal of Physics: Condensed Matter*, 10(14):L215, 1998. 67

[120] Steven T Bramwell and Mark J Harris. The history of spin ice. *Journal of Physics: Condensed Matter*, 32(37):374010, 2020. 67

[121] J Snyder, JS Slusky, RJ Cava, and P Schiffer. How 'spin ice'freezes. *Nature*, 413(6851):48–51, 2001. 67

[122] Tom Fennell, PP Deen, AR Wildes, K Schmalzl, D Prabhakaran, AT Boothroyd, RJ Aldus, DF McMorrow, and ST Bramwell. Magnetic coulomb phase in the spin ice $Ho_2Ti_2O_7$. *Science*, 326(5951):415–417, 2009. 67

[123] Ludovic DC Jaubert and Peter CW Holdsworth. Magnetic monopole dynamics in spin ice. *Journal of Physics: Condensed Matter*, 23(16):164222, 2011. 67

[124] David Jonathan Pryce Morris, DA Tennant, SA Grigera, B Klemke, C Castelnovo, R Moessner, C Czternasty, M Meissner, KC Rule, J-U Hoffmann, et al. Dirac strings and magnetic monopoles in the spin ice $Dy_2Ti_2O_7$. *Science*, 326(5951):411–414, 2009. 67

[125] DI Khomskii. Electric dipoles on magnetic monopoles in spin ice. *Nature communications*, 3(1):904, 2012. 67

[126] YM Jana, A Sengupta, and D Ghosh. Estimation of single ion anisotropy in pyrochlore $Dy_2Ti_2O_7$, a geometrically frustrated system, using crystal field theory. *Journal of magnetism and magnetic materials*, 248(1):7–18, 2002. 67

[127] Jacob PC Ruff, Roger G Melko, and Michel JP Gingras. Finite-temperature transitions in dipolar spin ice in a large magnetic field. *Physical Review Letters*, 95(9):097202, 2005. 67

[128] Byron C den Hertog and Michel JP Gingras. Dipolar interactions and origin of spin ice in ising pyrochlore magnets. *Physical Review Letters*, 84(15):3430, 2000. 67, 76, 79, 81, 82

[129] OA Petrenko, MR Lees, and G Balakrishnan. Magnetization process in the spin-ice compound $Ho_2Ti_2O_7$. *Physical Review B*, 68(1):012406, 2003. 68

[130] Zenji Hiroi, Kazuyuki Matsuhira, Seishi Takagi, Takashi Tayama, and Toshio Sakakibara. Specific heat of kagome ice in the pyrochlore oxide $Dy_2Ti_2O_7$. *Journal of the Physical Society of Japan*, 72(2):411–418, 2003. 68, 79

[131] Hidekazu Aoki, Toshiro Sakakibara, Kazuyuki Matsuhira, and Zenji Hiroi. Magnetocaloric effect study on the pyrochlore spin ice compound $Dy_2Ti_2O_7$ in a [111] magnetic field. *Journal of the Physical Society of Japan*, 73(10):2851–2856, 2004. 68

[132] Santiago Andrés Grigera, Rodolfo Alberto Borzi, Demian Gustavo Slobinsky, AS Gibbs, R Higashinaka, Y Maeno, and Tomas Sebastian Grigera. An intermediate state between the kagome-ice and the fully polarized state in $Dy_2Ti_2O_7$. *Papers in physics*, 7(2):0–0, 2015. 68

[133] Gerd Bergmann. Weak localization in thin films: a time-of-flight experiment with conduction electrons. *Physics Reports*, 107(1):1–58, 1984. 68

[134] Shashi Pandey, Han Zhang, Junyi Yang, Andrew F May, Joshua J Sanchez, Zhaoyu Liu, Jiun-Haw Chu, Jong-Woo Kim, Philip J Ryan, Haidong Zhou, et al. Controllable emergent spatial spin modulation in $Sr_2IrO_4$ by in situ shear strain. *Physical Review Letters*, 129(2):027203, 2022. 68

[135] DP Leusink, F Coneri, M Hoek, S Turner, G Van Tendeloo, and H Idrissi. Thin films of the spin ice compound $Ho_2Ti_2O_7$. *APL Materials*, 2(3), 2014. 68

[136] L Bovo, CM Rouleau, D Prabhakaran, and ST Bramwell. Phase transitions in few-monolayer spin ice films. *Nature Communications*, 10(1):1219, 2019. 68

[137] Fangdi Wen, Tsung-Chi Wu, Xiaoran Liu, Michael Terilli, Mikhail Kareev, and Jak Chakhalian. Epitaxial stabilization of (111)-oriented frustrated quantum pyrochlore thin films. *Journal of Applied Physics*, 129(2):025302, 2021. 68

[138] LDC Jaubert, T Lin, TS Opel, PCW Holdsworth, and MJP Gingras. Spin ice thin film: surface ordering, emergent square ice, and strain effects. *Physical Review Letters*, 118(20):207206, 2017. 68

[139] WC Yang, YT Xie, Xing Sun, XH Zhang, Kyungwha Park, SC Xue, YL Li, CG Tao, QX Jia, Yarolsav Losovyj, et al. Stoichiometry control and electronic and transport properties of pyrochlore $Bi_2Ir_2O_7$ thin films. *Physical Review Materials*, 2(11):114206, 2018. 69

[140] Mizuki Ohno, Takahiro C Fujita, and Masashi Kawasaki. Proximity effect of emergent field from spin ice in an oxide heterostructure. *Science Advances*, 10(11):eadk6308, 2024. 73

[141] Rodolfo Alberto Borzi, Flavia Alejandra Gómez Albarracín, Héctor Diego Rosales, Gerardo Luis Rossini, Alexander Steppke, Dharmalingam Prabhakaran, AP Mackenzie, Daniel Carlos Cabra, and Santiago Andrés Grigera. Intermediate magnetization state and competing orders in $Dy_2Ti_2O_7$ and $Ho_2Ti_2O_7$. *Nature Communications*, 7(1):12592, 2016. 76

[142] HD Zhou, JG Cheng, AM Hallas, CR Wiebe, G Li, L Balicas, JS Zhou, JB Goodenough, Jason S Gardner, and ES Choi. Chemical pressure effects on pyrochlore spin ice. *Physical Review Letters*, 108(20):207206, 2012. 79, 81, 82

# Vita

Chengkun Xing is born in Qinghai, P.R China. He received his B.Sc. in Physics from the University of Science and Technology of China in 2017. He then moved to United States to join University of Tennessee, Knoxville. He has worked as a research assistant for six years in the group of Dr. Haidong Zhou and Dr. Jian Liu. And he is expected to receive his Ph.D. in December of 2024.